First Principles Study of Thermally Activated Processes on Transition Metal Surfaces

A
thesis submitted
in partial fulfillment of the requirements for the degree of

DOCTOR OF PHILOSOPHY

by

Kanika Kohli

Roll No.: 20163461



Indian Institute of Science Education and Research, Pune

2022

CERTIFICATE

Certified that the work incorporated in the thesis entitled **First Principles Study of Thermally Activated Processes on Transition Metal Surfaces** submitted by **Kanika Kohli** was carried out by the candidate, under my supervision. The work presented here or any part of it has not been included in any other thesis submitted previously for the award of any degree or diploma from any other University or Institution.

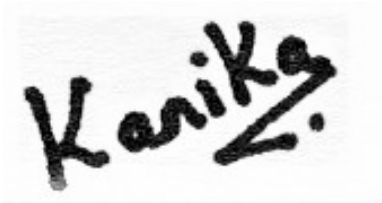


Date: 24-10-2022

(Dr. Prasenjit Ghosh)
Thesis supervisor

Declaration

I declare that this written submission represents my ideas in my own words and where others ideas have been included, I have adequately cited and referenced the original sources. I also declare that I have adhered to all principles of academic honesty and integrity and have not misrepresented or fabricated or falsified any idea/data/fact/source in my submission. I understand that violation of the above will be cause for disciplinary action by the Institute and can also evoke penal action from the sources which have thus not been properly cited or from whom proper permission has not been taken when needed.



Date: 24-10-2022 (Kanika Kohli)

To my mother and father

Acknowledgements

At first, I would like to express my solemn thanks to my thesis supervisor, Dr. Prasenjit Ghosh, for his enormous support, constant motivation, and valuable suggestions throughout my research. His diligent efforts and persistent dedication in tutoring are the reasons behind, my accomplishing different projects accepted during my research period as a research fellow at the Indian Institute of Science Education and Research(IISER), Pune and no doubt is the blessing for my future endeavor. This thesis would not have been possible without his guidance and immense support.

I would like to devote my research work to my family and I am highly thankful to them for giving me a chance to pursue higher studies. My beloved mother and father, late Smt. Savita Kohli and Shri Vipin Kohli, grandmother late Smt. Nirmalkanta Kohli, grandfather late Shri Bansilal Kohli, sister-in-law, Mrs. Manisha Oberoi, elder brother, Mr. Ketan Kohli, my abundant source of love and happiness Ms. Pariza Kohli, small cute puppy Coco, paternal aunt Smt. Vinod Kohli and paternal uncle late Shri Shashi Kohli was my strength. I am highly grateful to my maternal uncle late Shri Sunil Chadha for his belief in me which helped me to reach greater heights today. Their solid support has encouraged me in every tough instance. My parents-in-law, Mrs. Anita Pabbi and Mr. Rajesh Pabbi, grandmother-in-law Smt. Urmil Pabbi, grandfather-in-law late Shri Rabindernath Pabbi, and sister-in-law Hitakshi Pabbi have delightfully accepted me and my research work. I am grateful to my husband, Mr. Lavish Pabbi for his unbounded support and belief in me. All my thanks to their kind nature which did not impede my research work even after my marriage.

I am grateful to the Research Advisory Committee(RAC) members, Dr. Anirban Hazra and Dr. Chiranjib Majumder for their valuable comments and suggestions. The censorious evaluation and comments by RAC members of my research work during RAC meetings were always beneficial which helped me, to gain more insights and also directed me to more constructive paths of my work. I would like to extend my heartfelt thanks to my collaborator, Prof. Ryoji Sahara from the National Institute of Materials Science (NIMS), Tsukuba, Japan who was also the mentor for the first part of my thesis. Further kind invitation for a short-term visit at NIMS through which I was able to meet with renowned scientists and acquire knowledge in different aspects of research.

I would also like to acknowledge the Indian Institute of Science Education and Research (IISER), Pune for funding, for giving outstanding research facilities and a healthy research

environment. I am thankful to the staff of the IT, academic, and administrative section, Srinivas Ramanujan library, hostel management team, and house cleaning staff for their assistance and co-operation. Additionally, I would like to acknowledge the Institute for Materials Research, Tohoku University for computing facility, and National Supercomputing Mission (NSM) for computing resources of PARAM Brahma at IISER Pune.
My special thanks to my friends/co-mates, Ms. Aswathi Mohan, Mr. Mujjafar Hossain, Dr. Abhijit Gupta, Mr. Vineet Kumar Panday, Mr. Unmesh Mondal, and extend my sincere thanks to my seniors Dr. Niharika Joshi, Dr. Subrahmanyam Sappati, Dr. Nandha Kumar, Dr. Rahul Hardikar, Dr. Gautam Sharma, Dr. Aarti Shukla, Dr. Krishnakanth Mondal, Dr. Hridya, Dr. Reman Kumar Singh, Dr. Nishamol Kurkoise and all other lab-mates. Long discussions and their suggestions were always productive towards the improvement of my performance.
Last but not least I would like to express my gratitude to Lord Shiva and thanks to all my near and dear relatives. Thank you everyone for making me complete my doctoral studies.

List of Publications

List of publications resulting from work presented in this thesis

1. Kanika Kohli, Somesh Bhattacharya, Kyosuke Ueda, Takayuki Narushima, Ryoji Sahara, Prasenjit Ghosh, "First principles study of the effect of alloying on oxidation properties of Ti surface: sub-surface diffusion of oxygen",*Langmuir*, **2022**, 38, 4, 1448-1457.

2. Kanika Kohli, Debabrata Chattaraj, Chiranjib Majumder, Prasenjit Ghosh, "Influence of Hydrogen Sulphide on the surface properties and hydrogen permeability through PdCu membrane", under review for *Journal of Physical Chemistry C(JPCC)*

Synopsis

A vast range of solid state properties like ionic conductivity, viscosity, diffusion, chemical reactions etc., fit in the category of the so called thermally activated processes. These processes are also described as, in which system undergoes rare transitions from one potential energy well (minimum energy basin) to another. The dynamic study of activated processes using the computer simulation faces two major challenges (i) to obtain, exact explanation of the occurrence of changes in the electronic structure (ii) need to explore huge portion of the configuration space including the less populated regions like transition state. The time scales associated with these processes are large of the order of milliseconds and are not accessible with regular molecular dynamics simulation. Hence, we need advanced computational methodologies for studying such complex systems, involving dynamics directed by rare transitions.

This thesis mainly concentrates to the study of the activated processes. We, here focus to address some of the features of physico-chemical processes of practical importance in two different alloy systems, in two parts. The first part considers the effect of alloying on the initial oxidation of Ti, where we have investigated the effect of different p and d block elements on the diffusion kinetics of oxygen and its relation with the electronegativity difference. In the second part, we have studied the effect of sulphur impurities on the different processes involved in the solution diffusion mechanism for the permeation of hydrogen through the PdCu membrane, since metallic membrane is one of the most efficient way to purify hydrogen.

The thesis is divided into **five** chapters:

The **first chapter** of the thesis, gives a brief introduction of the thermally activated processes and categorizing the types of the potential energy surface (PES) depending on the degree of smoothness or roughness of the PES. The outline of the different theoretical tools used in the thesis to study physico-chemical processes is also given. In addition, we also give a brief summary of the remaining chapters included in the thesis.

In **Chapter 2**, we present a short note of the basics of theory and techniques on which

our computations are based, to determine the ground state properties and total energy of the system accurately. This involves (a) Born-Oppenheimer approximation and density functional theory, which limits many body problem to solving one body problem, (b) Plane wave basis set to handle periodic, infinitely repeated structures, (c) Pseudopotential method which enables to neglect the electrons in the core shell, for the calculations and also approximates the electron-ion interactions, (d) Supercell approach, which is helpful to study non-periodic systems within the periodic boundary conditions scheme, (e) Density Functional Perturbation Technique (DFPT) to calculate the normal mode frequencies of the initial and the transition state, used to estimate the prefactor for rate kinetics and (f) the shape of the minimum energy path and saddle point are determined using the Nudged Elastic Band (NEB) and Climbing Image Nudged Elastic Band method (CI-NEB).

Degradation of mechanical properties of α-titanium, which is used to manufacture parts of jet engines, due to high temperature oxidation is detrimental for the engine components. Therefore, to overcome this problem there are ongoing endeavours to develop novel oxidation resistant titanium alloys and improve the properties of the existing ones. In **Chapter 3** an effort to understand the effect of alloying on oxidation of α-Ti(0001) surface and to identify descriptors for rational design of oxidation resistant alloys, in this work, using density functional theory based calculations, we have studied oxygen sorption and surface to subsurface diffusion on pure and alloyed α-Ti(0001) surfaces. Zr, Hf, Nb, and Mo from the d-block and Al, Ga, Si, and Ge from the p-block were used as alloying elements. We find that the alloying elements prefers to segregate on the surface compared to the sub-surface layers. Our calculations show that the diffusion barrier correlates with the difference in the electronegativity between the alloying element and Ti. Elements, which are more electropositive than Ti are found to hinder the oxygen dissolution in Ti and vice-versa. We propose that the electronegativity difference can act as a good descriptor for choosing alloying elements. Our results are in reasonably good agreement with experimental reports on growth of oxide layers on these alloyed Ti surface.

Hydrogen is one of the cleanest energy source, since its combustion does not release carbon dioxide. Cost effective production and purification technologies are needed to meet the energy crisis and air pollution. Metallic membranes are the most efficient candidates for hydrogen purification with higher hydrogen permeability and selectivity. Dense palladium based membranes have gained much interest due to their high hydrogen production but, at the same time, they are susceptible to various gases present in the gasification streams or in atmosphere like for example H_2S. Different alloying elements are used in

combination with Pd to improve some of the membrane properties. PdCu membranes is of great interest due to the lower membrane cost, because of the low price of copper and higher hydrogen permeability. In **Chapter 4**, we have investigated the effect of H_2S and S as an impurity on all the processes involved in the hydrogen permeation via solution diffusion mechanism through a modelled PdCu membrane. From our study, we find that the dissociation of H_2S is an activated process on the PdCu(110) surface. Our calculations also suggest that there is decrease in the adsorption energy of hydrogen in the vicinity of S adatoms. The effect of impurity is most prominent at higher coverages on the hydrogen adsorption, dissociation and penetration steps. Evaluating the rates of the different processes in the solution diffusion mechanism, we find that the rate determining steps for permeation of hydrogen through the PdCu membrane are (i) reassociation of atomic H atoms and (ii) H_2 dissociation on the feed side of the membrane.

List of symbols

τ_e	time scale associated with the electron
τ_{ion}	time scale associated with the ion
$\mathbf{R}$	Nuclear coordinates
$\mathbf{r}$	Electronic coordinates
$\Psi(\mathbf{R}, \mathbf{r})$	Eigenfunctions
M	Mass of the nucleus
m	Mass of the electron
$E(\mathbf{R})$	Born-Oppenheimer potential energy surface
Z	Atomic number
e	Charge of an electron
α	marks the electronic state
h	Plank's constant
$\hbar$	defined in terms of Planck's constant = $h/2\pi$
$E[\rho(\mathbf{r})]$	Energy functional
$v(\mathbf{r})$	Energy of the electron-electron interactions
$F[\rho(\mathbf{r})]$	Universal energy functional
$\rho(\mathbf{r})$	Electronic density
p_i	Particle occupancy in a state
H	The Hamiltonian of a system
E_{xc}	Exchange-correlation energy
$\mathbf{k}$	Wavevector
$\mathbf{G}$	Reciprocal lattice vector
F	Force acting on the atom
k_{hTST}	Rate constant of an activated processes
ν_i^{init}	Normal mode frequencies of the system at mimima
ν_j^*	Normal mode frequencies of the system at saddle point
ΔE	Activation energy
k_B	Boltzmann's constant
T	Temperature

$\mathbf{F}_i^{NEB}$	The NEB force acting on image i
$\mathbf{F}_i^{\perp}$	The perpendicular force component
$\mathbf{F}_i^{S\parallel}$	The parallel force component
$\hat{\tau}$	Tangent along the NEB path
k	Spring constant
$P_i(t)$	Probability of finding the system at time t in state i
E_{ads}	Adsorption energy
E_{O+surf}	Total energy of the system with surface and adsorbed species
E_{surf}	Total energy of the clean surface
E_{O_2}	Total energy of O_2 molecule in the gas phase
E^{seg}	Segregation energy
k_{hTST}	rate constant
ΔE^q	Zero-point energy corrected barrier
$E_{surf+nX}$	Total energy of the surface and adsorbed species
E_{surf}	Total energy of the surface
E_X	Total energy of adsorbed molecule X in the gas phase
$E_{ads}^{H;S}$	Adsorption energy of hydrogen respect to S atom on the surface
$E_{surface+S+H}$	Total energy of the surface with S and H coadsorbed
$E_{surface+S}$	Total energy of the surface with S adsorbed
E_H	Total energy of H in vacuum

Contents

List of Publications vi

Synopsis vii

List of symbols x

List of Figures xv

List of Tables xxiv

1 Introduction 1

1.0.1 Thermally activated process 1
1.0.2 Theoretical tools 3
1.0.3 Thesis outline 4

2 Theoretical methods 6

2.0.1 The Born-Oppenheimer and Adiabatic approximation 7
2.0.2 Density functional theory-from wave functions to electron density 10
2.0.2.1 Hohenberg-Kohn theorems 10
2.0.2.2 **Kohn-Sham ansatz** 11
2.0.2.3 Exchange-correlation energy 14
2.0.3 Periodic supercells 16
2.0.3.1 Bloch's theorem 17
2.0.4 Nonperiodic system 18
2.0.5 Electron-ion interactions 18
2.0.6 Computation of vibrational frequencies 21
2.0.6.1 Computation of Phonons from density functional perturbation theory 21
2.0.6.2 Lattice dynamics from electronic-structure theory . . . 22

2.0.7 Nudged Elastic Band (NEB) Method 24
2.0.7.1 Minimum energy path (MEP) and saddle point estimation 24
2.0.7.2 Climbing Image Nudged Elastic Band Method(CI-NEB) 26
2.0.8 *Ab initio* Atomistic Thermodynamics 27

3 Electronegativity difference as a descriptor for oxidation inhibiting effect of alloying element during early stages of titanium oxidation 30
3.1 Introduction 30
3.2 Materials and Methods 32
3.3 Results and Discussion 34
3.3.1 Effect of alloying on properties of Ti(0001) surface 34
3.3.2 Oxygen molecule adsorption on pure and alloyed Ti(0001) surfaces 35
3.3.3 Oxygen sorption on surfaces 37
3.3.3.1 O adsorption at Θ_O = 0.06 ML 37
3.3.3.2 Subsurface O absorption at Θ_O = 0.06 ML 38
3.3.3.3 Oxygen adsorption at higher oxygen coverage (Θ_O>0.06 ML) 40
3.3.3.4 Adsorption versus absorption at Θ_O = 0.50 ML. 43
3.3.3.5 Thermodynamic analysis 44
3.3.4 Coverage dependent diffusion of oxygen from surface to subsurface 46
3.4 Conclusions 50

4 Influence of Hydrogen Sulphide on the surface properties and hydrogen permeability through PdCu membrane 52
4.1 Introduction 52
4.2 Methods 54
4.2.1 Computational Details 54
4.3 Results and Discussion 55
4.3.1 H_2S dissociation 55
4.3.1.1 Adsorption of H_2S and its derivatives on PdCu(110) surface 55
4.3.1.2 H_2S dissociation 58
4.3.2 Coadsorbed H_2 and H_2S dissociation 59
4.3.2.1 H_2 and H_2S coadsorption 59
4.3.2.2 Dissociation of H_2 and H_2S in coadsorbed form 61

4.3.3 Effect of S poisoning 62
4.3.3.1 Coadsorption of atomic S and H at $\Theta_{H,S}$ = 0.16 ML . . 63
4.3.3.2 Effect of S poisoning on H adsorption 64
4.3.3.3 Effect of Sulphur poisoning on the H_2 dissociation at higher H coverage ($1.00 \leq \Theta_H \leq 1.50$ ML) 66
4.3.3.4 Effect of Sulphur poisoning on surface to sub-surface diffusion at $\Theta_H = 1.16$ and 1.50 ML 68
4.3.3.5 Temperature Dependent Kinetics 69
4.4 Conclusions 72

A Appendix A **73**
A.1 Oxygen adsorption on Pure and alloyed Ti(0001) surfaces at higher oxygen coverage θ_O>0.06 ML 73
A.1.1 Pure Ti(0001) surface 73
A.1.2 Alloyed(Ti(0001)) surface 73
A.1.3 Thermodynamic analysis 73
A.1.4 Diffusion barrier of oxygen from the surface into the subsurface layer at lower and higher oxygen coverage 76

B Appendix B **103**
B.1 Adsorption of sulphur-containing species 103
B.2 H_2S dissociation 104
B.3 Coadsorbed H_2 and H_2S dissociation 104
B.3.1 H_2 and H_2S coadsorption 104
B.3.2 Dissociation of H_2 and H_2S in coadsorbed form 104
B.4 Effect of S poisoning 105
B.4.0.1 Coadsorption of atomic S and H at $\Theta_{H,S}$ = 0.16 ML . . 105
B.4.0.2 Effect of S poisoning on H adsorption 105
B.4.0.3 Effect of Sulphur poisoning on the H_2 dissociation at higher H coverage ($1.00 \leq \Theta_H \leq 1.50$ ML) 106
B.4.0.4 Effect of Sulphur poisoning on surface to sub-surface diffusion at $\Theta_H = 1.16$ and 1.50 ML 106

Bibliography **115**

List of Figures

1.1 Systems with rare transitions are categorised depending on how smooth or rough the PES is and on the initial and final state of the system. Depending on the roughness of the PESs, different methods are availaible to study the mechanism of the reaction and reaction rate of the system for which there is prior information about the final state(a-d). Systems presented in a) and b) can be studied using climbing-image nudge elastic band (CI-NEB) while systems presented in c) and d) require double-ended method like path sampling. Single-ended methods can be used to study the systems for which the final state is determined over the course of time. Systems having relatively smooth PESs (examples given in panel e and f) can be studied using kinetic Monte Carlo method and accelerated dynamics methods. Finding the reaction rates of the systems having rough PESs and the final state is predicted over the course of time (examples given in panel g and h), are challenging and are still an active reasearch area. Adapted with permission from Ref [1] 3

2.1 The steps involved in the self-consistent cycle to solve Kohn-Sham equations. Adapted with permission from Ref [2] 15

2.2 Pictorial representation of supercell for surface of solid. Adapted with permission from Ref [3] 19

2.3 Pictorial representation of all-electron and pseudoelectron potentials. Adapted with permission from Ref [3] 20

2.4 Schematic representation of NEB and force projection. $\mathbf{F_i}$ is the force on image i, $\mathbf{F}_i^s|^{\parallel}$ is spring force on image i and $\mathbf{F}_i|^{\perp}$ is perpendicular force on image i. Adapted with permission from Ref [4] 27

2.5 Pictorial representation of MEP by NEB and CI-NEB method. Adapted with permission from Ref [5] 28

3.1 (a)The α-Ti(0001) surface model. The green spheres represent the surface Ti atoms while the blue spheres represent the Ti atoms in the other layers below surface. Variation of segregation energy E_{seg} as a function of the position of the alloying element in different layers for (b) d-block and (c) p-block elements. Variation of (E_{seg}) as a function of $|\Delta EN|$ for the (d) d-block and (e) p-block elements. 33
3.2 Oxygen atom surface adsorption sites; green, blue, black and red denote top Ti, Ti in second layer, alloying element, and oxygen atoms respectively. 38
3.3 Oxygen atom subsurface absorption sites; green, blue, black and red spheres denote surface layer Ti atoms, Ti atoms in the remaining layers of the slab, alloying element, and oxygen atoms respectively. 40
3.4 The calculated binding energies for oxygen atoms adsorbed on the surface at different oxygen coverage. 41
3.5 Multiple-layer adsorption model showing adsorption sites (a) SFCC+Octa(1,2) and (b) SFCC+Octa(2,3). The adsorption energy for different configurations considered. (c) and (d) represents the d and p-block elements. In (a) and (b) green, blue, black and red spheres denote surface layer Ti atoms, Ti atoms in the remaining layers of the slab, alloying element, and oxygen atoms respectively. 44
3.6 Temperature-pressure phase diagrams for O on pure and alloyed Ti(0001) surface showing the transitions from (i) clean to 0.06 ML O coverage ((a) and (d)), (ii) 0.06 ML to 0.5 ML O coverage and (iii) 0.5 ML to 1.0 ML O coverage. The top (bottom) panel shows the effect of alloying Ti with d-block (p-block) elements. 45
3.7 Diffusion barrier as a function of ΔEN at different oxygen coverage. . . 47
3.8 The calculated reaction energy (a), (b) at 0.50 ML and (c), (d) at 1.00 ML oxygen coverage. 48
3.9 (a) Plot and BEP relation between barrier of diffusion of atomic O from surface to sub-surface. (b) Plot of variation of adsorption energy of O adsorbed on the surface with charge on the Ti atom next to the alloying element and interacting with the O atom. (c) Charge on the Ti atom next to the alloying element and interacting with the O atom as a function of ΔEN. 49

4.1 Top view of PdCu(110) surface. Different adsorption sites considered are marked. T, ontop adsorption; B, bridge site; H, hollow site. Pd and Cu atoms are represented in grey, brown color, respectively. 56
4.2 Top and side view of most stable structures of H_2S, SH, and S (0.16 , 0.33 and 0.50 ML). 57
4.3 The energetics and geometries of the initial states(IS), Transition states(TS), and final state(FS) for the H_2S dissociation reaction. The numbers in red are the reaction energies calculated with respect to H_2S on the surface. . . 60
4.4 The top and side view of the most stable coadsorbed configuration. 61
4.5 The energetics and geometries of the initial states(IS), Transition states(TS), and final state(FS) for H_2 and H_2S coadsorbed dissociation reaction. The numbers in red are the reaction energies calculated with respect to H_2 and H_2S on the surface. 63
4.6 The energetics and geometries of the initial states(IS), Transition states(TS), and final state(FS) for H_2 and H_2S coadsorbed dissociation reaction. The numbers in red are the reaction energies calculated with respect to H_2 and H_2S on the surface. 64
4.7 Adsorption energy of H at 0.16 ML of S as a function of distance (d_{S-H}) . 65
4.8 The adsorption energy of H for different H coverage as a function of S coverage. The open circle symbols are for S coverage of 0.00 ML. The open square symbols are for S coverage of 0.16 ML. The open diamond symbols are for S coverage of 0.33 ML. The triangle-up symbols are for S coverage of 0.50 ML. The triangle-down symbol is for S coverage of 1.00 ML 65
4.9 Rate constants for some important processes involved in the solution diffusion mechanism as a function of temperature 70

A.1 The different possible combination of sites on the surface 74
A.2 The three inequivalent configurations for the case of Pure Ti(0001), where the two O atoms are 3.12 (in (a)), 5.10 (in (b)) and 5.85 Å(in (c)). In the figure, the distances are given in Å. 75
A.3 E_{ads} as a function of d_{O-O} in angstrom for the case of Pure Ti(0001). . . 76
A.4 (a)-(j) are the inequivalent configurations of oxygen adsorption on pure Ti(0001), at 0.50 ML O-coverage. 77
A.5 E_{ads} as a function of d_{O-O} in angstrom for the case of d-block elements. . 78

A.6 (a)-(h) are the different inequivalent configurations considered for O adsorption on alloyed Ti(0001) surface at 0.50 ML O coverage. The alloying elements belong to the d-block. 79
A.7 E_{ads} as a function of d_{O-O} in angstrom for the case of p-block elements. . 80
A.8 (a)-(f) are the different inequivalent configurations considered for O adsorption on alloyed Ti(0001) surface at 0.50 ML O coverage. The alloying elements belong to the p-block. 81
A.9 Free energies relative to that of the surface without adsorbate (δF) as a function of temperature at different pressures: (a) 10^{-50}, (b) 10^{-60}, (c) 10^{-90}, and (d) 10^{-100} bar. The dotted-line without any symbol denote the surface without adsorbate. The solid-line with open circles represent surface at oxygen coverage of 0.06 ML. The dotted-line with closed squares, dashed-line with open squares represents surfaces at coverages of 0.50, 1.00 ML, respectively. The dotted-line with closed diamonds, dashed-line with open diamonds represents surfaces at coverage of 0.50 ML Octa(1,2), 1.00 ML Octa(1,2) configuration, respectively. The dotted-line with closed triangles, dashed-line with open triangles represents surfaces at coverage of 0.50 ML Octa(2,3), 1.00 ML Octa(2,3) configuration, respectively. 82
A.10 Free energies relative to that of the surface without adsorbate (ΔF) as a function of temperature at different pressures: (a) 10^{-50}, (b) 10^{-60}, (c) 10^{-90}, and (d) 10^{-100} bar. The dotted-line without any symbol denote the surface without adsorbate. The solid-line with open circles represent surface at oxygen coverage of 0.06 ML. The dotted-line with closed squares, dashed-line with open squares represents surfaces at coverages of 0.50, 1.00 ML, respectively. The dotted-line with closed diamonds, dashed-line with open diamonds represents surfaces at coverage of 0.50 ML Octa(1,2), 1.00 ML Octa(1,2) configuration, respectively. The dotted-line with closed triangles, dashed-line with open triangles represents surfaces at coverage of 0.50 ML Octa(2,3), 1.00 ML Octa(2,3) configuration, respectively. 83

A.11 Free energies relative to that of the surface without adsorbate (ΔF) as a function of temperature at different pressures: (a) 10^{-50}, (b) 10^{-60}, (c) 10^{-90}, and (d) 10^{-100} bar. The dotted-line without any symbol denote the surface without adsorbate. The solid-line with open circles represent surface at oxygen coverage of 0.06 ML. The dotted-line with closed squares, dashed-line with open squares represents surfaces at coverages of 0.50, 1.00 ML, respectively. The dotted-line with closed diamonds, dashed-line with open diamonds represents surfaces at coverage of 0.50 ML Octa(1,2), 1.00 ML Octa(1,2) configuration, respectively. The dotted-line with closed triangles, dashed-line with open triangles represents surfaces at coverage of 0.50 ML Octa(2,3), 1.00 ML Octa(2,3) configuration, respectively. 84

A.12 Free energies relative to that of the surface without adsorbate (ΔF) as a function of temperature at different pressures: (a) 10^{-50}, (b) 10^{-60}, (c) 10^{-90}, and (d) 10^{-100} bar. The dotted-line without any symbol denote the surface without adsorbate. The solid-line with open circles represent surface at oxygen coverage of 0.06 ML. The dotted-line with closed squares, dashed-line with open squares represents surfaces at coverages of 0.50, 1.00 ML, respectively. The dotted-line with closed diamonds, dashed-line with open diamonds represents surfaces at coverage of 0.50 ML Octa(1,2), 1.00 ML Octa(1,2) configuration, respectively. The dotted-line with closed triangles, dashed-line with open triangles represents surfaces at coverage of 0.50 ML Octa(2,3), 1.00 ML Octa(2,3) configuration, respectively. 85

A.13 Free energies relative to that of the surface without adsorbate (ΔF) as a function of temperature at different pressures: (a) 10^{-50}, (b) 10^{-60}, (c) 10^{-90}, and (d) 10^{-100} bar. The dotted-line without any symbol denote the surface without adsorbate. The solid-line with open circles represent surface at oxygen coverage of 0.06 ML. The dotted-line with closed squares, dashed-line with open squares represents surfaces at coverages of 0.50, 1.00 ML, respectively. The dotted-line with closed diamonds, dashed-line with open diamonds represents surfaces at coverage of 0.50 ML Octa(1,2), 1.00 ML Octa(1,2) configuration, respectively. The dotted-line with closed triangles, dashed-line with open triangles represents surfaces at coverage of 0.50 ML Octa(2,3), 1.00 ML Octa(2,3) configuration, respectively. 86

A.14 Free energies relative to that of the surface without adsorbate (ΔF) as a function of temperature at different pressures: (a) 10^{-50}, (b) 10^{-60}, (c) 10^{-90}, and (d) 10^{-100} bar. The dotted-line without any symbol denote the surface without adsorbate. The solid-line with open circles represent surface at oxygen coverage of 0.06 ML. The dotted-line with closed squares, dashed-line with open squares represents surfaces at coverages of 0.50, 1.00 ML, respectively. The dotted-line with closed diamonds, dashed-line with open diamonds represents surfaces at coverage of 0.50 ML Octa(1,2), 1.00 ML Octa(1,2) configuration, respectively. The dotted-line with closed triangles, dashed-line with open triangles represents surfaces at coverage of 0.50 ML Octa(2,3), 1.00 ML Octa(2,3) configuration, respectively. 87

A.15 Free energies relative to that of the surface without adsorbate (ΔF) as a function of temperature at different pressures: (a) 10^{-50}, (b) 10^{-60}, (c) 10^{-90}, and (d) 10^{-100} bar. The dotted-line without any symbol denote the surface without adsorbate. The solid-line with open circles represent surface at oxygen coverage of 0.06 ML. The dotted-line with closed squares, dashed-line with open squares represents surfaces at coverages of 0.50, 1.00 ML, respectively. The dotted-line with closed diamonds, dashed-line with open diamonds represents surfaces at coverage of 0.50 ML Octa(1,2), 1.00 ML Octa(1,2) configuration, respectively. The dotted-line with closed triangles, dashed-line with open triangles represents surfaces at coverage of 0.50 ML Octa(2,3), 1.00 ML Octa(2,3) configuration, respectively. 88

A.16 Free energies relative to that of the surface without adsorbate (ΔF) as a function of temperature at different pressures: (a) 10^{-50}, (b) 10^{-60}, (c) 10^{-90}, and (d) 10^{-100} bar. The dotted-line without any symbol denote the surface without adsorbate. The solid-line with open circles represent surface at oxygen coverage of 0.06 ML. The dotted-line with closed squares, dashed-line with open squares represents surfaces at coverages of 0.50, 1.00 ML, respectively. The dotted-line with closed diamonds, dashed-line with open diamonds represents surfaces at coverage of 0.50 ML Octa(1,2), 1.00 ML Octa(1,2) configuration, respectively. The dotted-line with closed triangles, dashed-line with open triangles represents surfaces at coverage of 0.50 ML Octa(2,3), 1.00 ML Octa(2,3) configuration, respectively. 89

A.17 Free energies relative to that of the surface without adsorbate (ΔF) as a function of temperature at different pressures: (a) 10^{-50}, (b) 10^{-60}, (c) 10^{-90}, and (d) 10^{-100} bar. The dotted-line without any symbol denote the surface without adsorbate. The solid-line with open circles represent surface at oxygen coverage of 0.06 ML. The dotted-line with closed squares, dashed-line with open squares represents surfaces at coverages of 0.50, 1.00 ML, respectively. The dotted-line with closed diamonds, dashed-line with open diamonds represents surfaces at coverage of 0.50 ML Octa(1,2), 1.00 ML Octa(1,2) configuration, respectively. The dotted-line with closed triangles, dashed-line with open triangles represents surfaces at coverage of 0.50 ML Octa(2,3), 1.00 ML Octa(2,3) configuration, respectively. 90
A.18 Charges on the surface Ti atoms at (a) Θ_O = 0.00 ML, (b) Θ_O = 0.06 ML, (c) Θ_O = 0.50 ML Octa(2,3), and (d) Θ_O = 1.00 ML Octa(2,3). 91
A.19 Charges on the surface Ti and Hf atoms at (a) Θ_O = 0.00 ML, (b) Θ_O = 0.06 ML, (c) Θ_O = 0.50 ML , and (d) Θ_O = 1.00 ML Octa(2,3). 92
A.20 Charges on the surface Ti and Zr atoms at (a) Θ_O = 0.00 ML, (b) Θ_O = 0.06 ML, (c) Θ_O = 0.50 ML , and (d) Θ_O = 1.00 ML Octa(2,3). 93
A.21 Charges on the surface Ti and Nb toms at (a) Θ_O = 0.00 ML, (b) Θ_O = 0.06 ML, (c) Θ_O = 0.50 ML , and (d) Θ_O = 1.00 ML Octa(2,3). 94
A.22 Charges on the surface Mo atoms at (a) Θ_O = 0.00 ML, (b) Θ_O = 0.06 ML, (c) Θ_O = 0.50 ML , and (d) Θ_O = 1.00 ML Octa(2,3). 95
A.23 Charges on the surface Ti and Al atoms at (a) Θ_O = 0.00 ML, (b) Θ_O = 0.06 ML, (c) Θ_O = 0.50 ML Octa(2,3) , and (d) Θ_O = 1.00 ML Octa(2,3). 96
A.24 Charges on the surface Ti and Ga atoms at (a) Θ_O = 0.00 ML, (b) Θ_O = 0.06 ML, (c) Θ_O = 0.50 ML Octa(2,3) , and (d) Θ_O = 1.00 ML Octa(2,3). 97
A.25 Charges on the surface Ti and Si atoms at (a) Θ_O = 0.00 ML, (b) Θ_O = 0.06 ML, (c) Θ_O = 0.50 ML Octa(2,3) , and (d) Θ_O = 1.00 ML Octa(2,3). 98
A.26 Charges on the surface Ti and Ge atoms at (a) Θ_O = 0.00 ML, (b) Θ_O = 0.06 ML, (c) Θ_O = 0.50 ML Octa(2,3) , and (d) Θ_O = 1.00 ML Octa(2,3). 99
A.27 The energy profile for surface to sub-surface oxygen diffusion at oxygen coverage of 0.06 ML on pure Ti (a) and alloyed Ti (b), (c), (d), (e), (f), (g), (h), (i) are when the alloying elements are Zr, Hf, Nb, Mo, Al, Ga, Si and Ge respectively. 100

A.28 The energy profile for surface to sub-surface oxygen diffusion at oxygen coverage of 0.5 ML on pure Ti (a) and alloyed Ti (b), (c), (d), (e), (f), (g), (h), (i) are when the alloying elements are Zr, Hf, Nb, Mo, Al, Ga, Si and Ge respectively. 101
A.29 The energy profile for surface to sub-surface oxygen diffusion at oxygen coverage of 1.00 ML on pure Ti (a) and alloyed Ti (b), (c), (d), (e), (f), (g), (h), (i) are when the alloying elements are Zr, Hf, Nb, Mo, Al, Ga, Si and Ge respectively. 102

B.1 The inequivalent configurations of S adsorbed on the surface at Θ_S = 0.33 ML. The numbers below are the shortest distances between two S atoms and are in Å. 103
B.2 Adsorption energy of sulphur(E_{ads}) versus distance between two sulphur atoms(d_{S-S}) in Å. 105
B.3 The inequivalent configurations of S adsorbed on the surface at Θ_S = 0.50 ML arranged in decreasing order of stability. The numbers below are the relative energies in eV. 106
B.4 The energy profile of H_2S dissociation reaction. 106
B.5 The different configurations of coadsorbed H_2 and H_2S. 107
B.6 The energy profile of coadsorbed dissociation reaction for P1. 108
B.7 The energy profile of coadsorbed dissociation reaction for P2. 108
B.8 The configurations with S and H coadsorbed on the surface. The numbers below are the distances between S and H atoms in Å. 109
B.9 Configurations for different combination of Θ_H and Θ_S 110
B.10 The initial and final state configurations for H_2 dissociation pathway for all coverages of H and S atoms. 111
B.11 The energy profile for H_2 dissociation pathway at different H, S coverage. 112
B.12 The initial and final state configurations for H penetration step at different H, S coverage. 113
B.13 The energy profile for the H penetration step at different H, S coverage. . 114

List of Tables

3.1 Electronegativity values (EN) of different alloying elements 35
3.2 Oxygen molecule adsorption in the horizontal and vertical configuration . 36
3.3 Oxygen sorption energy (E_{ads}) on surface and sub-surface sites at 0.06 ML coverage. 39
3.4 Surface to subsurface diffusion barriers of O (in eV) at different oxygen coverage. 47

4.1 Reaction energies (E_r) and barriers (ΔE^c) for H_2S and H_2 dissociation when they are coadsorbed but infinitely away from one another and when both are coadsorbed and are 4.28 Å apart (P1 and P2). For the second SH bond dissociation, the first barrier corresponds to rotation of SH and the second one corresponds to bond cleavage. The data for H_2 dissociation in absence of H_2S have been taken from. [7] 62
4.2 H-H bond length of H_2 (d^{IS}_{H-H}), binding energy of H_2 (E_{BE}), reaction energy of H_2 dissociation (ΔE) and dissociation barriers (E_a)at different H and S coverage (Θ_H and Θ_S). 67
4.3 H penetration barriers and difference between the final and initial state energy (ΔE) at different H and S coverage. 68
4.4 Quantum-Corrected Barriers (ΔE^q), Classical Barriers (ΔE^c), Arhenius Prefactor, and Rate Constants (k_{hTST}) 71

B.1 The adsorption energies and optimized structural parameters of H_2S on PdCu(110) surface. 103
B.2 The adsorption energies and optimized structural parameters of SH on PdCu(110) surface. 104
B.3 The adsorption energies and optimized structural parameters of S on PdCu(110) surface. 104

B.4 The Zero-point energy corrections involved in different processes on PdCu(110) surface. 109

Chapter 1

Introduction

In this thesis I study activated physico-chemical processes using atomistic computer simulations. In particular, I study (a) effect of alloying on oxidation of Ti, and (b) effect of S impurities on hydrogen permeation through PdCu membrane. Both of these are commercially important and are an active area of research. Moreover, In addition to the fact that these processes takes place on metal surfaces, both of them are thermally activated processes.

In section 1.0.1 I give a brief introduction to thermally activated processes. Further in section 1.0.2 brief of theoretical tools used and in section 1.0.3 outline of the chapters in this thesis.

1.0.1 Thermally activated process

The progress achieved in the last 20 years in the field of computer modelling of matter at the nanoscale have opened new ways of investigating chemical reactions with atomic resolution, realising of what can be considered as a virtual laboratory. Ideally, in the virtual laboratory one would like to simulate, step by step, the time evolution of a chemical process as a function of system's temperature and pressure. This can be achieved using first-principles molecular dynamics simulations, which provide insights into phenomenon that takes place with length of time comparable with the characteristic of the microscopic dynamics (some picoseconds). This is the case when relevant kinetics is determined by energy barriers that are low compared to the typical thermal fluctuations. When this is not the case, systems spend most of the time within stable states, so that interesting transitions occur only rarely as in the case of so called **"activated processes"**.
A vast range of solid state properties such as viscosity, ionic conductivity, mass transport, diffusion, and chemical reactions belong to the class of thermally activated processes.

These activated processes are marked by temperature induced quantity proportional to

$$e^{\frac{-E_a}{k_B T}}. \tag{1.1}$$

where E_a is called the energy of activation (indicates the barrier height), T is the absolute temperature and k_b is the Boltzmann's constant. These processes are well defined, in which system undergoes rare transitions from one potential well (minimum in the potential energy surface) to another over potential barriers of height $E_a > k_B T$ [8]. The probability of overcoming an energy barrier becomes exceptionally small by reducing the temperature of the system. Indicating with τ_{fast}, the time scale appropriate for the microscopic dynamics, the transitions between the stable states occurs on a time scale which is approximately given by τ_{slow} nearly equal to $\tau_{fast} * e^{\frac{-E_a}{k_B T}}$. It is clear that as soon as the temperature is reduced below E_a, the transitions becomes a rare event and the process can no longer be studied within the molecular dynamics framework. This sets a fundamental limitation to the kind of processes that can be studied within molecular dynamics because, however fast our computers might be, there will always be interesting phenomenon occuring on timescales unaccessible to it.

For this reason the development of advanced computational methods suited for studying the complex systems whose dynamics is driven by rare events has become the topic of intense research. The study of these phenomenon is based on the identification of the transition states, the configuration that represents the bottleneck for the reaction, which can be identified with the lowest order saddle point that separates the two minima corresponding to the stable states. The highest energy point in the potential energy surface(PES) gives the energy barrier that has to be overcome, and the transition rate can be evaluated using the harmonic transition-state theory(HTST).

In order to understand the reaction mechanism, rate and time length of activated processes in materials, one needs to have an understanding of the PES. Due to the presence of different types of energy landscapes, there are different computational methods availaible to explore them. Generally, the PESs are classified into two types:(i) smoothness or roughness of the PES, and (ii) information about the final state of the system whether it is known initially or needs to be speculated during the course of calculation. Figure 1 shows some of the PESs. [1, 9]

In this thesis, we restrict our focus on the study of thermally activated processes that occur on the surfaces of transition metals. The PES of these systems are rather smooth, in which both initial and final states are known and characterised by a small number of relevant

minima and saddle points. The minimum energy path(MEP) is a good indicator of the reaction mechanism and the transition rate can be estimated using HTST. The climbing image-nudged elastic band(CI-NEB) method represents the best choice for a first principles calculation of the reaction mechanism because the computational cost is only few times larger than that of standard structural optimizations.

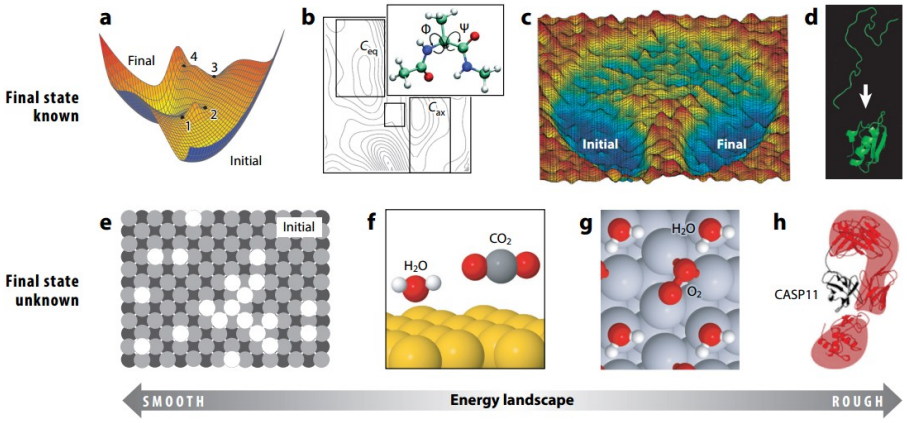


Figure 1.1: Systems with rare transitions are categorised depending on how smooth or rough the PES is and on the initial and final state of the system. Depending on the roughness of the PESs, different methods are availaible to study the mechanism of the reaction and reaction rate of the system for which there is prior information about the final state(a-d). Systems presented in a) and b) can be studied using climbing-image nudge elastic band (CI-NEB) while systems presented in c) and d) require double-ended method like path sampling. Single-ended methods can be used to study the systems for which the final state is determined over the course of time. Systems having relatively smooth PESs (examples given in panel e and f) can be studied using kinetic Monte Carlo method and accelerated dynamics methods. Finding the reaction rates of the systems having rough PESs and the final state is predicted over the course of time (examples given in panel g and h), are challenging and are still an active reasearch area. Adapted with permission from Ref [1]

.

1.0.2 Theoretical tools

There are numerous theoretical tools available with different accuracy level and computational cost to examine the various physico-chemical processes. One needs to make a choice among them based on the process type, and the time length involved with them. All the above mentioned physical processes that have been investigated in this thesis involves bond formation and breaking. This involves calculation of the total energy of the system and a precise information about the electronic structure. Hence, it is necessary to treat the systems quantum mechanically. At the same time, the systems are of large size thereby

making the calculations computationally expensive. Amongst the different computational methods that are available density functional theory (DFT) provides a reasonable balance between accuracy and the computational cost. Hence, in this thesis, we have used DFT to compute the total energies of the systems. The rates for the different activated processes have been computed within the harmonic transition state theory (HTST) as mentioned in equation 1.2. For this, we need to estimate the activation barrier and the prefactor (that depends on the vibrational motion of the IS and TS). To compute the former, we have used the CI-NEB method [5, 10, 11] while for the later we have used density functional perturbation theory (DFPT) [12–14]. All the results presented in this thesis that involves DFT, DFPT and CI-NEB calculations were obtained using the Quantum ESPRESSO software.

$$k_{hTST} = \frac{\prod_{i=1}^{3N} \upsilon_i^{init}}{\prod_{i=1}^{3N-1} \upsilon_i^{*}} e^{\frac{-E^q}{k_BT}} \tag{1.2}$$

1.0.3 Thesis outline

The rest of the thesis is composed of:

Chapter 2: In this chapter we have briefly discussed the computational techniques, like density functional theory, to compute the electronic structure and system's total energy. It also includes a description of the plane-wave implementation of DFT. Additionally, it also includes a short explanation of Density Functional Perturbation Theory (DFPT), to compute the vibrational modes of the minima and the saddle points (transition states) of the PES. It also includes a brief description of CI-NEB method used to estimate the saddle point.

Chapter 3: Due to high demand and tough competition in the aircraft industry, there is a need for the production of aircrafts and its components with lower cost of operation, namely, long serviceable life and highly efficient. Keeping in mind, the development of materials with improved properties is one of the key factors; the primary concerns are light in weight and with long shelf life of components of aircrafts and structures which are resistant to corrosion at high temperatures [15]. Ti alloys with more durability, toughness and stability are extensively used in the aviation sector because of their remarkable features like corrosion resistance and higher ranking mechanical properties. However, at higher temperatures Ti alloys undergo oxidation, effecting the critical components of jet engines. This can also lead to embrittlement on the surfaces and degradation of the mechanical properties of the Ti alloys. Efforts have been made to improve the oxidation

resistance of Ti alloys through some modifications on the surface of the alloys. Hence, in this study, we focus to have an understanding of the initial steps in the oxidation process of α-Ti at high temperature with the diffusion of oxygen in various alloyed Ti(0001) surfaces. The various alloying elements considered in our study are both from d-block(Zr, Hf, Nb, and Mo) and p-block(Al, Ga, Si, and Ge). We, tried to address the correlation between the properties of the different alloys, namely electronegativity, and their effect in inhibiting/aiding the high temperature oxidation process in Ti.

Chapter 4: Hydrogen is considered as one of the cleanest energy sources and environmentally sustainable energy carrier. Large scale use of hydrogen energy is an effective way to solve the greenhouse effect caused by burning of fossil fuels since its combustion does not release CO_2. It is also used as a transportation fuel for reducing motor vehicles emission, aerospace and other fields. The so-called "Hydrogen economy" will provide power generation causing an increased demand of hydrogen in the upcoming years. With the development of world economy, efficient hydrogen production and separation technology is required to provide solutions for global energy crisis and air pollution. Hydrogen rich syngas ($CO+H_2$) is produced on a large scale by "steam-methanol reforming" (SMR) and "water-gas shift reaction". One of the most critical steps in production is purification and separation of pure hydrogen from gasification stream which contains contaminant gases like H_2S, produced as by-products of the reaction or from the atmosphere. Membranes are promising candidates that are currently being employed as a low cost and efficient solution for hydrogen purification. Based on composition, they are classified as metallic (dense and porous), inorganic (oxides, zeolites), carbon and polymeric [16, 17]. Metals like Palladium can transfer dissociated hydrogen atoms via diffusion, being impermeable to other gases and achieving the high hydrogen selectivity. Palladium based membranes have high hydrogen permeability and catalytic activity. However, they are susceptible to surface poisoning induced by gases like H_2S which effects the performance and stability of these membranes. Alloying of Pd with other elements alleviates the above problems and Pd-Cu alloy membrane offers a cost effective solution. In this study, we focus on the effect of H_2S as an impurity on the different steps involved in the hydrogen permeation mechanism through the modelled PdCu(110) membrane.

.

Chapter 2

Theoretical methods

Nature of interaction between electrons and ions have become more prominent nowadays in the field of physics, chemistry and biology. The ability of currently used computational tools for system comprising of sub-atomic particles to evaluate the total energy of a system, ables one to acquire huge benefits from quantum mechanical calculations. Almost all the physical quantities can be computationally obtained from the computed total energies or the difference between them [3]. Some of the examples are lattice constants, bulk moduli, bond lengths, and phonons. With the increasing availaibility of powerful computers, and their decreasing cost, the total energy calculations have shown to be more cost effective than experimental measurements. Apart from raw materials requirements for each different class of physical property, different experimental apparatus is required, though for the case of theoretical approach, most of the physical properties linked with total energies of system can be determined from just one piece of theoretical calculation. This is why quantum mechanical calculations are often used to screen materials that can be used for novel applications. The currently used computational tools with advanced numerical algorithms can handle systems with hundreds, thousands of atoms and proves to be useful in solving real scientific problems in various fields of science.
In this chapter we will describe briefly the theoretical methods and approximations used in this thesis for the first principles calculations.

2.0.1 The Born-Oppenheimer and Adiabatic approximation

The Hamiltonian operator of a system of atoms is the sum of the kinetic and potential energy of the electrons and the nuclei and is given as:

$$\mathbf{H}_{tot} = -\sum_I \frac{\hbar^2}{2M_I}\nabla^2_{\mathbf{R}_I} - \sum_i \frac{\hbar^2}{2m_i}\nabla^2_{\mathbf{r}_i} + \sum_{i,j;i>j} \frac{1}{4\pi\epsilon_0}\frac{e^2}{|\mathbf{r}_i - \mathbf{r}_j|} - \sum_{i,I} \frac{1}{4\pi\epsilon_0}\frac{Z_I e^2}{|\mathbf{R}_I - \mathbf{r}_i|} + \sum_{I,J;I>J} \frac{1}{4\pi\epsilon_0}\frac{Z_I Z_J e^2}{|\mathbf{R}_I - \mathbf{R}_J|}. \tag{2.1}$$

Here $\hbar = h/2\pi$, h is the Planck's constant. M_I and m_i are the masses of the I^{th} nucleus and i^{th} electron, respectively. Z_I is the atomic number of I^{th} nucleus. $\mathbf{R} = \{\mathbf{R}_I\}$ is the set of nuclear coordinates and $\mathbf{r} = \{\mathbf{r}_i\}$ is set of electronic coordinates. So,

$$\mathbf{H}_{tot} = \mathbf{T}_n + \mathbf{T}_e + \mathbf{V}_{ee} + \mathbf{V}_{ne} + \mathbf{V}_{nn}. \tag{2.2}$$

where, $\mathbf{H}_{tot}$ is the total Hamiltonian of a system of electrons and nuclei, $\mathbf{T}_n$ $(= \sum_I \frac{\hbar^2}{2M_I}\nabla^2_{R_I})$ is the kinetic energy of nuclei, $\mathbf{T}_e$ $(= \sum_i \frac{\hbar^2}{2m_i}\nabla^2_{r_i})$ is the kinetic energy of electrons, $\mathbf{V}_{ee}$ $(= \sum_{i,j;i>j} \frac{1}{4\pi\epsilon_0}\frac{e^2}{|\mathbf{r}_i - \mathbf{r}_j|})$ is the potential energy due to electrons-electrons interactions, $\mathbf{V}_{ne}$ $(= \sum_{i,I} \frac{1}{4\pi\epsilon_0}\frac{Z_I e^2}{|\mathbf{R}_I - \mathbf{r}_i|})$ is the potential energy due to electrons-nuclei interactions, and $\mathbf{V}_{nn}$ $(= \sum_{I,J;I>J} \frac{1}{4\pi\epsilon_0}\frac{Z_I Z_J e^2}{|\mathbf{R}_I - \mathbf{R}_J|})$ is the potential energy due to nuclei-nuclei repulsions. Transferring to the centre of mass of a system, the Hamiltonian operator can be written as:

$$\mathbf{H}_{tot} = \mathbf{T}_n + \mathbf{H}_e + \mathbf{H}_{mp}. \tag{2.3}$$

$$\mathbf{H}_e = \mathbf{T}_e + \mathbf{V}_{ne} + \mathbf{V}_{ee} + \mathbf{V}_{nn}. \tag{2.4}$$

$$\mathbf{H}_{mp} = -\frac{1}{2M_{tot}}(\sum_i^{Nelec} \nabla_i)^2, \tag{2.5}$$

where, $\mathbf{H}_e$ is the electronic Hamiltonian depending on the position of nuclei through $\mathbf{V}_{ne}$ and $\mathbf{V}_{nn}$, $\mathbf{H}_{mp}$ is the mass-polarization involving total mass of all nuclei i.e M_{tot}.

Suppose the solution to electronic Schrödinger equation for a given arrangement of ions $\{\mathbf{R}\}$ are known and is given by $\Psi_i(\mathbf{R}, \mathbf{r})$, i.e.

$$\mathbf{H}_e(\mathbf{R})\Psi_i(\mathbf{R}, \mathbf{r}) = E_i(\mathbf{R})\Psi_i(\mathbf{R}, \mathbf{r}); i = 1, 2, ..., \infty \tag{2.6}$$

where, $\mathbf{R}$ represents position of nuclei, $\mathbf{r}$ represents position of electrons. Since the electronic Hamiltonian operator is *Hermitian* operator, $\Psi_i(\mathbf{R}, \mathbf{r})^{'}s$ must be orthonormal, i.e.

$$\int \Psi_i^*(\mathbf{R}, \mathbf{r})\Psi_j(\mathbf{R}, \mathbf{r})d(\mathbf{r}) = \delta_{ij}. \tag{2.7}$$

However, the $\Psi_i(\mathbf{R}, \mathbf{r})$ form a complete basis and hence the exact wave function of a system with no approximations, $\Psi_{tot}(\mathbf{R}, \mathbf{r})$ can be written as sum of electronic functions with coefficients depending only on the nuclear coordinates.

$$\Psi_{tot}(\mathbf{R}, \mathbf{r}) = \sum_{i=1}^{\infty} \Psi_{ni}(\mathbf{R})\Psi_i(\mathbf{R}, \mathbf{r}). \tag{2.8}$$

Putting Eqn 2.8 into the time-independent Schrödinger equation $\mathbf{H}_{tot}\Psi_{tot}(\mathbf{R}, \mathbf{r}) = \mathbf{E}_{tot}\Psi_{tot}(\mathbf{R}, \mathbf{r})$ gives:

$$\sum_{i=1}^{\infty}(\mathbf{T}_n + \mathbf{H}_e + \mathbf{H}_{mp})\Psi_{ni}(\mathbf{R})\Psi_i(\mathbf{R}, \mathbf{r}) = E_{tot}\sum_{i=1}^{\infty}\Psi_{ni}(\mathbf{R})\Psi_i(\mathbf{R}, \mathbf{r}), \tag{2.9}$$

where, $\mathbf{T}_n$ is nuclear kinetic energy expressed as.

$$\mathbf{T}_n = \sum_a -\frac{1}{2M_a}\nabla_a^2 = \nabla_n^2. \tag{2.10}$$

Considering the fact that $\mathbf{H}_e$ and $\mathbf{H}_{mp}$ operate only on the wave function of electrons and Ψ_i is the exact solution to the Schrödinger equation of electrons, Eqn 2.9 can be written as:

$$\sum_{i=1}^{\infty}\{\Psi_i(\nabla_n^2\Psi_{ni}) + 2(\nabla_n\Psi_i)(\nabla_n\Psi_{ni}) + \Psi_{ni}(\nabla_n^2\Psi_i) + \Psi_{ni}E_i\Psi_i + \Psi_{ni}\mathbf{H}_{mp}\Psi_i\} = E_{tot}\sum_{i=1}^{\infty}\Psi_{ni}\Psi_i. \tag{2.11}$$

By multiplying with electron wavefunction Ψ_j^* and integrating over the coordinates of electrons we get:

$$\begin{aligned}\nabla_n{}^2\Psi_{nj} + E_j\Psi_{nj} + \sum_{i=1}^{\infty}\{2 < \Psi_j|\nabla_n|\Psi_i > (\nabla_n\Psi_{ni}) + < \Psi_j|\nabla_n^2|\Psi_i > \Psi_{ni} + \\ < \Psi_j|\mathbf{H}_{mp}|\Psi_i > \Psi_{ni}\} = E_{tot}\Psi_{nj}.\end{aligned} \tag{2.12}$$

The first two terms do not contain wave function of electrons while the terms in bracket

involves coupling between different electronic states. Within the adiabatic approximation total wave function only involves one electronic state. Therefore, all coupling terms between two different electronic states in Eqn 2.12 are neglected, and Eqn 2.12 becomes:

$$(\nabla_n^2 + E_j + < \Psi_j|\nabla_n^2|\Psi_j > + < \Psi_j|\mathbf{H}_{mp}|\Psi_j >)\Psi_{nj} = E_{tot}\Psi_{nj}. \tag{2.13}$$

Re-introducing the kinetic energy operator in Eqn 2.13 and neglecting the mass-polarization term gives

$$(\mathbf{T}_n + E_j + < \Psi_j|\nabla_n^2|\Psi_j >)\Psi_{nj} = E_{tot}\Psi_{nj}. \tag{2.14}$$

The above equation can be rewritten as:

$$(\mathbf{T}_n + E_j(\mathbf{R}) + U(\mathbf{R}))\Psi_{nj}(\mathbf{R}) = E_{tot}\Psi_{nj}(\mathbf{R}), \tag{2.15}$$

where, $U(\mathbf{R})$, the diagonal correction, is smaller than $E_j(\mathbf{R})$, by a factor equal to ratio of electron and nuclear masses. Within the Born-Oppenheimer approximation the term $U(\mathbf{R})$ is neglected and the equation finally takes the form.

$$(\mathbf{T}_n + E_j(\mathbf{R}))\Psi_{nj}(\mathbf{R}) = E_{tot}\Psi_{nj}(\mathbf{R}). \tag{2.16}$$

And, the electronic hamiltonian written as.

$$(\mathbf{T}_e + \mathbf{V}_{ne} + \mathbf{V}_{ee} + \mathbf{V}_{nn})\Psi_i(\mathbf{R}, \mathbf{r}) = E_j(\mathbf{R})\Psi_i(\mathbf{R}, \mathbf{r}). \tag{2.17}$$

The nuclei moves on the potential energy surface in the Born-Oppenheimer picture which is the solution to the Schrödinger equation of electrons. The energy surface here is independent of the mass of the nuclei. Eqn 2.16 can be solved if $E_j(\mathbf{R})$ is known. For most cases one need not solve Eqn 2.16 because the de Broglie wavelength of the heavy nuclei is very small and the nuclei can be treated as classical particles. Therefore for the nuclear dynamics one typically solve Newtonian equation of motion by computing the forces from the derivative of $E_i(\mathbf{R})$. Thus the BO approximation decouples the nuclear and electronic degrees of freedom. We are now left with the task of solving the electronic Hamiltonian Eqn 2.17.

However, this still contains the non-local electron-electron Coulombic potential term. As a consequence this cannot be solved by separation of variables, a commonly used method to solve differential equation. Hence, further approximations are still needed. The next

section describes in detail one of the alternative ways to solve Eqn 2.17.

2.0.2 Density functional theory-from wave functions to electron density

There are many methods that had been developed to solve the Schrödinger equation for the electronic Hamiltonian. These can be classified into two categories:(a) wave function based and (b) density based. Some of the wave function based methods are Hatree, Hartree Fock [18], Coupled cluster [19] etc. In this thesis we have used density based method, namely, density functional theory (DFT) where electron density is the basic variable. Hence, in the remaining section DFT is briefly introduced.

The first quantum mechanical theory for electronic structure of a many body system using density as a basic variable was proposed by Thomas and Ferrin in 1927. Though this acts as a precursor to modern day DFT, it failed to provide quantitative description of realistic systems. Later in 1964 Hohenberg and Kohn, in an effort to set-up a theory for system consisting of interacting particles, proposed two theorems using electron density as the basic variable, which became the fundamental backbone of electronic structure calculations for many body systems in presence of an external potential [20]. These two theorems became the backbone of modern day density functional theory. The Hamiltonian for such system is expressed as:

$$\hat{H} = -\sum_i \frac{\hbar^2}{2m_i}\nabla^2_{\mathbf{r}_i} + \sum_{i,j;i>j} \frac{1}{4\pi\epsilon_0}\frac{e^2}{|\mathbf{r}_i - \mathbf{r}_j|} + \sum_i V_{ext}(\mathbf{r}_i). \tag{2.18}$$

2.0.2.1 Hohenberg-Kohn theorems

Theorem I: "For any system of interacting particles in an external potential $V_{ext}(\mathbf{r})$, the potential $V_{ext}(\mathbf{r})$ is determined uniquely, except for a constant, by the ground state particle density $n_o(\mathbf{r})$".

Corollary I: Since the Hamiltonian is thus fully determined, except for a constant shift of the energy, it follows that the many-body wavefunctions for all states (ground and excited) are determined. *Therefore all properties of the system are completely determined given only the ground state density* $n_o(\mathbf{r})$.

Theorem II: "A *universal functional* for the energy $E[n]$ in terms of the density $n(\mathbf{r})$ can be defined, valid for any external potential $V_{ext}(\mathbf{r})$. For any particular $V_{ext}(\mathbf{r})$, the exact ground state energy of the system is the global minimum value of this functional, and the

density $n(\mathbf{r})$ that minimizes the functional is the exact ground state density $n_o(\mathbf{r})$".
Corollary II: The functional $E[n]$ alone is sufficient to determine the exact ground state energy and density.
The Hohenberg-Kohn total energy functional (E_{HK}) for a given external potential $V_{ext}(\mathbf{r})$ is given by:

$$\begin{aligned} E_{HK}[n] &= T[n] + E_{e-e} + \int d^3r V_{ext}(\mathbf{r}) n(\mathbf{r}) \\ &\equiv F_{HK}[n] + \int d^3r V_{ext}(\mathbf{r}) n(\mathbf{r}), \end{aligned} \tag{2.19}$$

where, $F_{HK}[n]$ includes the kinetic T and interaction E_{e-e} energies of electrons.

$$F_{HK}[n] = T[n] + E_{e-e}[n]. \tag{2.20}$$

$F_{HK}[n]$ should be "universal" by construction since T and E_{e-e} depends only on electron density. These two theorems simplified the problem of evaluating the ground state properties of interacting particles by using the electron density based approach instead of wavefunction-based approach which has dependancy of 3N independent variables, N being the number of electrons. However, the functional form of $F_{HK}[n]$ is not known. In the following section, we explain a way proposed by Kohn and Sham to find this unknown functional.

2.0.2.2 Kohn-Sham ansatz

Kohn and Sham proposed an idea of finding the unknown functional [21]. Their proposal involves mapping of a complicated many body problem of interacting electrons to a simpler system of non-interacting electrons.
The assumptions are [22]:
1. The exact ground state density of a system of interacting particles can be represented by the ground state density of an auxiliary system of non-interacting particles.
2. The Hamiltonian for this auxiliary system of non-interacting single electrons will have the usual kinetic energy operator and an effective local potential acting on an electron at point $\mathbf{r}$. Using Hartree atomic units the auxiliary Hamiltonian can be written as:

$$\hat{H}_{aux} = -\frac{\nabla^2}{2} + V_{eff}(\mathbf{r}). \tag{2.21}$$

For an auxiliary system of N non-interacting electrons obeying the above Hamiltonian, the ground state has one electron in each of the N orbitals $\psi_i(\mathbf{r})$ with eigen values ϵ_i of the Hamiltonian. The electron density of the system is given by sums of squares of the orbitals

$$n(\mathbf{r}) = \sum_{i=1}^{N} |\psi_i(\mathbf{r})|^2, \tag{2.22}$$

the kinetic energy of non-interacting electrons T_o is written as:

$$T_o = \frac{1}{2} \sum_{i=1}^{N} \int d^3r |\nabla \psi_i(\mathbf{r})|^2, \tag{2.23}$$

and Coulombic interaction energy of the electron density $n(\mathbf{r})$ interacting with itself is defined as the Hartree energy given as:

$$E_{Hartree}[n] = \frac{1}{2} \int d^3r d^3r' \frac{n(\mathbf{r})n(\mathbf{r}')}{|\mathbf{r} - \mathbf{r}'|}. \tag{2.24}$$

Taking into account the above two assumptions, the HK functional had been re-written by KS as:

$$F_{KS}[n] = T_o[n] + E_{Hartree}[n] + E_{xc}[n]. \tag{2.25}$$

In the above equation, $T_o[n]$ is the kinetic energy of non-interacting electrons at their ground state as a function of electronic density distribution. E_H is the Hartree energy, and all many-body effects of exchange and correlation are merged into the exchange-correlation energy E_{xc}. The overall Hohenberg-Kohn ground state energy functional using the KS approach can be written in the form

$$\begin{aligned} E_{KS}[n] &= T_o[n] + \int d\mathbf{r} V_{ext}(\mathbf{r}) n(\mathbf{r}) + E_{Hartree}[n] + E_{xc}[n] \\ &\equiv F_{KS}[n] + \int d\mathbf{r} n(\mathbf{r}) V_{eff}(\mathbf{r}). \end{aligned} \tag{2.26}$$

In terms of Hohenberg-Kohn functional the E_{xc} can be written as:

$$E_{xc}[n] = F_{HK}[n] - (T_o[n] + E_{Hartree}[n]). \tag{2.27}$$

Here E_{xc} is defined as the difference between kinetic and interaction energies of interacting many body system from the non-interacting system with Hartree energy replacing the

electron-electron interactions. If the universal functional E_{xc} is known then Kohn-Sham approach can be used to calculate the ground state properties of many-body electron system.

The soultion of KS system for ground state is obtained by minimization of $E_{KS}[n]$ in Eqn 2.26 w.r.t electron density $n(\mathbf{r})$. T_o is a functional of orbitals Eqn 2.23 and other terms in Eqn 2.26 are functional of density of electrons, varying the wavefunctions can help derive the variational equation

$$\frac{\delta E_{KS}}{\delta \psi_i^*(\mathbf{r})} = \frac{\delta T_o}{\delta \psi_i^*(\mathbf{r})} + [\frac{\delta E_{ext}}{\delta n(\mathbf{r})} + \frac{\delta E_{Hartree}}{\delta n(\mathbf{r})} + \frac{\delta E_{xc}}{\delta n(\mathbf{r})}]\frac{\delta n(\mathbf{r})}{\delta \psi_i^*(\mathbf{r})} = 0, \tag{2.28}$$

under orthonormalization constraints

$$< \psi_i | \psi_j >= \delta_{i,j}. \tag{2.29}$$

Using the expressions for $n(\mathbf{r})$ and T_o in Eqns 2.22 and 2.23, gives

$$\frac{\delta T_o}{\delta \psi_i^*(\mathbf{r})} = -\frac{1}{2}\nabla^2 \psi_i(\mathbf{r}); \frac{\delta n(\mathbf{r})}{\delta \psi_i^*(\mathbf{r})} = \psi_i(\mathbf{r}), \tag{2.30}$$

and method of Lagrage multiplier, results to the Kohn-Sham Schrödinger equations:

$$(H_{KS} - \epsilon_i)\psi_i(\mathbf{r}) = 0, \tag{2.31}$$

where, ϵ_i are eigenvalues, and H_{KS} is KS hamiltonian

$$H_{KS}(\mathbf{r}) = -\frac{1}{2}\nabla^2 + V_{KS}(\mathbf{r}), \tag{2.32}$$

having

$$\begin{aligned} V_{KS}(\mathbf{r}) &= V_{ext}(\mathbf{r}) + \frac{\delta E_{Hartree}}{\delta n(\mathbf{r})} + \frac{\delta E_{xc}}{\delta n(\mathbf{r})} \\ &= V_{ext}(\mathbf{r}) + V_{Hartree}(\mathbf{r}) + V_{xc}(\mathbf{r}). \end{aligned} \tag{2.33}$$

Eqns 2.31, 2.32, and 2.33 are Kohn-Sham equations, with the ground state density $n(\mathbf{r})$ and total energy E_{KS} given by Eqns 2.22 and 2.26, respectively. These are independent-particle equations having potential found self-consistently from the density obtained. These equations results in ground state properties like electron density and energy for many body interacting system, if the form of functional $E_{xc}[n]$ is known. From Hohenberg-

Kohn theoerems, there exist a ground state density that uniquely evaluates the potential at minimum, such that there exist a unique KS potential for a given interacting system $V_{eff}(\mathbf{r})|_{min} \equiv V_{KS}(\mathbf{r})$. The Kohn-Sham equations need to be solved self-consistently because $V_{Hartree}$ and V_{xc} needs to be defined, which depends on the electron density $n(\mathbf{r})$, which further is given by single particle eigenstates ψ_i, which then in turn are estimated by these potentials. So, therefore to break this circle and to bring this into implementation interative method is used. To do this:

1. An initial guess of electron density, trial electron density n($\mathbf{r}$) is defined.
2. The Kohn-Sham equations are solved to get eigen states $\psi_i(\mathbf{r})$ according to Eqn 2.31.
3. On the basis of Eqn 2.22 the new electron density is calculated by summing over the occupied orbitals ψ_i.
4. Compare the new calculated electron density with the electron density used initially to solve KS equations. If the two matches, then this is the ground state density and is used to calculate the total energy. If not then again the trial density is updated and this process is repeated until convergence is achieved. Figure 2.1 shows steps involved in self-consistently or iteratively solving Kohn-Sham equations.

2.0.2.3 Exchange-correlation energy

Exchange interaction comes from Pauli's exclusion principle which states that no two electrons can have the same quantum state. Since the electrons are Fermions, the wave function must be antisymmetric for a many-body electron system undergoing the exchange of two electrons. This antisymmetry principle causes a spatial separation between the electrons of same spin and leads to reduction in the Coulomb energy of the many-body electronic system. This reduction in the electronic system's energy due to the wavefunction antisymmetry principle is defined as exchange energy. It is quite easy to include the exchange while total energy calculation, which is called as the Hartree-Fock approximation. The Coulomb energy can be reduced further below Hartree-Fock value if electrons of opposite spins also are spatially separated. The reduction in Coulomb energy is at the cost of kinetic energy increment of the electrons. The correlation energy is defined as the difference between the many-body energy of electronic system and energy of system calculated taking into account the Hartree-Fock approximation. Both exchange and correlation depend on the electron density. Hence, the exchange correlation energy functional

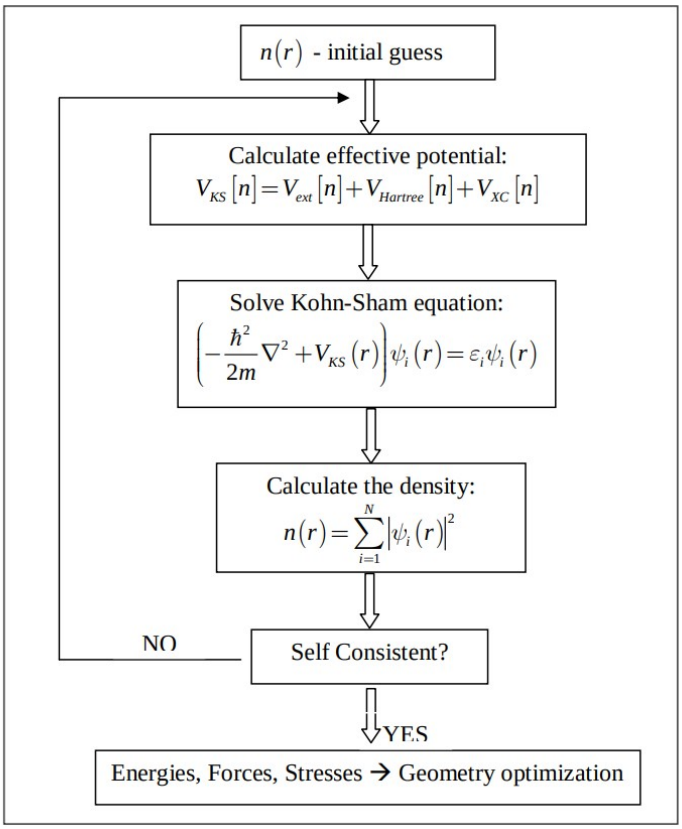


Figure 2.1: The steps involved in the self-consistent cycle to solve Kohn-Sham equations. Adapted with permission from Ref [2]

depends on the electron density only.

$$E_{xc}[n] = \int n(\mathbf{r})\epsilon_{xc}(n(\mathbf{r})).d\mathbf{r}, \tag{2.34}$$

here, in the above equation $\epsilon_{xc}([n(\mathbf{r})])$ is exchange-correlation energy per electron at point $\mathbf{r}$. In the above equation $\epsilon_{xc}([n(\mathbf{r})])$ functional is unknown. The search for an exact form of $\epsilon_{xc}([n(\mathbf{r})])$ functional is one of the challenge in DFT. There are ways in which this functional can be approximated.

Local Density Approximation(LDA): In this approximation the assumption made for the exchange-correlation energy is that it depends locally on the electronic density of system around a point $\mathbf{r}$ and this local electron density is supposed to be homogeneous. The exchange-correlation energy is estimated by taking into consideration the assumption

that the exchange-correlation energy per electron in the electron gas at point $\mathbf{r}$, $\epsilon_{xc}(\mathbf{r})$, is equal to that of exchange correlation energy per electron in a homogeneous electron gas having same density as the electron gas at point $\mathbf{r}$. The exchange-correlation energy given as [23]:

$$E_{xc}^{LDA}[n(\mathbf{r})] = \int n(\mathbf{r})\epsilon_{xc}(\mathbf{r}).d^3\mathbf{r}, \tag{2.35}$$

where $\epsilon_{xc}(\mathbf{r}) = \epsilon_{xc}^{hom}[n(\mathbf{r})]$ is the exchange correlation energy density of a homogeneous electron gas at $\mathbf{r}$. This approximation holds good for cases where density of electrons varies gradually with $\mathbf{r}$. Usually alkali and alkaline earth metals can be better dealt with this approximation. It produces well geometrical parameters, which matches with the experiment, overestimates binding energies, computes bond length much shorter than in experiments. To solve these problems within LDA, extensions of this approximation was introduced. Among them Generalized Gradient Approximation(GGA) is one of the most successful ones.

Generalized Gradient Approximation(GGA): Within GGA it is proposed that the exchange-correlation energy (E_{xc}^{GGA}) not only depends on local density but also on the local spatial variation of the density and its higher derivatives. In view of this, Eqn 2.35 is modified to:

$$E_{xc}^{GGA} = \int n(\mathbf{r})\epsilon_{xc}((\mathbf{r}), \nabla n(\mathbf{r}), \nabla^2 n(r).d\mathbf{r}, ...). \tag{2.36}$$

This approximation helps to improve some short comings of LDA. It also produces better results of the energy of binding, activation energy for the system. It helps to give better results for cases where LDA fails, like for transition metals. For example for bulk iron GGA correctly predicts the ground state to be ferromagnetic, which is in accordance with experiment, whereas LDA predicted it to be paramagnetic. [23]

2.0.3 Periodic supercells

In the preceding section we have discussed that using DFT one can reduce the computational efforts required for solving the many-body problem by mapping it into a single-particle problem. The first is to calculate wavefunction for each of the infinite number of electrons and the second difficulty is of infinitely large basis set required for expansion of each wavefunction, which spans through the entire solid. However there still is the issue of the requirement of an infinite basis set. Moreover, for solids, there are infinite number of ions and electrons. Hence for solids it is necessary to find infinite number of solutions.

The issue of the infinite size of solids can be solved by using Born-von karman periodic boundary condition that gives rise to a discrete set of quantum numbers. "k" that reside in the 1^{st} Brillouin Zone of the crystal. In the limit the crystal goes to infinity, "k" becomes continuous. However, we are solving the KS equations numerically. Hence, we always use a finite grid of k-points. Hence it is important to check the convergence of the desired properties with respect to the k-grid used in the calculations.

2.0.3.1 Bloch's theorem

In accordance with Bloch's theorem the wavefunction for each electron in a periodic solid is a product of wave-like part and cell-periodic part and can be written as:

$$\psi_i(\mathbf{r}) = e^{i\mathbf{k}.\mathbf{r}} f_i(\mathbf{r}), \tag{2.37}$$

where, $e^{i\mathbf{k}.\mathbf{r}}$ represents a plane wave of wave-vector, $\mathbf{k}$ and $f_i(\mathbf{r})$ is the periodic part of the Bloch's function that has the periodicity of the unit cell of the crystal. In our calculations the periodic part of the wave function in Eqn 2.37 has been expanded using plane wave basis set consisting of discrete set of plane waves having wave vectors G which are reciprocal lattice vectors, i.e:

$$f_i(\mathbf{r}) = \sum_G c_{i,G} e^{i\mathbf{G}.\mathbf{r}}. \tag{2.38}$$

Hence, each electronic wavefunction is written as sum of plane waves as given in the following equation:

$$\psi_i(\mathbf{r}) = \sum_{\mathbf{G}} c_{i,\mathbf{k}+\mathbf{G}} e^{i(\mathbf{k}+\mathbf{G}).\mathbf{r}}, \tag{2.39}$$

where, $c_{i,\mathbf{k}+\mathbf{G}}$ are co-efficients to the basis functions. The number of G vectors can be infinite in number making basis set infinitely large. This can be overcomed by truncating the infinite series. Those electronic wavefunctions are important which results in small kinetic energy. On operating the kinetic energy operator ($\hat{T} = -\frac{\hbar^2}{2m}\nabla^2$) on the wavefunction in Eqn 2.39 we get the expectation value of the kinetic energy operator (T) as,

$$< \psi_i(\mathbf{r})|T|\psi_i(\mathbf{r}) >= \frac{\hbar^2}{2m}|\mathbf{k}+\mathbf{G}|^2. \tag{2.40}$$

Hence, plane wave basis set or number of G to be truncated with only plane waves having kinetic energies less than certain cutoff energy (E_{cut}).

$$\frac{\hbar^2}{2m}|\mathbf{k}+\mathbf{G}|^2 < E_{cut}. \tag{2.41}$$

The convergence of total energy is checked so to fix the value of cutoff energy. Precisely, the value of E_{cut} is increased till total energy values are consistent upto minimum order of error.

2.0.4 Nonperiodic system

For finite systems like: Surfaces, interfaces, defects, etc. the translational symmetry of the crystal is broken in atleast one direction. To solve the KS equations using plane wave (PW) basis and within the framework of periodic boundary conditions for these systems the supercell method is used. Since this thesis involves calculations of surfaces where the periodicity is maintained in the plane of the surface and is broken in the direction perpendicular to the surface we discuss this case in this section.

Figure 2.2 demonstrates a supercell for such an aperiodic system; a surface where perpendicular direction to the plane of the surface shows no periodicity and plane of the surface exhibits periodicity. The supercell contains two regions, slab and vacuum region. Slab is infinite and periodic in the plane of the surface but finite in the direction perpendicular to the surface and vacuum is region between two consecutive slabs where there are no atoms. Since we are interested in the surface properties of the material the thickness of slab(determined by the number of layers) and vaccum region is important. The slab should be enough thick to minimize the interactions between its two surfaces through the bulk crystal. The number of layers in the slab are increased till the intermediate layers in the slab exhibits the bulk interplanar distances upon relaxation. The thickness of vacuum region should be large enough to avoid interaction between the periodic images.

2.0.5 Electron-ion interactions

Usually in an atom the core electron are highly localized compared to the valence electron. Hence, when two atoms come close to each other, they interact through the exponentially decaying tail of the wavefunction corresponding to the valence electron. Therefore, in our

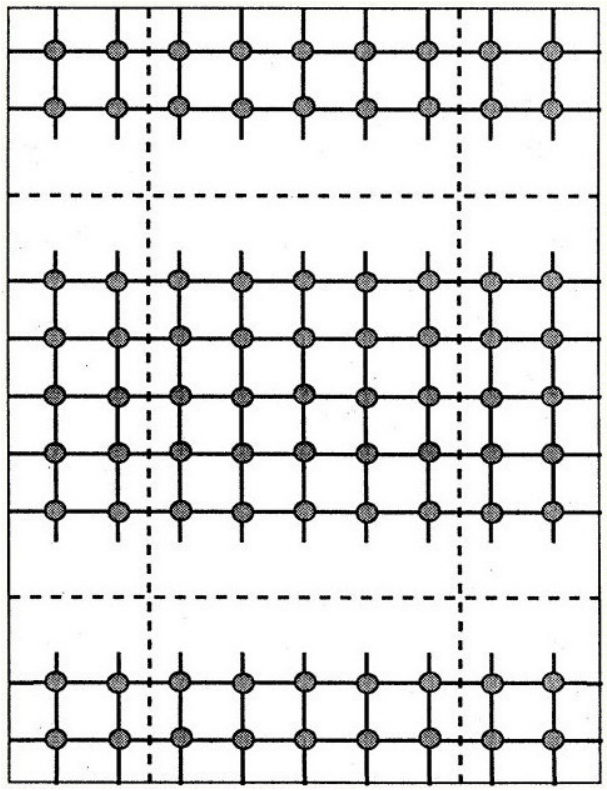


Figure 2.2: Pictorial representation of supercell for surface of solid. Adapted with permission from Ref [3]

calculations we consider only the valence electron. They see an effective nuclear charge that is screened by the core electron. Moreover, the Coulomb potential between the electron and the ion diverges near the nucleus, which is difficult to handle numerically. Hence, the Coulomb potential is approximated by a fictitious potential that has a non-diverging form near the nucleus. At distances away from the nucleus (r_c in Figure 2.3) it is ensured that this potential matches with the actual potential as shown in Figure 2.3. This is called the pseudopotential approximation. The removal of the core electron reduce the computational cost while the pseudopotential helps in handling the numerical issue of divergence of the actual effective potential at the nuclei.

Additionally the valence electron have large oscillations as one moves towards the nuclei. As a consequence, to expand such an oscillating wavefunction in a PW basis would require enormous number of plane waves, hereby increasing the computational cost. Hence, the actual wavefunction is replaced with a pseudo-wavefunction that matches

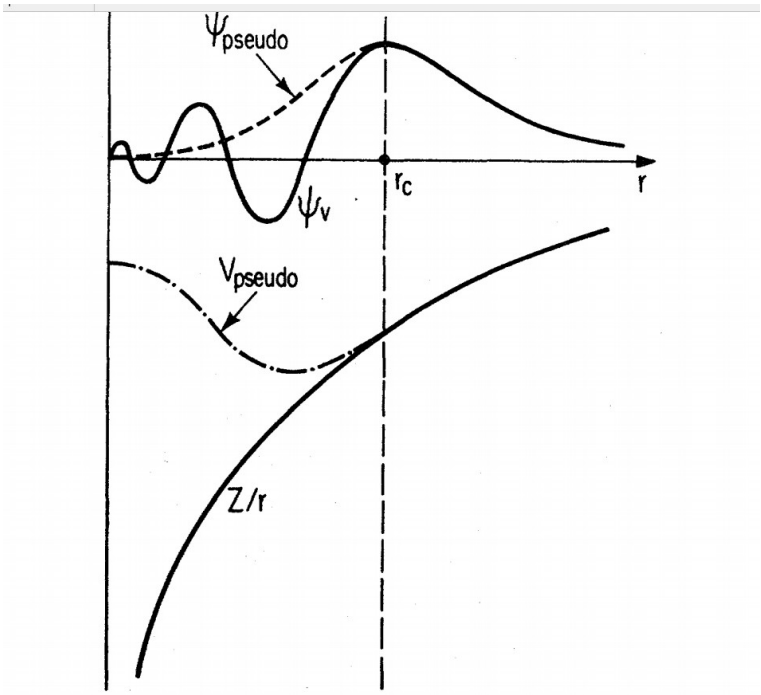


Figure 2.3: Pictorial representation of all-electron and pseudoelectron potentials. Adapted with permission from Ref [3]

exactly with the actual wavefunction beyond a cutoff radius r_c (see Figure 2.3) while at distances smaller than r_c they are approximated by a smoothly varying function. Thus smaller the value of r_c, larger is the requirement for basis set and more expensive is the calculation.

The pseudopotentials used can be classified primarily in two classes: norm-conserving and ultrasoft pseudopotentials. In the norm-conserving pseudopotentials, the norm of pseudo-wavefunction in core region is equal to norm of all-electron wavefunction. The "norm-conservation" concept makes the application of pseudopotential easy, more accurate but requires high cutoff energy and is hard pseudopotential. In ultrasoftpseudopotential (USPP), introduced by David Vanderbilt [24], the norm conserving condition is relaxed. Hence one can use very low energy cutoffs resulting in a relatively small basis set. Moreover implementation of USPP in codes also become complicated.

2.0.6 Computation of vibrational frequencies

Using DFT calculations, one can optimize the structure of surfaces, molecules, and bulk solids. It also helps us to predict useful properties of materials. Hence, DFT calculations are termed as: "*zero temperature approach*" i.e it computes the properties of materials in which the atoms are at their equilibrium position corresponding to a temperature of 0 K. Additionally, the nuclei are treated as classical particles. However, the quantum nature of the nuclei results in delocalization of the nuclei, which is manifested through zero-point energy (ZPE). ZPE can be computed from the knowledge of the vibrational frequency of the system and is given a:

$$E_{ZPE} = \frac{1}{2}\sum_{i} h\nu_i, \tag{2.42}$$

where, ν_i is the frequency of the i^{th} vibrational mode. In this section, we will see how to get information about the properties of materials at non zero temperature. When a material is raised to some non-zero temperature, the atoms will vibrate about their equilibrium positions. In terms of quantum mechanical perspective, the vibrations around an atom's equilibrium position has contribution to material's energy even at 0 K via zero-point energies. Zero-point energy effects are particularly important in systems involving light atoms like hydrogen, for example, in case of H adsorbed on Cu(100) surface consisting of two interstitial sites (octahedral and tetrahedral), showed that ZPE alters the relative stabilities of these two sites [25]. Hence, if we are interested in energy difference between different sites involving light atoms it is necessary to include zero-point energies, which are computed from the vibrational frequency. Moreover, the vibrational frequencies can also help us determine the dynamic stability of a structure. The vibrational frequency associated with different vibrational modes like symmetric stretching, asymmetric stretching and bending act as finger prints for molecules. Experimentally the frequencies of the vibrations are obtained using Raman, IR or Brillouin spectroscopy. In this section we aim to show vibrational frequencies can be computed from DFT.

2.0.6.1 Computation of Phonons from density functional perturbation theory

The energy associated with lattice vibrations (collective oscillations of ions) are quantized and a quanta of this energy is called phonon. The information about the phonons of a material can help us understand some of the physical properties of a material like for example vibrational spectra, thermal expansion, structural stability and thermal con-

ductivity of the lattice etc. The introduction of Density Functional Perturbation Theory (DFPT) [26], which is based on linear response theory have made feasible for systems containing atoms huge in number, to carry out *ab initio calculations* of vibrations in a lattice.

2.0.6.2 Lattice dynamics from electronic-structure theory

Under the BO approximation, the dynamical properties of a lattice in a system are evaluated by eigenvalues E_{tot}, eigenfunctions Ψ_{nj} of the Schrödinger equation which is given below:

$$(-\sum_{I} \frac{\hbar^2}{2M_I} \frac{\partial^2}{\partial \mathbf{R}_I^2} + E_j(\mathbf{R}))\Psi_{nj}(\mathbf{R}) = E_{tot}\Psi_{nj}(\mathbf{R}), \tag{2.43}$$

here, in the above equation $\mathbf{R}_I$ is the I^{th} nucleus coordinate, M_I is the mass of the I^{th} nucleus, $\mathbf{R} \equiv \{\mathbf{R}_I\}$ is the set of nuclear coordinates and $E_j(\mathbf{R})$ is total-ion energy of system, called as the *Born-Oppenheimer energy surface*. The $E_j(\mathbf{R})$ is the energy corresponding to the ground state of interacting electrons moving under fixed nuclei field, and it's Hamiltonian depending only parametrically on $\mathbf{R}$ given as:

$$H_{BO}(\mathbf{R}) = -\frac{\hbar^2}{2m}\sum_{i} \frac{\partial^2}{\partial \mathbf{r}_i} + \frac{e^2}{2}\sum_{i \neq j} \frac{1}{|\mathbf{r}_i - \mathbf{r}_j|} - \sum_{i,I} \frac{Z_I e^2}{|\mathbf{r}_i - \mathbf{R}_I|} + E_N(\mathbf{R}), \tag{2.44}$$

here, the first term is kinetic energy of electrons, second term is potential energy due to electrons-electrons interactions, third term is potential energy of electrons-nuclei interactions, Z_I is the atomic number of the I^{th} nucleus, -e is the electronic charge and $E_N(\mathbf{R})$ is the potential energy due to nuclei-nuclei repulsions:

$$E_N(\mathbf{R}) = \sum_{I,J;I>J} \frac{1}{4\pi\epsilon_0} \frac{Z_I Z_J e^2}{|\mathbf{R}_I - \mathbf{R}_J|}. \tag{2.45}$$

The condition to obtain the equilibrium geometry of the system is that the forces acting on all individual nuclei should disappear:

$$\mathbf{F}_I \equiv -\frac{\partial E(\mathbf{R})}{\partial \mathbf{R}_I} = 0, \tag{2.46}$$

and the frequency of vibrations ω are evaluated using the eigenvalues corresponding to the Hessian matrix of the Born-Oppenheimer potential energy surface , by scaling of their

nuclear masses.

$$det|\frac{1}{\sqrt{M_I M_J}}\frac{\partial^2 E(\mathbf{R})}{\partial \mathbf{R}_I \partial \mathbf{R}_J} - \omega^2| = 0. \tag{2.47}$$

The computation of first and second derivatives of the Born-Oppenheimer energy surface is required to calculate the equilibrium geometry and vibrational properties of the sysytems. To accomplish this task the basic tool used is the Hellmann-Feyman theorem (Hemmmann, 1937; Feyman, 1939) [27]. The Hellmann-Feyman theorem states that the first derivative of eigenvalues of Hamiltonian, H_λ, depending on the parameter λ, with respect to the parameter is given by the expectation value of the Hamiltonian derivative:

$$\frac{\partial E_\lambda}{\partial \lambda} = < \Psi_\lambda | \frac{\partial H_\lambda}{\partial \lambda} | \Psi >, \tag{2.48}$$

where Ψ_λ is eigenfunction of H_λ Hamiltonian with E_λ eigenvalue obeying Schrödinger equation: $H_\lambda \Psi_\lambda = E_\lambda \Psi_\lambda$. In accordance with Born-Oppenheimer approximation, coordinates of the nuclei act parametrically on the electronic Hamiltonian as in Eqn 2.44. The force on the I^{th} nucleus in ground state of electrons is:

$$F_I = -\frac{\partial E(\mathbf{R})}{\partial \mathbf{R}_I} = - < \Psi(\mathbf{R}) | \frac{\partial H_{BO}(\mathbf{R})}{\partial \mathbf{R}_I} | \Psi(\mathbf{R}) >, \tag{2.49}$$

here $\Psi(\mathbf{R})$ is the ground state electronic wavefunction of Hamiltonian of Born-Oppenheimer. The Born-Oppenheimer Hamiltonian has dependancy on nuclear coordinate $\mathbf{R}$ via interaction beween nuclei and electrons that couples with electronic degrees of freedom only through the electron charge density. The Hellmann-Feyman theorem in this case states that

$$\mathbf{F}_I = -\int n_{\mathbf{R}}(\mathbf{r}) \frac{\partial V_{\mathbf{R}}(\mathbf{r})}{\partial \mathbf{R}_I} d\mathbf{r} - \frac{\partial E_N(\mathbf{R})}{\partial \mathbf{R}_I}, \tag{2.50}$$

here, $V_{\mathbf{R}}(\mathbf{r})$ is the interaction between electron and nucleus, and $n_{\mathbf{R}}(\mathbf{r})$ is the ground-state electron charge density for nuclear configuration $\mathbf{R}$.

$$V_{\mathbf{R}}(\mathbf{r}) = -\sum_{iI} \frac{Z_I e^2}{|\mathbf{r} - \mathbf{R}_I|}, \tag{2.51}$$

and $n_{\mathbf{R}}(\mathbf{r})$ is the ground-state electron charge density for nuclear configuration $\mathbf{R}$. The Hessian of the BO energy surface appearing in Eqn 2.47 is calculated by differentiation

of Hellmann-Feyman forces with respect to nuclear coordinates,

$$\frac{\partial^2 E(\mathbf{R})}{\partial \mathbf{R}_I \partial \mathbf{R}_J} \equiv -\frac{\partial \mathbf{F}_I}{\partial \mathbf{R}_J} = \int \frac{\partial n_{\mathbf{R}}(\mathbf{r})}{\partial \mathbf{R}_J} \frac{\partial V_{\mathbf{R}}(\mathbf{r})}{\partial \mathbf{R_I}} d\mathbf{r} + \int n_{\mathbf{R}}(\mathbf{r}) \frac{\partial^2 V_{\mathbf{R}}(\mathbf{r})}{\partial \mathbf{R}_I \partial \mathbf{R}_J} d\mathbf{r} + \frac{\partial^2 E_N(\mathbf{R})}{\partial \mathbf{R}_I \partial \mathbf{R}_J}. \tag{2.52}$$

For the calculation of the Hessian corresponding to the Born-Oppenheimer energy surface, one needs to know the ground state electron charge density $n_{\mathbf{R}}(\mathbf{r})$ and its linear response to a distortion of the nuclear geometry i.e $\frac{\partial n_{\mathbf{R}}(\mathbf{r})}{\partial \mathbf{R}_I}$, which can be computed using DFPT. The detailed derivation of how to compute the linear response is given in Ref [26].

2.0.7 Nudged Elastic Band (NEB) Method

The study of the chemical reactions at the surfaces of transition metals is a topic of extreme importance because of the technological relevance these reactions have for the society. Activated processes such as oxidation, permeation discussed in this thesis are used in the industry, involving chemical and physical phenomenon at the surfaces of transition metals. The difficulty lies in the calculation of their transition rates, like rates of chemical reactions asscociated with these processes. In regular practise, it is possible to treat the atomic motion using the classical mechanics, but the transitions of our interest are much slower than the normal vibration of atoms, so standard molecular dynamics simulations are not practical. Hence, in the field of computational chemistry the rate of an activated process is usually calculated using harmonic transition states theory (HTST) defined as,

$$k_{hTST} = \frac{\Pi_{i=1}^{3N} \nu_i^{init}}{\Pi_{i=1}^{3N-1} \nu_i^*} exp(\frac{-\Delta E}{k_B T}), \tag{2.53}$$

where, $\Delta E = E^* - E^{init}$ with E^* energy of the 1^{st} order saddle point, E^{init} is the potential energy minimum corresponding to the initial state. ν_i are the normal mode frequencies. All these quantities can be evaluated from the potential energy surface at zero temperature. The most difficult part is the search for the saddle point.

2.0.7.1 Minimum energy path (MEP) and saddle point estimation

The path connecting the initial and final state with greatest statistical weight is defined as the minimum energy path (MEP). The saddle point estimation is one of the challenges because the first order saddle point is the minimum in all directions except one along which

it is maximum. There are various methods availaible for finding the MEPs and the saddle point. The drag method [28], NEB method [29], CI-NEB method [30], the conjugate peak refinement (CPR) method [31], and the Dewar, Healy and Stewart (DHS) method [32] are some of the examples for methods used to estimate the saddle point. These above methods involves maximization of one degree of freedom while all the other degrees of freedom are minimized. All the MEPs and saddle points in this thesis are estimated using CI-NEB method [5]

The NEB method to estimate the MEP can be used if the initial and final state of the sysytem is known. At first, a path is constructed using string of images(replicas of the system) connected together with springs of zero rest-length starting from the initial state (reactant configuration) to the final state (product configuration). Using an optimization algorithm these images are then relaxed down to the MEP. If $[\mathbf{I}_0, \mathbf{I}_1, \mathbf{I}_2, ..., \mathbf{I}_N]$ denote string of images with initial $(\mathbf{I}_o)$ and final $(\mathbf{I}_N)$ states fixed, then the optimization algorithm will adjust the $N-1$ images to MEP. The easy approach is to construct an objective function and minimize it with respect to N-1 intermediate images,$(\mathbf{I}_1, ..., \mathbf{I}_N)$. [33]

$$S(\mathbf{I}_1, ...\mathbf{I}_N) = \sum_{i=1}^{N-1} E(\mathbf{I}_i) + \sum_{i=1}^{N} \frac{k}{2}(\mathbf{I}_i - \mathbf{I}_{i-1})^2 \tag{2.54}$$

The expression above mimics an elastic band made by $N-1$ beads and N springs with spring constant k. The two major problem with this formulation are: $1)$ for curved regions of the MEP, the elastic band tends to cut corners and gets pulled off the MEPs by the spring forces due to the perpendicular component of the spring force to the path. $2)$ the images close to the saddle point tend to slide down towards the fixed endpoints (initial and final states) resulting in low resolution of the region near saddle point, due to the parallel component of the true force (arising because of the interaction between atoms). These two problems stated above can be solved with force projection scheme referred to as 'nudging'.
According to the force projection scheme, the true forces act perpendicular to the band and the spring forces act parallel to the band. On the basis of these force projections the images are then relaxed towards the MEP. The force projection scheme as shown in Figure 2.4 is carried out by estimating the tangent along the path $\hat{\tau}$ as shown in Figure 2.4, defined as the unit vector pointing the neighboring high energy image. The NEB force, $\mathbf{F}_i^{NEB}$ (shown in Figure 2.4) on each image is the sum of the perpendicular component of

true force and parallel component of the spring force given as, [4]

$$\begin{aligned} \mathbf{F}_i^{NEB} &= \mathbf{F}_i^{\perp} + \mathbf{F}_i^{s\parallel} \\ &\equiv -\nabla E(\mathbf{I}_i)|_{\perp} + \mathbf{F}_i^{s}.\hat{\tau}_i\hat{\tau}_i, \end{aligned} \tag{2.55}$$

where $-\nabla E(\mathbf{I}_i)|_{\perp}$ is the gradient of energy with respect to coordinate of atoms in the system at i^{th} image and $\mathbf{F}_i^s$ is the spring force on image i. By subtracting the parallel component we get the perpendicular component of the gradient as,

$$\nabla E(\mathbf{I}_i)|_{\perp} = \nabla E(\mathbf{I}_i) - \nabla E(\mathbf{I}_i).\hat{\tau}_i\hat{\tau}_i \tag{2.56}$$

To ensure spacing between the images when using same spring constant k for all the spring, spring force calculated as,

$$\mathbf{F}_i^{s\parallel} = k(|\mathbf{I}_{i+1} - \mathbf{I}_i| - |\mathbf{I}_i - \mathbf{I}_{i-1}|).\hat{\tau}_i \tag{2.57}$$

Figure 2.4 shows schematic representation of how force projection helps the NEB to find MEP.

2.0.7.2 Climbing Image Nudged Elastic Band Method(CI-NEB)

The CI-NEB method ensures the highest energy image in a path to be the saddle point and differs from the regular NEB method discussed above in one aspect. After performing some iterations with NEB, image having the highest energy is identified, i_{max}. Force on this one image is modified as given below [5]:

$$\begin{aligned} \mathbf{F}_{i_{max}} &= -\nabla E(\mathbf{I}_{i_{max}}) + 2\nabla E(\mathbf{I}_{i_{max}})|_{\parallel} \\ &= -\nabla E(\mathbf{I}_{i_{max}}) + 2\nabla E(\mathbf{I}_{i_{max}}).\tau_{i_{max}}\tau_{i_{max}} \end{aligned} \tag{2.58}$$

The full force on the highest energy image is due to the potential with component along the elastic band inverted, given by Eqn 2.58. The highest energy image is made to climb to the saddle point by applying a force along the tangent. In this method the highest energy image in the path feels no spring forces at all. Hence, the lay out of the images is non uniform on both (left and right) side of the potential energy surface, as it moves up towards the saddle point. Once, the MEP is obtained on the convergence of the CI-NEB, the convergence of climbing image to exact saddle point is also obtained. There should be sufficient number of images near to the saddle point, as to get a good guess of the collective

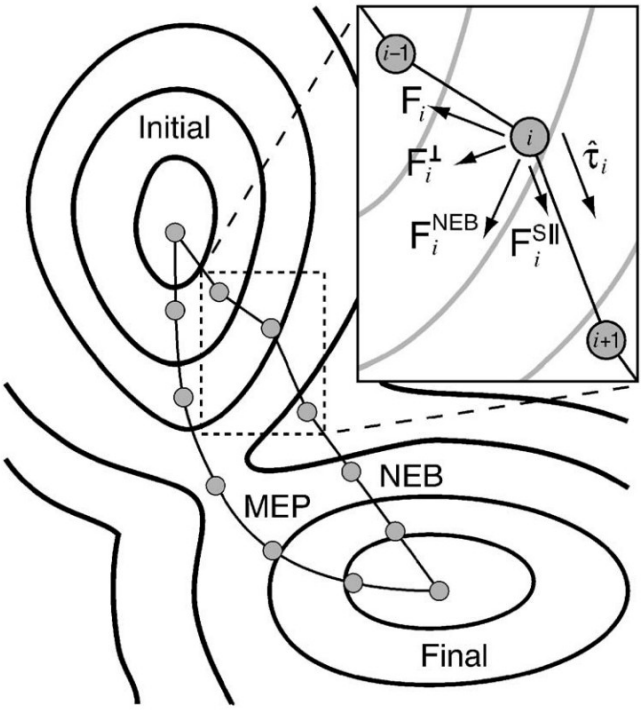


Figure 2.4: Schematic representation of NEB and force projection. $\mathbf{F_i}$ is the force on image i, $\mathbf{F}_i^s|^{\parallel}$ is spring force on image i and $\mathbf{F}_i|^{\perp}$ is perpendicular force on image i. Adapted with permission from Ref [4]

variables describing the transition process. Figure 2.5 shows comparison of regular NEB calculation and a climbing image NEB calculation where due to low resolution of the barrier, activation energy is underestimated by regular NEB. The climbing image NEB where one of the image is brought right to the saddle point and it also precisely gives the activation energy.

2.0.8 *Ab initio* Atomistic Thermodynamics

Stability of different surfaces, both clean and in the presence of adsorbate at various coverages, can be determined based on their free energies. In order to account for the effect of varying gas-phase temperature and pressure on the stability of a surface configuration, we apply concepts from classical thermodynamics. The free energy (F) of a system gives a measure of stability of the system. In the grand-canonical ensemble (GCE), assuming that the surface is in equilibrium with the adsorbates, the Gibbs free energy (F) is given

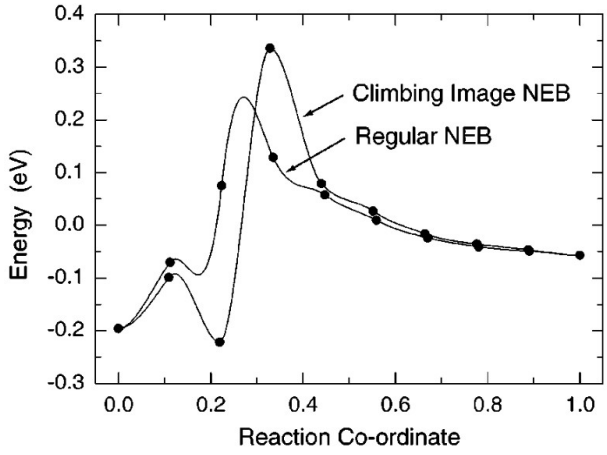


Figure 2.5: Pictorial representation of MEP by NEB and CI-NEB method. Adapted with permission from Ref [5]

by Eqn below.

$$F = E + PV - TS - \sum_i n_i \mu_i \tag{2.59}$$

where P, V, T and S are the pressure, volume, temperature and entropy, respectively. n_i and μ_i are, respectively, the number of molecules and the chemical potential of species i at the surface. E is the internal energy of the system and is obtained from the DFT calculations. In order to apply these concepts, one needs to have a clear distinction between what we consider as "system" and that which we take to be its "surroundings". In this thesis while studying thermodynamic analysis the system is considered to include the surface, the adsorbed molecules on the surface and the gas above the surface; the surroundings include only the world beyond some external gas container. Taking this view, the number of particles in the system is now fixed but the entropy is considerably large, since it includes large translational and rotational contributions from the gas molecules which are not adsorbed on the surface. Hence Eqn 2.59 is modified as

$$F^s = E + PV - TS \tag{2.60}$$

Now we calculate the necessary free energy that must be minimized. This can be done by defining free energies relative to that of the surface without X adsorbate. The change

in free energy upon adsorption with respect to the clean surface is given by:

$$\delta F^s = \frac{F^s_{slab+X} - F^s_{slab} - (n_X/2)F^s_X}{N_s} \tag{2.61}$$

where F^s_{slab}, F^s_{slab+X} and F^s_X are the free energies of the clean surface, of surface in presence of the adsorbate and of the adsorbed molecule in gas phase respectively. n_X and N_s denote the number of atoms adsorbed on the surface and the number of (1×1) surface unit cells respectively. To evaluate the free energy of the solid phases, i.e. F^s_{slab+X} and F^s_{clean}, we ignore the effects of TS (because entropy of the solid phase is negligible compared to that of the gas phase) and PV. With all these approximations the free energy of the solid phases equals the internal energy obtained from the DFT calculations.

For X in the gas phase, PV is obtained by assuming that the gas phase obeys the ideal gas equations. In order to compute the contribution of TS to F^s_X for the X in gas phase at different temperatures and pressures we can take the values of S at a pressure of 1 bar and for a temperature range of 300-1500K from the CRC handbook [62]. We then can derive the variation of S with pressure and temperature from the following formula:

$$S(T,P) = S(T,P^o) - Rln(p/p^0) \tag{2.62}$$

p^o(=1 bar) is the reference pressure and R is the universal gas constant. A plot of δF^s as a function of different pressures is obtained. The temperature at which the crossover in the stability occurs for different surfaces as a function of pressure can be estimated and based on this we can plot the pressure vs temperature phase diagrams.

Chapter 3

Electronegativity difference as a descriptor for oxidation inhibiting effect of alloying element during early stages of titanium oxidation

Degradation of mechanical properties of α-titanium, which is used to manufacture parts of jet engines, due to high temperature oxidation is detrimental for the engine components. Therefore, to overcome this problem there are ongoing endeavours to develop novel oxidation resistant titanium alloys and improve the properties of the existing ones. In an effort to understand the effect of alloying on oxidation of α-Ti(0001) surface and to identify descriptors for rational design of oxidation resistant alloys, in this work, using density functional theory based calculations, we have studied oxygen sorption and surface to sub-surface diffusion on pure and alloyed α-Ti(0001) surfaces. Zr, Hf, Nb, and Mo from the d-block and Al, Ga, Si, and Ge from the p-block were used as alloying elements. We find that the alloying elements prefers to segregate on the surface compared to the sub-surface layers. Our calculations show that the diffusion barrier correlates with the difference in the electronegativity between the alloying element and Ti. Elements, which are more electropositive than Ti are found to hinder the oxygen dissolution in Ti and vice-versa. We propose that the electronegativity difference can act as a good descriptor for choosing alloying elements. Our results are in reasonably good agreement with experimental reports on growth of oxide layers on these alloyed Ti surface.

3.1 Introduction

Titanium and its alloys are marked by their good fatigue strength, lightweight, relatively low Young's modulus and low densities. As a result, they possess high specific

strength that makes them a preferred candidate for constructing lighter and stronger structures [36,37]. Moreover, α-type Ti alloys could resist moderately high temperatures without creeping. As a consequence, they are used for manufacturing different parts of jet engines. However, at the high operating temperatures of jet engines, these alloys are prone to oxidation. The mechanical properties of the alloys deteriorate over time as the oxide layer thickness is increased. This leads to failure of critical components of jet engines, especially those with thin sections [38, 39]. Hence, it is imperative to develop oxidation resistant Ti-alloys with the above mentioned mechanical properties.

The first step towards development of such alloys is to understand the high temperature oxidation of Ti and how this is affected after alloying. On the experimental front, oxidation of Ti and its alloys had been widely studied. For example, Stringer [40] and Kofstad et al. [41, 42] studied high temperature (800-1200°C) oxidation of Ti using oxidation rate measurements and X-ray diffraction. From their study of oxidation of pure α-Ti(0001) surface at room temperature using low energy electron diffraction (LEED) and Auger electron spectroscopy (AES), Shih et al. [43] proposed that the oxidized state is probably TiO and not TiO_2. Studies on the oxidation kinetics of Ti films and diffusion kinetics of oxygen in α-Ti have also been reported [44, 45]. The effect of different alloying elements on the tensile strength and oxidation properties of α- and near α-Ti alloys has been outlined experimentally by Kitashima et al. [46] The role of these elements toward the oxidation resistance of Ti was reported by Kitashima and Kawamura [47]. It was observed that Ge decreases the oxidation resistance of Ti-alloys, while the addition of Hf increases the oxidation resistance [46, 48, 49].

In contrast, on the computational front, there are fewer studies. Schneider et al. [50] used first-principles based molecular dynamics simulations to study the formation of oxide layer on TiO_2 surface. From their simulations they could observe the formation of the TiO layer as inferred by Shih et al. The first step towards Ti oxidation is the interaction of the Ti surface with oxygen. This is followed by diffusion of the surface oxygen to subsurface. Density functional theory (DFT) based studies of sorption and diffusion of O in Ti(0001) by Liu et al. showed when O coverages exceeds 0.5 ML, O starts occupying the subsurface sites [48]. Ohler et al. used DFT to study the TiO_2/Ti interfaces [51]. Their work showed that mixing of bulk phases of Ti and TiO_2 is thermodynamically favourable. Wu et al. studied diffusion of atomic O through bulk Ti [39]. As opposed to pure Ti, there are even fewer studies on Ti-alloys. Bhattacharya et al. studied the oxidation mechanism of Si segregated α-Ti surfaces. [52, 53] DFT based study on oxidation thermodynamics of

Nb-Ti alloys were recently reported by Samin et al. [54]

For rational design of novel oxidation resistant alloys it is not only important to understand the effect of the alloying element on oxygen adsorption and its diffusion from surface to subsurface but also to correlate the oxidation inhibiting properties of the alloys with the physicochemical properties of the alloying element. In this work, in an effort to understand the result of alloying on the early stages of oxidation, we have studied oxygen adsorption and surface to subsurface diffusion in pure and alloyed α-Ti. In particular, we have considered alloying with d-block (Zr, Hf, Nb, and Mo) and p-block (Al, Ga, Si, and Ge) elements. We note that these are the most widely studied alloying elements for Ti. [46, 48, 49] Additionally, in an endeavour to rationally choose the alloying element we have also determined correlations between physicochemical properties of the alloying element and diffusion barriers. The rest of the chapter is divided as follows: Section 4.2 contains the details of the DFT calculations and the slab model used to study the surfaces. The results of our calculations are described in Section 4.3. Finally we summarize our results and conclude in Section 4.4.

3.2 Materials and Methods

All the calculations were performed using the Quantum ESPRESSO (QE) software, which is the plane wave-based implementation of DFT [55]. The electron-ion interactions were described using ultrasoft pseudopotentials [56], while the electron-electron exchange and correlation potential was described using Perdew, Burke and Ernzerhof (PBE) parametrization of the generalized gradient approximation (GGA) [57]. Kinetic energy cut offs of 45 and 360 Ry were employed for the wave function and charge density, respectively. Brillouin zone (BZ) integrations were performed with (18×18×6) shifted Monkhorst-Pack [58] k-grid for bulk α-Ti. To speed up the convergence we have used Marzari-Vanderbilt smearing with a smearing width of 0.008 Ry [59]. α-Ti in its bulk form exists in a hexagonal close packed crystal structure. Our calculated lattice parameters a and c for bulk α-Ti are 2.92 and 4.63 Å, respectively, which are in reasonably good agreement with the previously reported computed (2.92 Å and 4.63 Å) [48, 52, 60] and experimental values (2.95 Å and 4.68 Å) [61].

The (0001) surface was modelled using an asymmetric eleven layer Ti slab (Figure 3.1(a)), of which the bottom four layers were kept fixed at the bulk inter-planar distance while other atoms were allowed to relax. We have used a vacuum of 16 Å along the [0001]

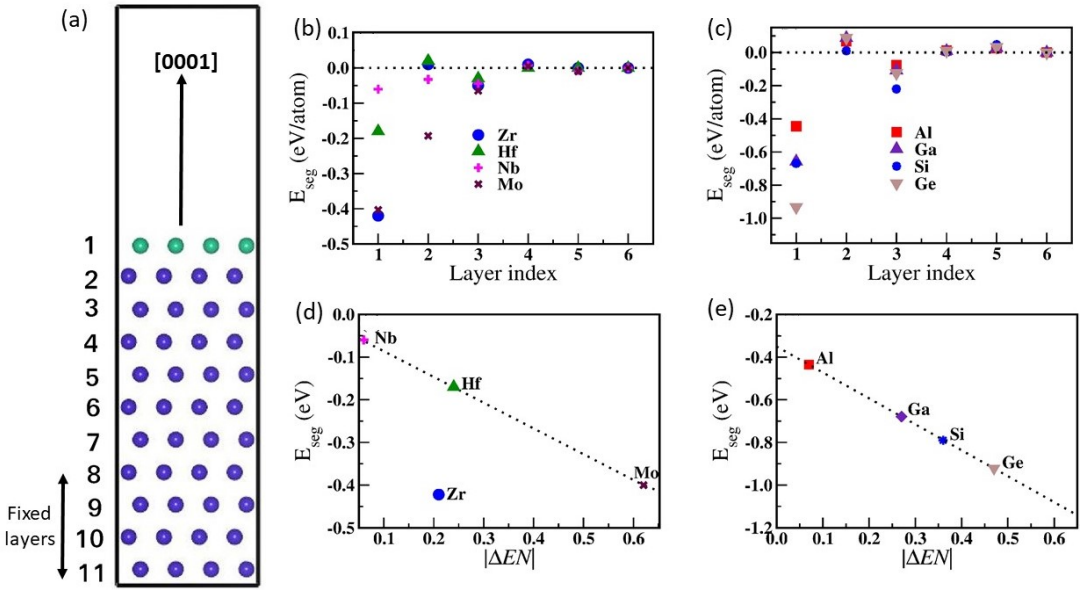


Figure 3.1: (a)The α-Ti(0001) surface model. The green spheres represent the surface Ti atoms while the blue spheres represent the Ti atoms in the other layers below surface. Variation of segregation energy E_{seg} as a function of the position of the alloying element in different layers for (b) d-block and (c) p-block elements. Variation of (E_{seg}) as a function of $|\Delta EN|$ for the (d) d-block and (e) p-block elements.

direction to minimize the fictitious interaction between the slab and its periodic images. In the experimental studies reported in Ref. [46] 4.0 at% of Al, Sn, Ga, Zr, Hf and 0.09 - 1.0 at% of Nb, Mo, W, Si, Ge were added to Ti to form the alloys. Based on this, to have a realistic and also computationally feasible model system, we considered Ti alloyed with 6.67% of the alloying element. To model this we have used a 4×4 surface supercell. At this point we would like to point out that in this work we have ignored the effect of defects like grain boundaries, vacancies, dislocations, etc. that might influence the segregation spots for alloying elements as well as paths for oxygen diffusion depending on their concentration. For the supercells BZ integrations were performed using the Γ-point only to reduce the computational cost. Since we are interested in differences of energy, to check the accuracy of our calculations, we have computed the difference in O adsorption energies at 0.50 and 1.00 ML oxygen coverage on Ti(0001) surface with only Γ-point and with a $4\times4\times1$ k grid. From our calculations we found out that this difference computed with Γ-point is 0.43 eV while that computed with the $4\times4\times1$ k-grid is 0.41 eV. This suggests that our approximation of using Γ-point only for BZ integration is reasonably accurate.

In order to understand the stability of the adsorbed oxygen atom on the pure and

alloyed Ti(0001) surfaces, we have calculated the adsorption energy (E_{ads}), which is given as:

$$E_{ads} = E_{O+surf} - E_{surf} - \frac{1}{2}E_{O_2} \tag{3.1}$$

where E_{O+surf}, E_{surf}, and E_{O_2} are the total energies of the system containing the surface and the adsorbed species, the clean surface and O_2 molecule in the gas phase, respectively. To compute the above energies we have carried out spin-polarized calculations for both pure and alloyed Ti(0001) surfaces involving oxygen for both oxygen adsorption and oxygen dissociation cases. Moreover, climbing image based nudged elastic band (CI-NEB) method [5, 10, 11] was used to compute the minimum energy path and barriers for the diffusion of O atoms from surface to subsurface layer. Depending on the path, we have used 7-12 images for the CI-NEB calculations.

3.3 Results and Discussion

3.3.1 Effect of alloying on properties of Ti(0001) surface

As mentioned in the introduction, we have studied the effect of alloying by Zr, Hf, Nb, and Mo that are d-block elements and Al, Ga, Si, and Ge that are p-block elements. The alloying elements can either be present in the bulk of Ti or on the (0001) surface/subsurface. To determine the thermodynamically favourable occupation site of the alloying element we substituted one Ti atom in each layer at a time. We carried out this substitution from layer 6 in the Ti slab (Figure 3.1(a)) to the surface layer. At layer 6, we observe that the interplanar distance is very close to that of bulk. Hence substituting a Ti atom in layer 6 is a reasonably good approximation of the alloying element occupying the bulk site. Using the energy of this configuration as reference, we define the segregation energy (E^i_{seg}) as:

$$E^i_{seg} = E_{X,i} - E_{X,6} \tag{3.2}$$

where $E_{X,i}$ and $E_{X,6}$ are the total energies when the alloying element X replaces a Ti atom in the i^{th} layer ($i \geq 6$) and 6^{th} layer respectively. According to Eqn. 3.2, when the alloying element is in bulk E_{seg} is zero. A negative value of E^i_{seg} indicates that it is more favourable for the alloying element to occupy that layer.

The variation of E_{seg} as a function of their position in the slab for the d and p-block alloying elements are shown in Figure 3.1(b) and (c) respectively. We find that for all the cases the alloying element prefers to be present on the surface. Moreover, E_{seg} for d-block

elements are in general smaller than that of the p-block ones.

E_{seg} is a measure of the stability of the configuration where the alloying element replaces a surface Ti atom. Amongst several factors, the difference in electronegativity between the alloying element and Ti can be an indicator of the stability. To understand the trends in the variation of E_{seg} with electronegativity of the different alloying elements (Zr, Hf, Nb, Mo, Al, Ga, Si, and Ge), we plotted E_{seg} as a function of $|\Delta EN|$, defined here as difference of electronegativity between alloying and Ti atom for both the d-block and p-block elements as shown in Figure 3.1 (d) and (e). We have considered Pauling electronegativity and the values taken from the CRC Handbook [62] are listed in Table 3.1 below. In case of p-block elements it is observed that as $|\Delta EN|$ decreases E_{seg} becomes more negative (Figure 3.1(e)) suggesting that the probability of the alloying element coming out of the bulk and segregating on the surface increases as the electronegativity difference between the host and the alloying element increases. This is in accordance with the empirical Hume-Rothery rules where it has been proposed that for a good alloy the electronegativity of the alloying elements should match. Similar trends are also observed in the d-block elements (Hf, Nb, and Mo) except for Zr (Figure 3.1(d)).

Table 3.1: Electronegativity values (EN) of different alloying elements

Dopant atom	**EN**
Ti	1.54
Zr	1.33
Hf	1.30
Nb	1.60
Mo	2.16
Al	1.61
Ga	1.81
Si	1.90
Ge	2.01

3.3.2 Oxygen molecule adsorption on pure and alloyed Ti(0001) surfaces

Before studying the adsorption and diffusion of oxygen atom on the pure and alloyed Ti(0001) surfaces, the interactions of the latter with an oxygen molecule was first studied. We started with configurations where an oxygen molecule is placed (both horizontally and vertically) at a height of 2 Å from the surface and relaxed the structure. On pure

Ti surface, irrespective of the starting configuration, the oxygen molecule dissociates and the dissociated O atoms occupies the hollow sites with an adsorption energy of -6.89 eV/O-atom. This is in accordance with previous reports [48, 51]. This result is similar to the dissociative adsorption of oxygen on other metal surfaces such as Al(111) and Pd(111) [63–66].

In presence of the alloying elements, when O_2 is placed horizontally or vertically on the surface, it undergoes dissociative adsorption with adsorption energies lying between -7.69 eV and -4.85 eV. The E_{ads} value for all the cases are listed in Table 3.2 below. However, Hf is an exception. For this case, when adsorbed vertically on Hf, O_2 binds in a molecular form with an adsorption energy of -2.78 eV and an O-O bond length of 1.31Å. Since the concentration of the alloying element is very small, so for Hf the probability of an oxygen molecule approaching the Hf atom vertically and binding in molecular form is very low. Hence in the remaining study we have considered that O adsorbs dissociatively on the surface.

Table 3.2: Oxygen molecule adsorption in the horizontal and vertical configuration

Dopant atom	**Horizontal**	**Vertical**
	near dopant atom near Ti atom	top of dopant atom top of Ti atom
Zr	-5.923 -5.943	-5.874 -6.267
Hf	-7.692 -5.757	-2.777 -6.600
Nb	-5.459 -5.755	-5.858 -6.726
Mo	-5.468 -5.523	-5.842 -6.727
Al	-4.846 -5.716	-5.726 -6.455
Ga	-5.855 -5.959	-5.732 -6.503
Si	-5.700 -5.801	-5.715 -6.364
Ge	-5.691 -5.729	-5.728 -6.463

3.3.3 Oxygen sorption on surfaces

Before studying the diffusion process, it is important to understand how atomic O adsorbs on these surfaces. Moreover, at higher O coverage there might be a competition between O being adsorbed on the surface and absorbed in the subsurface layer. Further, O absorbed in the subsurface layer is the final state of the surface to sub-surface diffusion. Hence, in this section we have presented results on study of adsorption and absorption of O at different coverages.

3.3.3.1 O adsorption at Θ_O = 0.06 ML

Pure Ti(0001) surface: Since the (4×4) surface unit cell has 16 Ti atoms, one O atom adsorbed on this surface amounts to 0.06 (1/16) ML coverage. This adsorbed O can occupy one of the following sites: (a) face centered hollow site (SFCC) (Figure 3.2(a)), (b) hexagonal closed pack hollow site (SHCP) (Figure 3.2(b)) and (c) bridge site between two Ti atoms. From our calculations we find that O does not adsorb on the bridge site and relaxes to either SFCC or SHCP. Amongst the hollow sites, O prefers to bind to SFCC with an adsorption energy of -5.80 eV. The average Ti-O and Ti-Ti bond length are 1.93 and 2.90 Å respectively. The configuration where O adsorbs at the SHCP site is about 0.30 eV higher in energy than SFCC site. We find our results to be in good agreement with literature reports. [52]

Alloyed Ti(0001) surface: For the alloyed surfaces, since the alloying element is on the surface, there are two types of SFCC and SHCP sites: (a) hollow sites formed by three surface Ti atoms, which we will call as SFCC1 and SHCP1 and (b) hollow sites formed by two surface Ti atoms and the alloying element that we will call as SFCC2 and SHCP2. These four sites are shown in Figure 3.2(c)-(f). Our calculations show that, oxygen being electronegative in nature, prefers to occupy the SFCC1 site in the presence of alloying elements, which are less electronegative than Ti (Nb, Mo, Al, Ga, Si, and Ge). The average Ti-O bond lengths when O is adsorbed on the alloyed Ti(0001) surfaces varies in the range 1.93-1.94 Å. In the presence of dopant atoms that are more electronegative than Ti (Hf and Zr) O prefers to adsorb on the SFCC2 site. For these cases the average Ti-O bond lengths ranges from 1.93-1.95 Å. In Table 3.3 we summarize the adsorption energy and the most stable adsorption sites for different Ti(0001) surfaces.

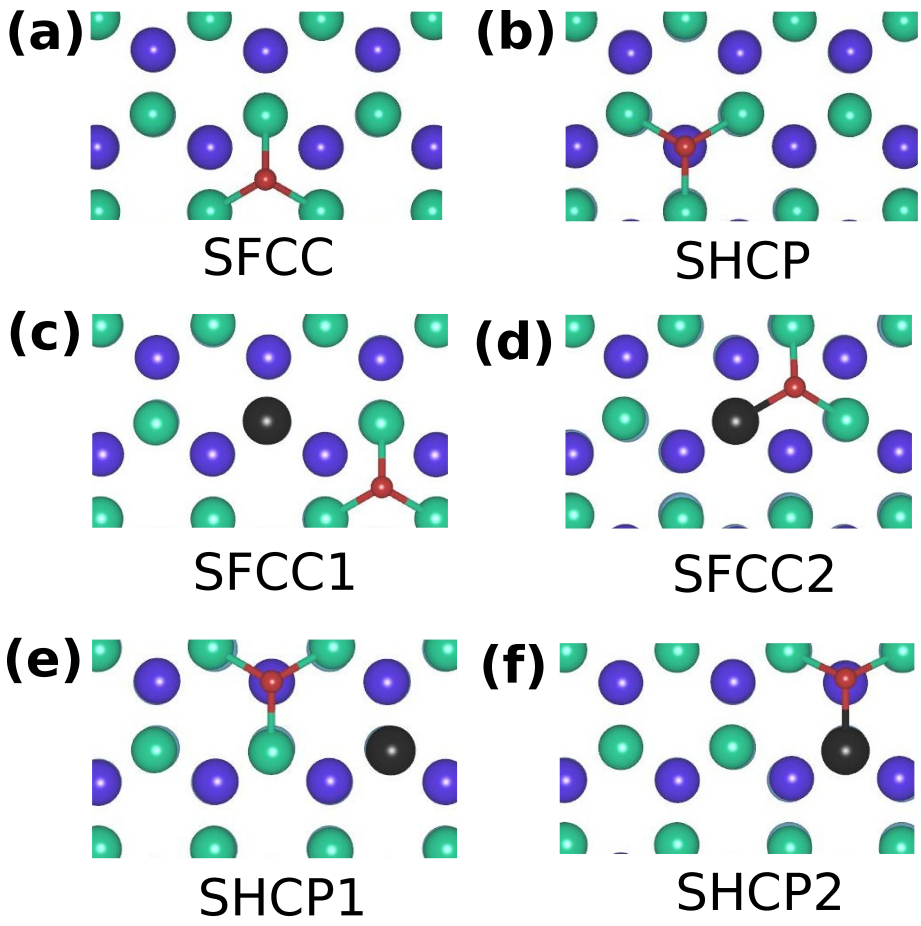


Figure 3.2: Oxygen atom surface adsorption sites; green, blue, black and red denote top Ti, Ti in second layer, alloying element, and oxygen atoms respectively.

3.3.3.2 Subsurface O absorption at Θ_O = 0.06 ML

If the oxygen atom penetrates and is absorbed into the subsurface Ti layer, for both the pure and alloyed Ti(0001) surfaces, they occupy either the octahedral or the tetrahedral interstitial sites. The subsurface octahedral site, hereafter called "Octa(m,n)", is below the SFCC site while the tetrahedral one (hereafter called "Tetra(m,n)") is below the SHCP site. "m" and "n" denote the layers between which this site exists. "m" ("n") denotes the layer above the site (layer below the site). For the alloyed surfaces there are two Octa and Tetra sites. The Octa (Tetra) site below SFCC1 (SHCP1) is called Octa1(m,n) (Tetra1(m,n)). Similarly, the Octa (Tetra) site below SFCC2 (SHCP2) is called Octa2(m,n) (Tetra2(m,n)). The different sites are shown in Figure 3.3. Our calculations show when the O atom is absorped at the first-subsurface layer, i.e., when m=1 and n=2, for the pure (alloyed) surface, the Octa(1,2) (Octa1(1,2)) is thermodynamically more favourable than

Table 3.3: Oxygen sorption energy (E_{ads}) on surface and sub-surface sites at 0.06 ML coverage.

Surface	**Adsorption Site**	E_{ads} **(eV)**
Pure-Ti	SFCC	-5.80
	Octa(1,2)	-4.87
	Tetra(1,2)	-4.67
Zr@Ti	SFCC2	-5.80
	Octa2(1,2)	-5.00
	Tetra2(1,2)	-4.75
Hf@Ti	SFCC2	-5.90
	Octa2(1,2)	-5.36
	Tetra2(1,2)	-5.10
Nb@Ti	SFCC1	-5.76
	Octa1(1,2)	-4.87
	Tetra1(1,2)	-4.77
Mo@Ti	SFCC1	-5.78
	Octa1(1,2)	-5.00
	Tetra1(1,2)	-4.70
Al@Ti	SFCC1	-5.76
	Octa1(1,2)	-4.91
	tetra1(1,2)	-4.70
Ga@Ti	SFCC1	-5.73
	Octa1(1,2)	-4.92
	tetra1(1,2)	-4.65
Si@Ti	SFCC1	-5.71
	Octa1(1,2)	-4.92
	tetra1(1,2)	-4.70
Ge@Ti	SFCC1	-5.68
	Octa1(1,2)	-4.90
	tetra1(1,2)	-4.60

the Tetra(1,2) (Tetra1(1,2)) (Table 3.3). This can be attributed to the smaller geometric volume of tetrahedral site compared to that of the octahedral site, which leads to large strain on the Ti lattice when oxygen atom occupies the tetrahedral site. Moreover, at this low O coverage, surface adsorption of O is more favourable than sub-surface absorption.

For both pure and alloyed Ti(0001) surfaces the octahedron/tetrahedron formed by the metal atoms surrounding the O atoms are slightly distorted. For the pure Ti(0001) surface the Ti-O bond length vary between 2.05-2.06 Å. In the case of Zr and Hf alloyed surfaces the Ti-O bond lengths in Octa2(1,2) and Tetra2(1,2) are between 2.04-2.05 Å, and the Hf/Zr-O bond lengths are about 2.16-2.20 Å. When the alloying elements are Nb, Mo, Al,

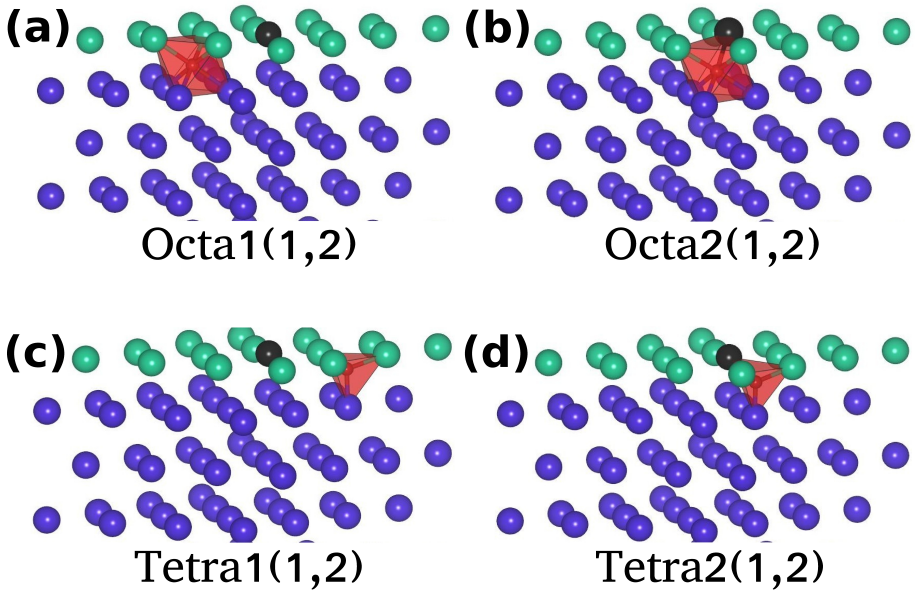


Figure 3.3: Oxygen atom subsurface absorption sites; green, blue, black and red spheres denote surface layer Ti atoms, Ti atoms in the remaining layers of the slab, alloying element, and oxygen atoms respectively.

Ga, Si, and Ge the Ti-O bond lengths in Octa1(1,2) and Tetra1(1,2) configurations varies between 2.05-2.06 Å. The alloying metal-O bond lengths are around 3.50-3.55 Å. Both the Ti-O and the alloying metal-O bond lengths are larger compared to the case when oxygen is adsorbed because of the presence of oxygen in between the subsurface layers.

3.3.3.3 Oxygen adsorption at higher oxygen coverage (Θ_O>0.06 ML)

Pure Ti(0001) surface: At higher oxygen coverages, the preadsorbed oxygen will have a significant effect on the upcoming oxygen. To study this, two oxygen atoms are placed in a (4×4) supercell which corresponds to Θ_O = 0.13 ML. There are 16 SFCC sites present (SFCC site being most stable adsorption site at Θ_O = 0.06 ML). Out of the two oxygen atoms, one is placed at the most stable SFCC site. The second oxygen can occupy any one of the remaining 15 SFCC sites. The distance between the two O atoms (d_{O-O}) can be used to distinguish different configurations and also to reduce the possible number of combinations to be considered for the two oxygen atoms to occupy. Based on d_{O-O}, we find that there are three inequivalent configurations, where the shortest distance between two O atoms are 3.12, 5.10 and 5.85 Å (Figure A.2 of the Appendix A). Our calculations show that the most stable configuration is the one where the two oxygen atoms are 5.10 Å away from each other (Figure A.3 in Appendix A) and binds to the surface with E_{ads} =

-5.85 eV/O atom. We note that the increased binding energy compared to that observed at 0.06 ML O coverage suggests that the interaction between the O molecules are attractive in nature. However, as shown in Figure A.3 of the Appendix A, if d_{O-O} is either smaller or greater than 5.10 Å, the oxygen binding becomes thermodynamically less stable. This suggests that if the O atoms come too close to each other ($d_{O-O} < 5.10$ Å), which might be the case at higher O coverages, the interaction between them will be repulsive in nature.

At Θ_O = 0.50 ML there are eight O atoms and 16 sites to occupy. To determine the possible symmetry inequivalent configurations, we adopted the following strategy. We begin by noting that if one O atom is at SFCC site, then there are 3 sites where the second incoming O can be adsorbed such that the d_{O-O} = 5.10 Å. Hence 4 O atoms will occupy 4 SFCC sites. The remaining 4 O atoms can occupy the remaining 12 sites. We considered all the symmetry inequivalent configurations for these cases and they are shown in Figure A.4 of Appendix A. In contrast, for the 1.00 ML O coverage, all the SFCC sites will be occupied. The black dotted line in Figure 3.4 shows the variation of O adsorption energy as a function of coverage. We observe that as Θ_O increases the O atoms come closer to each other resulting in repulsive lateral interaction between the O atoms, thereby reducing E_{ads}.

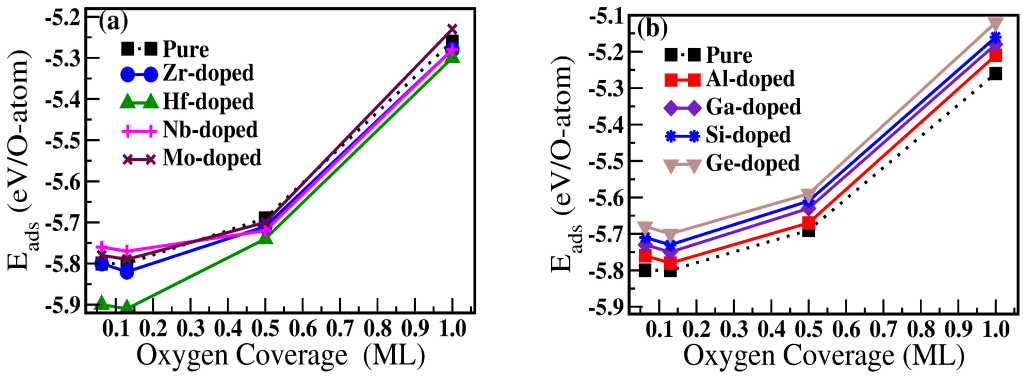


Figure 3.4: The calculated binding energies for oxygen atoms adsorbed on the surface at different oxygen coverage.

Alloyed Ti(0001) surfaces: As shown in Section 3.3.3.1, for the surfaces containing alloying elements there are four types of sites, viz., SFCC1, SFCC2, SHCP1 and SHCP2. For Θ_O = 0.13 ML, i.e., two O atoms on the surface, we have considered different configurations where these O atoms occupy two of the above mentioned four sites. Additionally, for a given combination of sites we have varied the distance between the O atoms also. E_{ads} as a function of d_{O-O} for each combination of adsorption sites when alloyed with

d (p-block) elements are shown in Figure A.5 (Figure A.7) of Appendix A. Amongst the d-block elements, when the alloying elements are Hf and Zr, we find that for all values of d_{O-O} the configurations where the O atoms occupy a combination of SFCC1 and SFCC2 sites are lowest in energy. In contrast, on alloying with Nb and Mo, we find that, irrespective of the separation of the two O atoms, the configurations where both the O atoms occupy the SFCC1 site are lowest in energy. This behaviour can be attributed to the difference in electronegativity between the alloying element and Ti. Nb/Mo being more electronegative than Ti, the O atom prefers to adsorb on the SFCC1 sites formed by 3 Ti atoms. For Zr and Hf, which are less electronegative than Ti, O prefers to bind to SFCC2 site formed by two Ti and one Zr/Hf atom. However, on the surface there are only 3 SFCC2 sites and they are nearest neighbours to each other. Hence, when the two O atoms occupy two SFCC2 sites, the distance between them is close enough, resulting in a repulsive interaction between them. Therefore, a combination of two SFCC2 sites is not favourable. Rather, one of the O atoms prefer to bind to a SFCC1 site and the second O binds to SFCC2 site. Moreover, we find that for these sites, the d_{O-O} at which the O adsorption configuration is most favourable are similar to that observed in case of Ti, with Zr being the exception. For the Zr alloyed surface the lowest energy configuration corresponds to $d_{O-O} = 5.09$ Å. Similar to Nb and Mo, the p-block elements being more electronegative than Ti, the two O atoms always prefer to occupy two SFCC1 sites, irrespective of the distance between the two sites (Figure A.7 of Appendix A). Additionally, for these, the optimal distance between the O atoms is about 5.8 Å, which is larger than those observed for pure Ti or when the d-block elements are used as alloying elements.

To determine the lowest energy configurations of O adsorption at Θ_O = 0.50 and 1.00 ML, we adopted a strategy similar to that described for the pure Ti(0001) surface. The different configurations considered in this study are shown in Figure A.6 and A.8 of the Appendix A. The O adsorption energies as a function of coverage in presence of p and d block elements are shown in Figure 3.4(a) and (b) respectively. We find that, similar to the case of pure Ti surface, in presence of alloying elements the O adsorption energy decreases as the O coverage increases. Moreover, for the p-block elements we observe that the O adsorption is weaker than that compared to pure Ti. Further, the reduction in O adsorption energy depends on the electronegativity difference between the alloying element and Ti; larger is the difference, weaker is the binding of O. For the d-block elements we observe similar trends in the behaviour of O adsorption with differences in electronegativity at low O coverages. However, for Nb and Mo we observe departure from this behaviour at

higher O coverages.

3.3.3.4 Adsorption versus absorption at Θ_O = 0.50 ML.

Based on our calculations described in the previous section, we found that as the O coverage increases, the O-O interaction become repulsive in nature. This indicates that at higher coverages absorption of O at the subsurface sites might become more favourable than adsorption on surface. Further, previous studies by Liu *et al.* [48] showed that for pure Ti, at 0.50 ML oxygen coverage, the configurations where oxygen atoms occupying a combination of surface and sub-surface sites are more favourable than all the O atoms occupying surface sites. They also observed that amongst these configurations, the ones in which the O atoms occupy alternate layers are more favourable than the ones in which they occupy adjacent layers. In this section we will investigate what happens in presence of alloying elements.

The different configurations used to determine the most stable adsorption and absorption geometries are shown in Figure 3.5(a) and (b). In each case, the total number of oxygen atoms is fixed at 8. This corresponds to 0.50 ML surface coverage. Starting from the most stable adsorption configuration of 0.5 ML O adsorbed on the surface, we removed one atom from the surface and placed it in the sub-surface layer. This corresponds to a coverage of 0.06 ML in the sub-surface layer and 0.44 ML on the surface. The adsorption energies for the different configurations considered for all alloying elements are shown in Figure 3.5(c) and (d). For the d-block elements (Zr, Hf, Nb, and Mo) the configuration in which all the O atoms are adsorbed on the surface sites is more favourable than the ones where oxygen atoms occupy a combination of surface and sub-surface sites. This suggests that oxygen penetration from surface to sub-surface site endergonic. Moreover, we also observe that amongst the mixed configurations, the ones where the subsurface O occupies the Octa(2,3) sites are more favourable than the ones where the O atoms occupy the Octa(1,2) sites, which implies that the diffusion from the first subsurface to the second subsurface layer is exergonic. For the p-block elements (Al, Ga, Si, and Ge), amongst the mixed configurations, the ones where the subsurface O occupies the Octa(2,3) site is lower in energy than the case when all the O atoms are on the surface. This suggests that similar to pure Ti, for p block alloying elements, at 0.5 ML O-coverage, the subsurface sites start becoming thermodynamically more favourable.

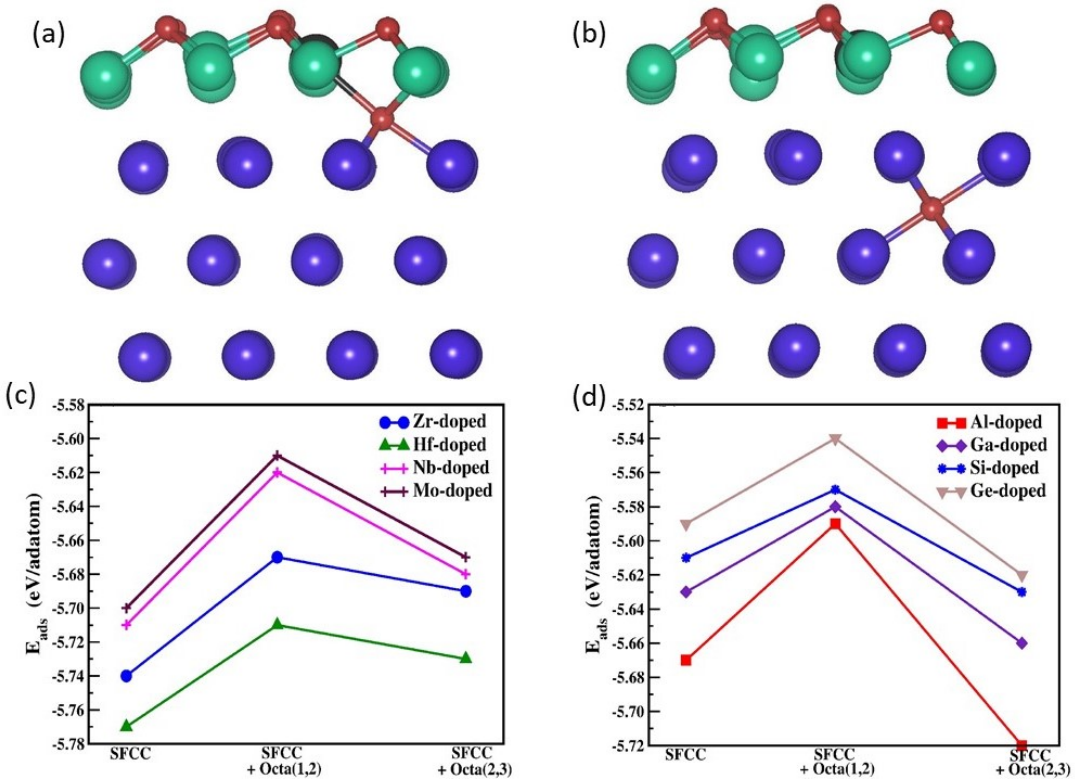


Figure 3.5: Multiple-layer adsorption model showing adsorption sites (a) SFCC+Octa(1,2) and (b) SFCC+Octa(2,3). The adsorption energy for different configurations considered. (c) and (d) represents the d and p-block elements. In (a) and (b) green, blue, black and red spheres denote surface layer Ti atoms, Ti atoms in the remaining layers of the slab, alloying element, and oxygen atoms respectively.

3.3.3.5 Thermodynamic analysis

In order to understand the relative stability of the surfaces at different O coverage as a function of the O partial pressure and temperature, we have computed the Gibbs free energy using ab initio thermodynamic analysis. The details of the calculations are given in Section A.1.3 of the Appendix A. From the plots of free energy as a function of temperature and O partial pressure (Figures A.9 - A.17), we have computed the pressure-temperature phase diagram, the plot of which is shown in Figure 3.6. The top (bottom) panel of Figure 3.6 shows the effect of alloying Ti with d-block (p-block) elements on the equilibrium pressure and temperature of transitions from clean to 0.06 ML to 0.5 ML to 1.0 ML O covered surface. When alloyed with d-block elements, we observe that at a given temperature, the O partial pressure for transition from clean to 0.06 ML O covered surface decreases in the presence of the alloying element (Figure 3.6(a)), with Mo show-

ing the largest decrease. In contrast, when alloyed with the p-block elements, we do not observe significant changes (Figure 3.6(d)). Further, we observe that the transition from 0.06 ML O-covered surface to 0.5 ML O covered surface is not significantly affected by the alloying element (Figure 3.6(b) and (e)). Both the d and p-block alloying elements enhance the O partial pressure required for the transition from 0.5 ML to 1.0 ML O covered surface at a given temperature. However, the effect is stronger for p-block elements (Figure 3.6(f)) than that observed for d-block elements (Figure 3.6(c)). Moreover, we also observe that the increase in the O partial is more if ΔEN is more.

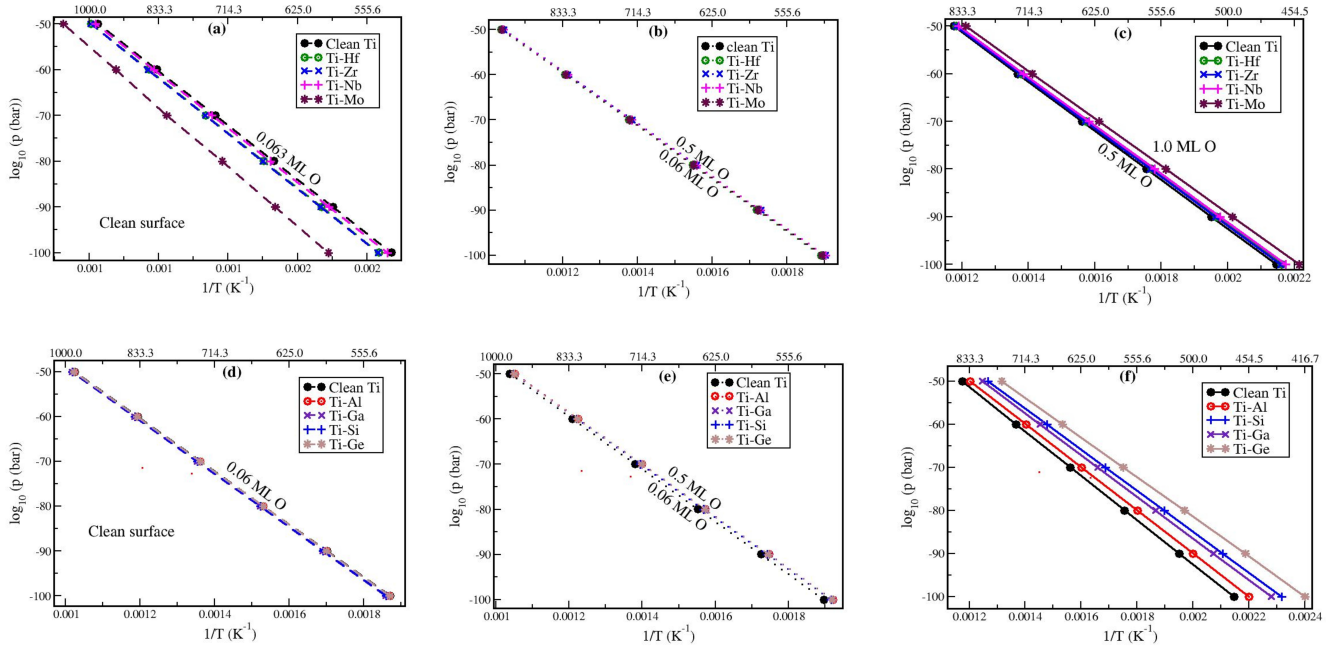


Figure 3.6: Temperature-pressure phase diagrams for O on pure and alloyed Ti(0001) surface showing the transitions from (i) clean to 0.06 ML O coverage ((a) and (d)), (ii) 0.06 ML to 0.5 ML O coverage and (iii) 0.5 ML to 1.0 ML O coverage. The top (bottom) panel shows the effect of alloying Ti with d-block (p-block) elements.

Based on literature report, before TiO_2 is formed, there is formation of an α-case (TiO) where the Ti atoms are in +2 oxidation state and the Ti:O ratio is 1:1. We note that at 1.0 ML O coverage the Ti:O ratio is 1:1 and is analogous to the formation of the first layer of α-case. This is further corroborated by the fact that all the surface metal atoms have Bader charges greater than +1 (discussed in Section A.1.3 and Figures A.18 - A.26 of Appendix A). In order to understand the onset of the oxidation, we have computed and compared the charges on the surface metal atoms at 0.06 and 0.5 ML O coverage (Figures

A.18 - A.26 of Appendix A). While for 0.06 ML O coverage, there are very few positively charged metal atoms, when the O coverage is increased to 0.5 ML, we observe that a significant fraction of the surface atoms become positively charged. Hence, 0.5 ML O coverage can be considered the onset of surface oxidation. Based on the results described in the previous paragraph, we note that the alloying element does not significantly affect the O partial pressure required for the onset of surface oxidation. Interestingly, at a given temperature, the presence of the alloying element enhances the O-partial pressure required for stabilizing the first layer of the α-case.

3.3.4 Coverage dependent diffusion of oxygen from surface to sub-surface

During the early stage of oxidation, the O atoms adsorbed on the surface will penetrate the surface Ti layer and start moving to the subsurface sites. The rate at which the oxidation will proceed depends on the rate at which the O atoms diffuse into the subsurface. The kinetics of the later, however, depends on the diffusion barrier. Hence to understand the effect of the alloying elements on the initial oxidation process it is important to understand their effect on the diffusion barrier. Therefore, in this section we have studied the barriers for diffusion of a single O atom from surface to sub-surface for pure and alloyed Ti(0001) as a function of O coverage. For all the cases, at a given O coverage, the initial state corresponds to the most stable configuration at that particular coverage (as described in the previous sections). For the final state we restricted ourselves to the cases where the O atom penetrates vertically and occupies the sub-surface site.

At Θ_O = 0.06 ML, for all the cases it is the octahedral site in between the surface and first subsurface layer right below the surface FCC site. At 0.50 and 1.00 ML coverages, on Ti(0001) surface the final state is one in which one O atom occupies Octa(1,2) site while the others occupy SFCC sites. For the alloys, the Octa(1,2) sites are classified in two categories: Octa1(1,2) and Octa2(1,2). Here also at both 0.50 and 1.00 ML coverages we tried different configurations in which one of the surface O atoms occupy either one of the octahedral sites. For Zr and Hf the subsurface O prefers to occupy Octa2(1,2) while for Nb, Mo and the p-block elements the subsurface O occupies Octa1(1,2) sites. The diffusion pathway along with the initial, transition and final states for each case is shown in Figure A.27, A.28 and A.29 of the Appendix A. The barriers at different O coverage for all the systems are summarized in Table 3.4 below.

Figure 3.7(a) and (b) show the variation of the diffusion barrier with ΔEN at different

Table 3.4: Surface to subsurface diffusion barriers of O (in eV) at different oxygen coverage.

Surface	E_{act} at 0.06 ML	E_{act} at 0.50 ML	E_{act} at 1.00 ML
Ti(0001)	1.97	1.65	0.81
Zr@Ti(0001)	1.96	2.10	1.10
Hf@Ti(0001)	2.01	2.19	1.10
Nb@Ti(0001)	1.81	1.73	1.00
Mo@Ti(0001)	1.88	1.68	0.84
Al@Ti(0001)	1.72	1.65	0.72
Ga@Ti(0001)	1.65	1.60	0.69
Si@Ti(0001)	1.62	1.55	0.62
Ge@Ti(0001)	1.60	1.46	0.61

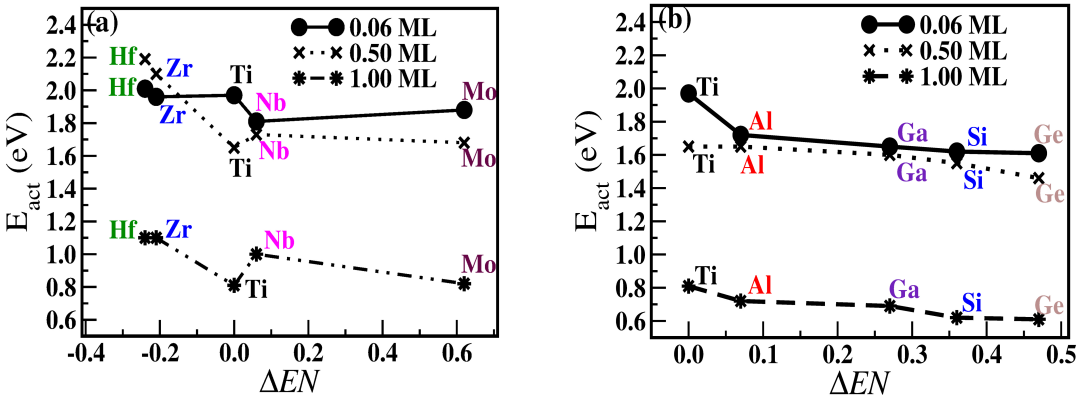


Figure 3.7: Diffusion barrier as a function of ΔEN at different oxygen coverage.

O coverage in presence of d and p-block alloying elements, respectively. For the d-block elements we observe that as Θ_O increases the barrier decreases, except for Zr and Hf at 0.50 ML coverage (Figure 3.7(a)). The larger barrier at smaller O coverage can be understood from the fact that for this the diffusion process is endergonic. Further, at 0.06 ML coverage E_{act} decreases as ΔEN increases. The lowering in the barrier as a function of ΔEN is due to the stronger (weaker) binding of the surface O atom in presence of the alloying elements that are less (more) electronegative than Ti.

At Θ_O = 0.50 and 1.00 ML, though E_{act} vs. ΔEN follows similar trends as that observed at 0.06 ML coverage, E_{act} in presence of alloying elements is larger than that of Ti for all the elements irrespective of the value of ΔEN. In order to understand the deviations discussed above, we computed the reaction energy (E_{rxn}) that is defined as the difference in total energy between the case where an O atom is occupying a subsurface site and when all the O atoms are on the surface (initial state). Figure 3.8(a) and (c) show

the plots of E_{rxn} as a function of the position of the diffusing O atom at Θ_O = 0.50 and 1.00 ML. We find that for all the alloying elements, E_{rxn} is larger than that observed for pure Ti(0001) surface. Further, the plot also shows that the diffusion process is endergonic at 0.50 ML O coverage and exergonic when the O coverage is increased to 1.00 ML.

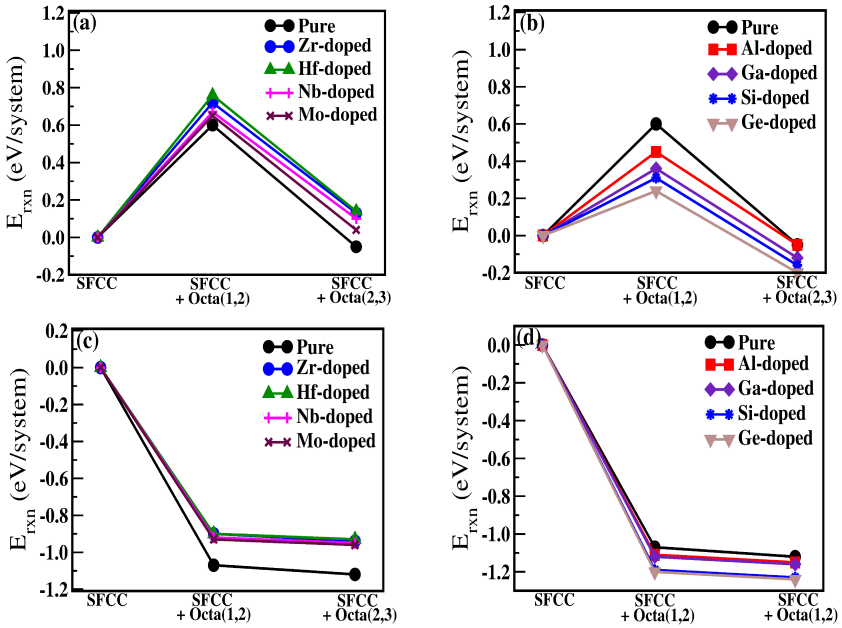


Figure 3.8: The calculated reaction energy (a), (b) at 0.50 ML and (c), (d) at 1.00 ML oxygen coverage.

When the p-block elements are used as alloying elements, we observe that the diffusion barrier reduces when the O coverage increases (Figure 3.7(b)). Further, irrespective of the O coverage, the O diffusion barrier decreases as alloying elements become more electronegative than Ti. This can be understood from the trends of E_{rxn} as a function of the position of the diffusing O atom. As shown in Figure 3.8(b) we observe that upon doping at 0.50 ML O coverage the diffusion process is not only less endergonic compared to that of pure Ti but also becomes exergonic at $\Theta_O = 1.00$ ML (Figure 3.8(d)), suggesting a stronger driving force for the diffusion process. Thus our results suggests that doping Ti with a more electropositive element will be more effective to hinder the early oxidation.

In order to understand how the sign and the magnitude of the electronegativity difference between the Ti atom and that of the alloying elements affects the property of the Ti surface, thereby influencing the diffusion barriers, we have plotted E_{act} as a function of E_{ads} (Figure 3.9(a)). We find that the diffusion barrier is inversely related to the adsorption energy of the O atom on the surface. By fitting the data to a linear equa-

tion we obtained the Brønsted-Evans-Polanyi (BEP) relation between the two quantities ($E_{act} = -9.205 - 1.918E_{ads}$ eV). From further analysis we find that the changes in the adsorption energies are related to the charge on the Ti atoms that are interacting with the incoming O atoms and are near the alloying element. From the plot of E_{ads} as a function of Bader charge on this Ti atom (Figure 3.9(b)) we observe that, barring a few exceptions, for most cases the adsorption energy decreases when the charge become more positive. Further, we also find that the sign and the magnitude of the charge depends on the sign and magnitude of the difference in electronegativity between the Ti atom and the alloying element. For those cases where the alloying element is more electronegative than Ti, i.e. negative ΔEN, the magnitude of the negative (positive) charge on the Ti atom decreases (increases), as observed for p-block (d-block) elements, when $|\Delta EN|$ increases (Figure 3.9(c))). In contrast, for the two electropositive elements considered here the charge remains similar. Therefore, our overall analysis suggests that for negative ΔEN (electronegative elements) the charge on the Ti atoms becomes less negative and for some cases also becomes positive. This weakens the E_{ads} thereby lowering the diffusion barrier. In contrast for positive ΔEN we observe that the alloying element transfers charge to the nearby Ti atom which favours stronger binding of the O atom to the surface, thereby reducing the barrier. Our analysis suggests that electropositive elements will be better candidates for hindering the oxidation of Ti surface.

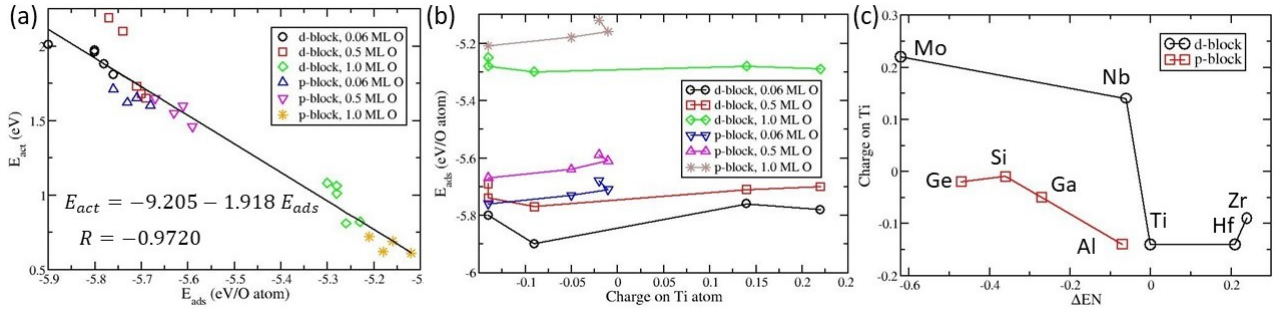


Figure 3.9: (a) Plot and BEP relation between barrier of diffusion of atomic O from surface to sub-surface. (b) Plot of variation of adsorption energy of O adsorbed on the surface with charge on the Ti atom next to the alloying element and interacting with the O atom. (c) Charge on the Ti atom next to the alloying element and interacting with the O atom as a function of ΔEN.

At this point, it would be interesting to compare our results with experimental results. However, to the best of our knowledge, there are no data available for the early stages of oxidation. Hence, we have compared our results with the rate of mass gain measured by Kitashima *et al.* [46] In their experiments the mass gain is due to the formation of the

oxide layers on Ti and smaller the rate, more hindered is the oxidation process. According to their results, the mass gain rate increases in the following order: Hf $<$ Zr $<$ Si $<$ Nb $<$ Mo $<$ Al $<$ Ga $<$ Ge. Amongst these the rate of mass gain is more than Ti when Al, Ga and Ge are the alloying elements. Since in these experiments the oxide layers have already formed, while in this work we are studying the early stages of oxide formation, it would be apt to compare our results for the 1.0 ML O coverage with the experimental one because at these coverage we have 1:1 Ti and O ratio that is analogous to the α-case reported in literature. A comparison of our results reported in Figure 3.7 with the experimental ones shows that, in accordance with experiments, alloying Ti with the d-block elements not only increase the O diffusion barrier compared to that observed in Ti, but also the order in which it is increased is same as that observed in the experiment. For the p elements, our computed barriers decrease on doping in the following order Ge $<$ Si $<$ Ga $<$ Al $<$ Ti. Again, for these p-block elements the trends observed from our calculation are same as that observed in the calculations, except for the case of Si. In this case while we predict that Si will reduce the barrier compared to pure Ti, in experiments it is observed that Si hinder the growth of the oxide layer.

3.4 Conclusions

In summary, in an effort to understand the effect of alloying on Ti oxidation (at the initial oxidation stage) and identify descriptors connected to the property of alloying element that correlate with its effectiveness to hinder initial oxidation of Ti, we have studied O adsorption and surface to subsurface diffusion in pure and alloyed α-Ti(0001) surfaces. We considered d-block (Zr, Hf, Nb, and Mo) and p-block (Al, Ga, Si, and Ge) elements for our purpose. We found that all these elements prefer to segregate on surface layers. As a function of O coverage, we observe that for pure and p-block element alloyed Ti surface O prefers to occupy the sub-surface sites at an O coverage of 0.50 ML. When the O coverage is increased further to 1.00 ML, for all surfaces, O starts filling up the sub-surface sites. From our calculations of diffusion barrier at different oxygen coverages, we observe that the difference in electronegativity between Ti and the alloying elements correlate with the diffusion barrier. The difference in electronegativity affects the charge on the Ti atoms thereby influencing the adsorption energy of O on the surface and the surface to subsurface diffusion barrier. The trends in the barrier observed from our calculations are in reasonably good agreement with experimental reports on rate of growth of oxide layer. Moreover our

results also suggest that more electropositive is the alloying element compared to that of Ti, larger will be the O diffusion barrier, thereby indicating that such alloying material will hinder Ti oxidation more efficiently.

Chapter 4

Influence of Hydrogen Sulphide on the surface properties and hydrogen permeability through PdCu membrane

Palladium based alloys are commonly used in industry as a membrane material for the purification of hydrogen, because of their high hydrogen permeability and catalytic activity concerning hydrogen dissociation. However, they are susceptible to poisoning, induced by impurities in the gasifier effluent streams like H_2S, in the form of corrosion or catalyst deactivation. In this work, we report a systematic theoretical study of the dissociation process of H_2S, and its influence on the H_2 dissociation. Moreover, the effect of its derivative (sulphur) on the hydrogen adsorption, dissociation and hydrogen penetration via the solution diffusion mechanism through a model PdCu(110) membrane, as a function of the sulphur coverage have also been studied. We find the dissociation of H_2S is a facile process. Additionally, we observe slight lowering of H_2 dissociation barrier in the presence of H_2S as compared to that observed on the clean PdCu(110) membrane. Our calculations also suggest that there is a significant decrease in the hydrogen adsorption energy in the vicinity of the sulphur adatoms. Irrespective of the hydrogen coverage, blocking of hydrogen adsorption happens only for higher sulphur coverages. Based on the microkinetic model of the permeation process, we find the permeation in the presence of sulphur can be limited by both reassociation of atomic H atoms and dissociation of H_2 molecule depending significantly on the hydrogen, sulphur coverage and temperature.

4.1 Introduction

Hydrogen is considered as one of the cleanest energy sources and environmentally sustainable energy carrier. Large scale use of hydrogen energy is an effective way to solve the greenhouse effect caused by burning of fossil fuels since its combustion does not re-

lease carbon dioxide [67, 68]. It is also used as a transportation fuel for reducing motor vehicles emission, aerospace and other fields. The so-called "Hydrogen economy" will provide power generation causing an increased demand of hydrogen in the upcoming years [16, 17]. With the development of world economy, efficient hydrogen production and separation technology is required to provide solutions for global energy crisis and air pollution.

Till date one of the primary source of H_2 is hydrogen rich syngas ($CO+H_2$) that is produced on a large scale by "steam-methanol reforming" (SMR) and "water-gas shift reaction". One of the most critical steps in production is purification and separation of pure hydrogen from gas stream which contains contaminants like H_2S, produced as by-products of the reaction or from the atmosphere.

Membranes are promising candidates that are currently being employed as a low cost and efficient solution for hydrogen purification [69–71]. Based on composition, they are classified as metallic (dense and porous), inorganic (oxides, zeolites), carbon and polymeric. The performance of a membrane could be measured in terms of its permeability, selectivity, and thermal stability. Among the above-mentioned membranes, the dense metallic ones are preferred because of their higher strength, higher hydrogen selectivity and ability to produce high purity hydrogen through solution-diffusion mechanism. Metals like Pd, Pt, Ni can transport dissociated hydrogen atoms through diffusion across a dense layer of metal [72]. Palladium and its alloys have been the most studied membranes for separation of hydrogen due to their more favourable properties like high permeability and high catalytic activity when compared to the other elements [73–76]. Pure palladium, however, is susceptible to phase transition below 300°C, consequently resulting in volume expansion which causes distortion of its crystalline structure and mechanical failure of the membrane [77–79]. Further, they are also liable to "poisoning" induced by presence of other gases like H_2S which adversely affects the performance and stability of these membranes. Alloying Palladium with other metals alleviates the above problems to some extent. However, still much need to be done to understand and address the above problems. Addition of elements like Cu to Pd offers a cost-effective solution to hydrogen embrittlement and enhances sulphur tolerance [80]. The desired composition of the alloy could be attained by varying the concentration of Cu.

Hydrogen permeation through a membrane via solution diffusion mechanism consists of the following steps: (1) Adsorption of raw gas (H_2 and unwanted (H_2S) gas) at the feeder side of the membrane surface, (2) dissociation of H_2 and H_2S on the membrane

surface, (3) penetration of H from surface subsurface, (4) diffusion of atomic H within the bulk of the membrane to the permeate side, (5) diffusion of H from subsurface to surface of the membrane on the permeate side, (6) reassociation of atomic H to molecular H_2 and (7) desorption of the molecular hydrogen from the permeate side. Amongst these, the impurities will affect steps (1), (2) and (3). In this work we study the effect of poisoning of the PdCu membrane by H_2S on the permeation. The membrane has been modelled by the (110) bcc phase of Pd-Cu alloy as it offers almost twice the hydrogen flux when compared to the fcc phase [81,82]. The rest of the Chapter is organized as follows: Section 4.2 gives the computational details. The results of our calculations are discussed in Section 4.3. Finally in Section 4.4 we conclude our results.

4.2 Methods

4.2.1 Computational Details

All the calculations were performed using the Quantum ESPRESSO software [55], which is a plane-wave based implementation of Density Functional Theory(DFT). The electron-ion interactions were described using ultrasoft pseudopotentials [56]. The electron-electron exchange and correlation potential was described using Perdew, Burke and Ernzerhof (PBE) functional of the generalized gradient approximation (GGA) [57]. Kinetic energy cutoff of 35 Ry and 350 Ry were used for the wave function and charge density, respectively. Brillouin zone integrations were performed with (9×9×9) Monkhorst-Pack k-point mesh for bulk PdCu. To speed up the convergence we have used Marzari-Vanderbilt smearing with smearing width of 0.005 Ry [59]. Our calculated lattice parameter for bcc structure of bulk PdCu is 3.02 Å, which is slightly over estimated with the reported experimental values [83,84], but are in good agreement with computed value of 3.03 Å [85].

We employed climbing image nudged elastic band (CI-NEB) [5,10,11] to map out the minimum energy path, energy barriers and transition states for the different processes (H_2 dissociation and H penetration). Depending on the length of the path 7-12 images were used. Forces on the images are converged up to 0.05 eVÅ^{-1}.

The rate constant (k_{hTST}) for a reaction step, computed using the harmonic transition-state theory, is given by

$$k_{hTST} = \frac{\prod_{i=1}^{3N} \upsilon_i^{init}}{\prod_{i=1}^{3N-1} \upsilon_i^{*}} exp(-\frac{\Delta E^q}{k_B T}) \tag{4.1}$$

where k_BT is the Boltzmann constant, T is the temperature, ΔE^q is the zero-point energy (ZPE) corrected barrier. ΔE^q is computed as

$$\Delta E^q = \Delta E^c + \frac{1}{2}(\sum_{i=1}^{3N} h\upsilon_i^* - \sum_{i=1}^{3N-1} h\upsilon_i^{init}) \tag{4.2}$$

where ΔE^c is the classical activation barrier obtained from CI-NEB calculations and υ_i^{init} and υ_i^* are the normal mode frequencies corresponding to the initial and transition state, respectively. The normal mode frequencies are computed using Density Functional Perturbation Theory(DFPT) as implemented in the Quantum Espresso software. [12]

The (110) surface was modelled using six-layer slab wherein, the bottom three layers were fixed at their bulk interplanar distances. To minimize the spurious interaction between the slab and its periodic images, a vacuum of 11 Å in the direction perpendicular to the surface was used. For the adsorption, dissociation, and penetration study of atomic hydrogen on this surface we have used a (3×2) surface supercell. The calculated adsorption energy given as:

$$E_{ads} = E_{surf+nX} - E_{surf} - yE_X \tag{4.3}$$

where $E_{surf+nX}$, E_{surf}, and E_X are the energies of the total system involving the surface and adsorbed species, only surface, adsorbed molecule X in the gas phase, respectively. If the adsorbed molecule X involves H, ZPE corrections were applied to the first and third terms in the right hand side of Eqn. 4.3.

4.3 Results and Discussion

4.3.1 H_2S dissociation

Since H_2S is a primary source for S poisoning of these surfaces, in this section we have studied H_2S dissociation on the clean surface. Further we have also studied how H_2S and H_2 dissociation are affected in the presence of each other.

4.3.1.1 Adsorption of H_2S and its derivatives on PdCu(110) surface

In H_2S dissociation, though the final products are atomic H and S, the reaction proceeds through the formation of sulfuhydrl (SH). Hence, in this section we report the results of our calculations to determine the most stable adsorption configuration of each of the

species on the surface.

On PdCu(110) surface there are three types of adsorption sites, namely, top (T), bridge (B) and three-fold hollow (H). The different sites are shown in Figure 4.1. We note that there are two top sites, T1 (atop Pd) and T2 (atop Cu). The bridge sites can be classified in three types: B1 (between two Pd atoms), B2 (between two Cu atoms) and B3 (between a Pd and a Cu atoms). Similarly, there are two types of hollow sites, H1 (between two Pd and one Cu atom) and H2 (between two Cu and one Pd atom). To determine the lowest energy configuration, for each of the species we have computed the adsorption energy on each of these sites.

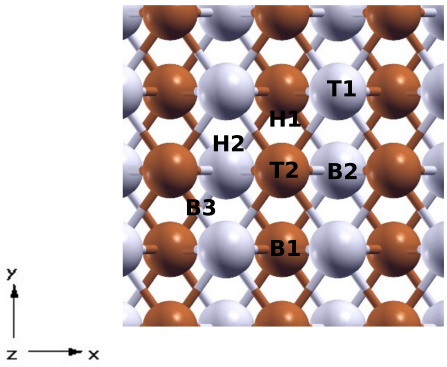


Figure 4.1: Top view of PdCu(110) surface. Different adsorption sites considered are marked. T, ontop adsorption; B, bridge site; H, hollow site. Pd and Cu atoms are represented in grey, brown color, respectively.

Adsorption of H_2S: Since the surface has six Pd/Cu atoms, the surface coverage of the adsorbed species has been defined as the number of adsorbed molecules of that species per number of Pd atoms on the surface. For example, one H_2S adsorbed molecule on this (3×2) surface supercell corresponds to a coverage of 0.16 ML. At this coverage, in the most stable adsorption geometry, the H_2S molecule binds on top of Pd (T1 site) through sulphur atom (Figure 4.2(a) and (b)) with a binding energy of -0.66 eV (-0.64 eV with ZPE correction). The plane of the molecule formed by two H and one S atom makes an angle of 91.2° with respect to the surface normal. The Pd-S bond length is about 2.38 Å. The H-S bond lengths are elongated by 0.01 Å compared to that of 1.35 Å in the gas phase. In contrast, the H-S-H bond angle is reduced to 91.2° from the gas phase value of 91.8°. We note that this configuration is very similar to the case of Pd(111) as was reported in literature. [86–88] The H_2S molecule placed on all the other sites end up in any one of the two top sites. The adsorption energetics on T2 site is described in Table B.1 of Appendix B of the .

Adsorption of SH: Similar to that on Pd(111) surface, [86] SH on PdCu(110) prefers to adsorb on the B2 site (Figure 4.2(c) and (d)) with an adsorption energy of -3.16 eV (-3.11 eV with ZPE corrections) with respect to the gas phase SH. The S atoms not only binds to the two bridge Cu atoms (Cu-S bond length of 2.26 Å) but also to the Pd atoms that are at right angle to the B2 site, the Pd-S bond length being 2.61 Å. Due to the strong interaction with the surface, the SH bond is slightly elongated (0.01 Å) with respect to those of the H_2S molecule on the surface. The details of the other configurations are given in Table B.2 of Appendix B.

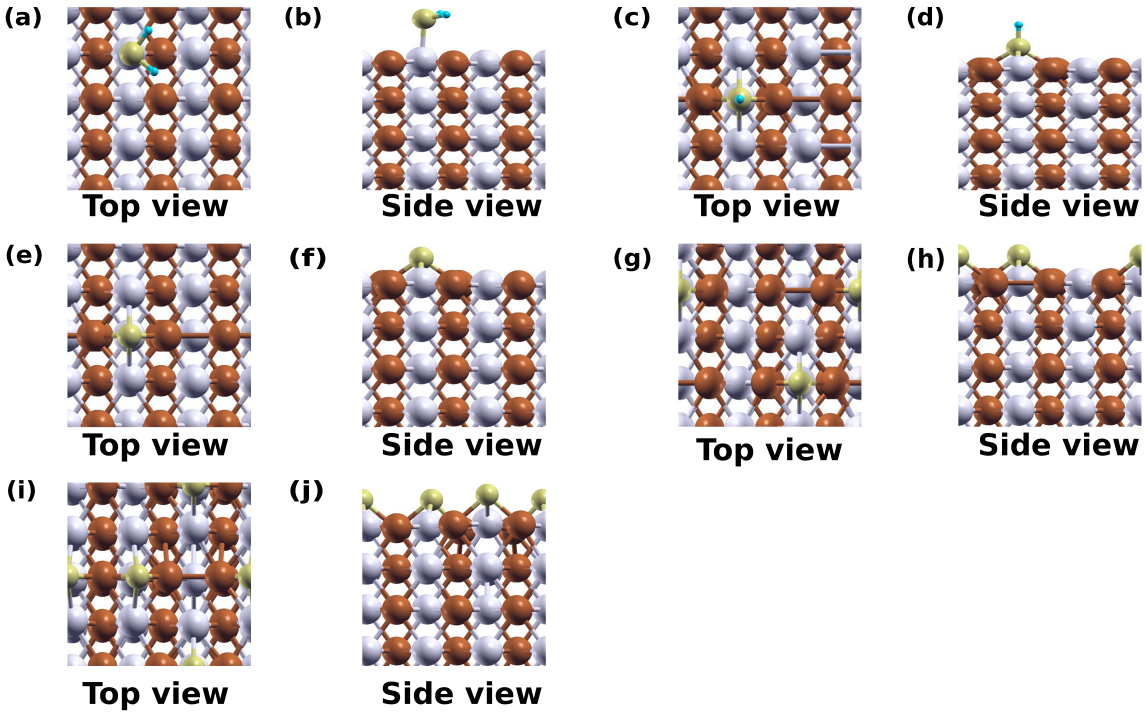


Figure 4.2: Top and side view of most stable structures of H_2S, SH, and S (0.16 , 0.33 and 0.50 ML).

Adsorption of S: At 0.16 ML coverage the most stable configuration of sulphur on PdCu(110) corresponds to the adsorption on the B2 bridge site with a binding energy of -2.53 eV, which is in agreement with literature report. [89, 90] The top and side view of the same is shown in Figure 4.2(e) and (f). The Pd-S and Cu-S bond lengths are 2.41 and 2.21 Å respectively. The details of the other configurations are given in Table B.3 of Appendix B.

Since we are interested in the effect of hydrogen adsorption and dissociation in presence of various S coverage, here we also report the adsorption of S at coverages $\Theta_S = 0.33$,

0.50 and 1.00 ML. On the (110) surface there are six distinct B2 sites available for sulphur adsorption. The second S can occupy any one of the remaining five B2 sites. The distance between two sulphur atoms (d_{S-S}) was used as the criteria to distinguish the different configurations. Based on d_{S-S}, we find that there are three inequivalent configurations, where the shortest distance between two S atoms are 3.50, 4.28 and 5.24 Å as shown in Figure B.1 of Appendix B. Our calculations show that the most stable configuration is the one where the two S atoms are 5.24 Å away from each other and binds with E_{ads} of -2.55 eV/S atom as shown in Figure B.2 of Appendix B. The top and side view of the same is shown in Figure 4.2(g) and (h). The rest inequivalent configurations are shown in Figure B.1 of Appendix B. For Θ_S = 0.50 ML, three sulphur atoms are placed at different B2 sites such that the $d_{S-S} \approx$ 4.50 Å. The top and side view of the most stable configuration are shown in Figure 4.2(i) and (j). The different possible configurations are shown in Figure B.3 of Appendix B. In the lowest energy configuration, S adsorption energy is -2.12 eV/S atom. At 1.00 ML S coverage all the six B2 sites are occupied by sulphur. The adsorption energy varies from 2.55 to -1.75 eV/S atom.

4.3.1.2 H_2S dissociation

To study the dissociation of H_2S molecule on PdCu(110) surface we have considered the following reaction steps:

R1: $H_2S^* \rightarrow SH^* + H^*$

R2: $SH^* + H^* \rightarrow S^* + 2H^*$

where '*' indicates that the species is adsorbed on the surface.

R1: $H_2S^* \rightarrow SH^* + H^*$. The first S-H bond cleavage of H_2S on this surface to form sulfuhydrl (SH^*) and H^* is exothermic by about -0.74 eV. As shown in the previous section, while the initial state (IS) corresponds to H_2S adsorbed atop Pd, in the final state (FS) SH and H are adsorbed on B2 and H1 site respectively, that share the Pd atom to which H_2S is adsorbed. In the transition state (TS) the molecule is asymmetrically tilted towards the B3 site with Pd-S and Cu-S bond lengths of 2.76 and 2.51 Å respectively. In this configuration, the plane of the molecule is tilted towards the surface and the dissociating H-S bond is elongated to 1.43 Å compared to that of 1.36 Å in the IS. The other S-H bond length do not show any change. Following this the S-H bond cleaves and the dissociated species diffuse to their lowest energy configuration. This process involves a barrier of 0.27 eV (0.24 eV with ZPE correction). We note that while this barrier is equal to that observed on Ni(111) surface, [87] it is much smaller than that of 0.33 eV on Pd(111) surface [87].

R2: $SH^* + H^* \rightarrow S^* + 2H^*$. In the FS of the second SH dissociation the two H atoms occupy the H1 site while the S atom occupy the B2 site, as shown in Figure 4.3 compared to the IS the reaction is exothermic by about -0.82 eV. The reaction proceeds through an intermediate state in which the SH species is tilted towards the Pd atom and the SH bond becomes parallel to the surface. This process is almost barrier less with a barrier of 0.01 eV. In this metastable state the S-H bond length is elongated to 1.41 Å from that of 1.37 Å in the IS. In the TS, the S-H bond cleaves with S atom occupying the B2 site and the H atom is bound to the Pd atom. The S-H distance is about 1.87 Å. Following this, the H diffuses to the most stable H1 site in the FS. The activation barrier for this bond cleavage is 0.08 eV (0.06 eV with ZPE correction).

Combining these two pathways we observe that the cleavage of the first SH bond is the rate limiting step in the dissociation of H_2S on PdCu(110). The H_2S dissociation energy profile for reaction steps R1 and R2 are shown in Figure B.4 of Appendix B. Similar sequential dissociation of S-H bonds are also observed on (111) surfaces of Ni, Pd and NiPd [87, 88]. Akin to PdCu(110) surface, on these surfaces also the breaking of first SH bond is the rate determining step for the overall H_2S decomposition reaction. While the barrier on Ni(111) surface is similar to that we observe on PdCu(110), those on Pd(111) and PdNi(111) are higher.

4.3.2 Coadsorbed H_2 and H_2S dissociation

At the feeder side of the membrane, the gas will contain both H_2 and H_2S. Hence when they come in contact with the membrane surface both will adsorb on the surface and the dissociation of one might be affected due to the presence of the other. Hence, in this section we will study how the coadsorption of H_2 and H_2S affects their dissociation.

4.3.2.1 H_2 and H_2S coadsorption

As shown in the previous section and in Ref. [7] H_2S binds more strongly on the surface than H_2, -0.66 eV versus -0.35 eV. Hence, when both the molecules simultaneously approach the surface, the probability of H_2S binding is higher than H_2. Therefore, in order to study the coadsorption of H_2 and H_2S on the PdCu(110) membrane surface we start with H_2S bound to a T1 site. Since, for both the gas molecules the top sites are favourable, we have restricted to configurations where the molecules are bound to the top site. Based on the above two considerations, we considered configurations in which H_2S is on T1 site and H_2 is either on T1 or on a T2. Additionally, we also consider cases where both the

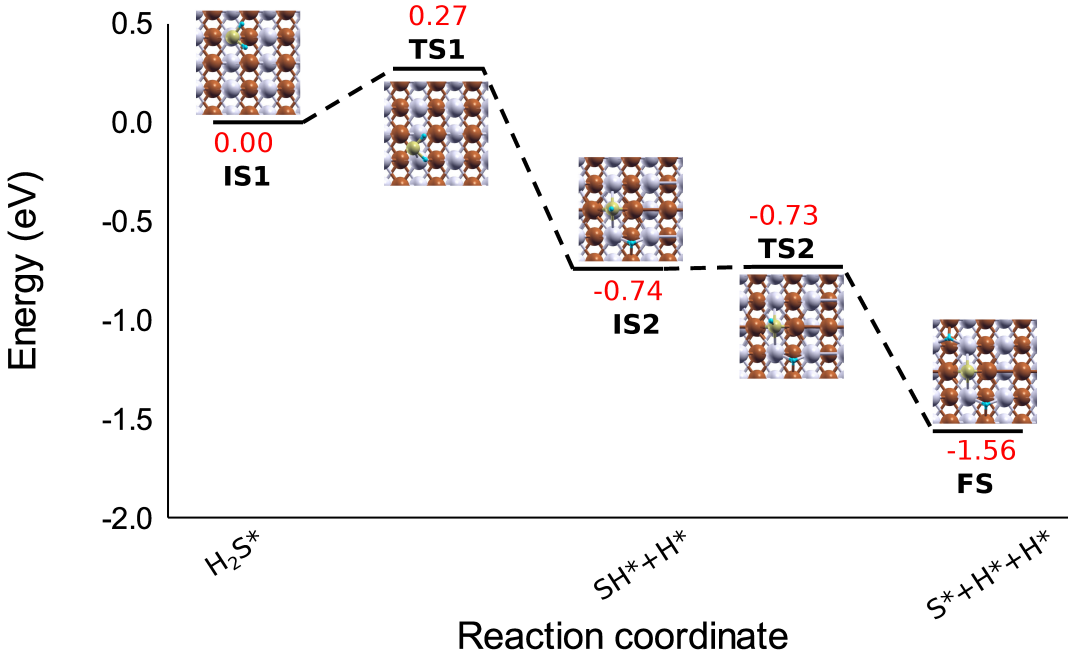


Figure 4.3: The energetics and geometries of the initial states(IS), Transition states(TS), and final state(FS) for the H_2S dissociation reaction. The numbers in red are the reaction energies calculated with respect to H_2S on the surface.

molecules occupy T2 sites. Further, when the molecules are placed on bridge or hollow sites, or a combination of both, the structure relaxes to either T1 or T2 or a combination of T1 and T2. The relaxed geometries of all the considered configurations are shown in Figure B.5 of Appendix B.

We find that in the lowest energy configuration both H_2 and H_2S coadsorb on the T1 sites that are separated by about 4.28 Å along the y direction (Figure 4.4). In this configuration the coadsorption energy is -0.97 eV (-0.94 eV with ZPE), which is about 0.04 eV higher in energy than the sum of the individual adsorption energies of H_2S and H_2 (non interacting limit), suggesting that in this coadsorbed configuration the interaction between the two molecules are weakly repulsive in nature. Moreover, in accordance with the picture obtained from the energy considerations, we note that the orientation and the bond lengths of the molecules in this configuration are same as those observed when they are interacting individually with the surface.

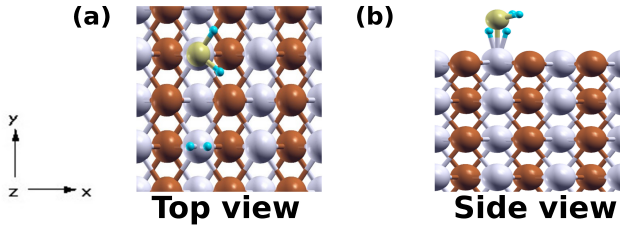


Figure 4.4: The top and side view of the most stable coadsorbed configuration.

4.3.2.2 Dissociation of H_2 and H_2S in coadsorbed form

To study the influence these coadsorbed species have on one another in their dissociation we considered three possibilities. Amongst these in two of the paths H_2S dissociation preludes the dissociation of H_2 (path1, P1) and vice-versa (path2, P2). In the last path both the molecules dissociate simultaneously (path3, P3). The end products of each of the paths consist of four H atoms, each bound to a H1 site and the S atom bound to a B2 site as shown in Figure 4.5 and Figure 4.6 for P1 and P2, respectively. However, the hollow sites occupied by the dissociated H atoms are different compared to that observed when the molecules dissociate in absence of each other. For example the H atoms resulting from H_2 dissociation usually occupy the hollow sites that are diagonally opposite to the top Pd site. However, in presence of H_2S, those H atoms occupy the hollow sites on either side of the top Pd site to which H_2 was bound to. Similarly, for H_2S, in absence of H_2, the dissociated H atoms occupy the hollow sites that are on the diagonally opposite sides of S atom. In presence of H_2 however the H atoms are found to be on the same side. We note that during the optimization of P3, it coincides with P2 suggesting that simultaneous dissociation of the molecules is not preferred. Hence, in the following only P1 and P2 are described.

P1 involves the following sequence of reaction steps:

P1;R1: $H_2S^* + H_2{}^* \rightarrow SH^* + H^* + H_2{}^*$

P1;R2: $SH^* + H^* + H_2{}^* \rightarrow S^* + H^* + H^* + H_2{}^*$

P1;R3: $S^* + H^* + H^* + H_2{}^* \rightarrow S^* + H^* + H^* + 2H^*$

In contrast, for P2 we considered the following elementary steps:

P2;R1: $H_2S^* + H_2{}^* \rightarrow H_2S^* + 2H^*$

P2;R2: $H_2S^* + 2H^* \rightarrow SH^* + H^* + 2H^*$

P2;R3: $SH^* + H^* + 2H^* \rightarrow S^* + H^* + H^* + 2H^*$

A careful observation of the two reaction pathways show that the overall mechanism is similar for both the pathways and is identical to that observed when the molecules dis-

Table 4.1: Reaction energies (E_r) and barriers (ΔE^c) for H_2S and H_2 dissociation when they are coadsorbed but infinitely away from one another and when both are coadsorbed and are 4.28 Å apart (P1 and P2). For the second SH bond dissociation, the first barrier corresponds to rotation of SH and the second one corresponds to bond cleavage. The data for H_2 dissociation in absence of H_2S have been taken from. [7]

Reaction	System					
	H_2S/H_2		$H_2S + H_2$ (P1)		$H_2S + H_2$ (P2)	
	E_r (eV)	ΔE^c (eV)	E_r (eV)	ΔE^c (eV)	E_r (eV)	ΔE^c (eV)
$H_2S^* \rightarrow SH^* + H^*$	-0.74	0.27	-0.35	0.25	-0.53	0.26
$SH^* + H^* \rightarrow S^* + 2H^*$	-0.83	0.01, 0.08	-0.79	0.04, 0.16	-0.72	0.01, 0.17
$H_2^* \rightarrow H^* + H^*$	-0.77	0.27	-0.84	0.10	-0.74	0.25

sociate in the absence of each other or when they are infinitely apart. Table 4.1 compares the reaction energies (difference between the reactants and products of a reaction), E_r and ΔE^c's of the different reaction steps when the molecules are infinitely apart and are coadsorbed with a distance of 4.28 Å between them. We observe significant differences in the reaction energies and ΔE^c's for certain reaction steps. For example, E_r for the first S-H bond cleavage is significantly reduced (by 0.39 eV for P1 and 0.21 eV for P2) when the two molecules interact with each other. E_r for the second S-H bond cleavage is not significantly affected by the interaction between the molecules. For H_2 dissociation, the reaction energy is largest for P1. In fact, for this path the H_2 dissociation barrier is reduced to 0.10 eV. This is almost half the value observed for other pathways. Moreover, for the second S-H bond cleavage, we observe that the barrier is doubled when the molecules are interacting each other. We envisage that amongst P1 and P2, the former pathway will be preferred because in that the H_2 dissociation barrier is significantly reduced. Since the overall reaction barriers are quite small, we envisage that eventually the surface will be covered with atomic H and S. The energy profiles for three elementary steps R1, R2, and R3 for P1 and P2 are shown in Figure B.6 and B.7 of Appendix B.

4.3.3 Effect of S poisoning

From Section 4.3.2 we saw that the rate determining step of H_2S dissociation is the first S-H bond cleavage. However, the barrier from the same is low and at high operating temperature of the membrane it will cleave easily. Once the first S-H bond is broken, the second bond will break very easily. Hence, eventually it will be the S species adsorbed on the surface that will occupy the sites. Therefore, we have considered only the role of S on

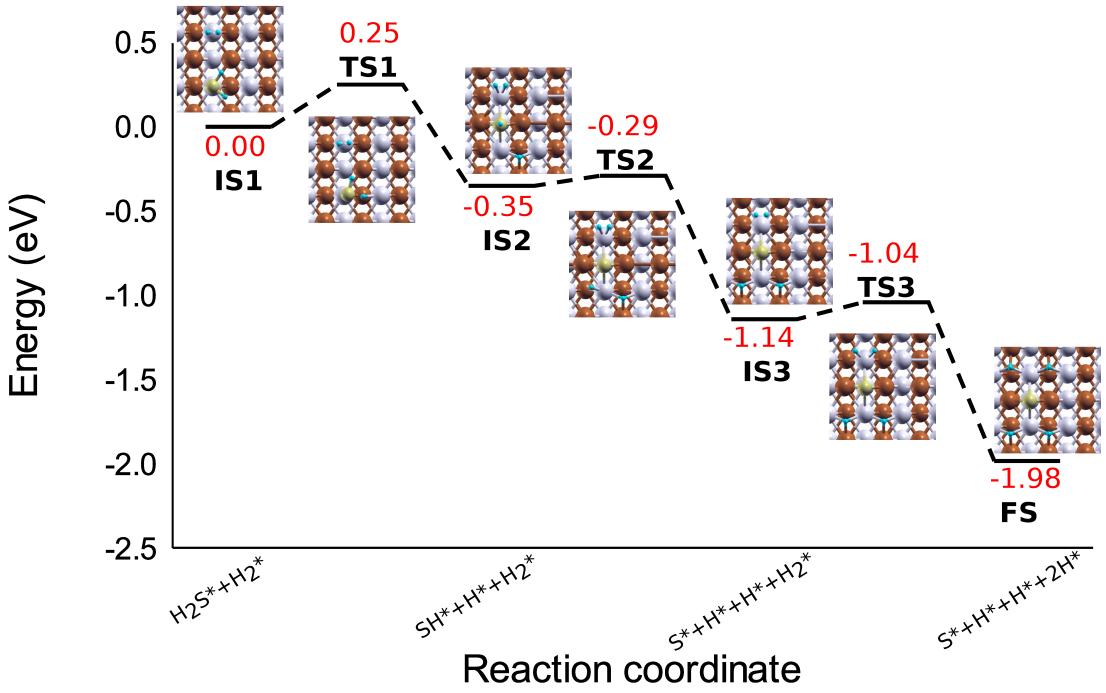


Figure 4.5: The energetics and geometries of the initial states(IS), Transition states(TS), and final state(FS) for H_2 and H_2S coadsorbed dissociation reaction. The numbers in red are the reaction energies calculated with respect to H_2 and H_2S on the surface.

the poisoning.

4.3.3.1 Coadsorption of atomic S and H at $\Theta_{H,S}$ = 0.16 ML

At low coverages, the most stable adsorption sites are accessible to both S (B2 site) and H (H1 site). Hence to determine the lowest energy configuration of coadsorption of S and H at this coverage, we considered different cases where the S (H) is occupying the B2 (H1) site and varied the distance between them. The various configurations with different S-H distance are shown in Figure B.8 of Appendix B. The smallest (largest) separation between the two atoms is 2.42 (4.71) Å. The H adsorption energies ($E_{ads}^{H;S}$)are computed with respect to the surface containing S atoms and is given by:

$$E_{ads}^{H;S} = E_{surface+S+H} - (E_{surface+S} + E_H) \tag{4.4}$$

where $E_{surface+S+H}$, $E_{surface+S}$, and E_H are the energies of the surface with S and H coadsorbed, only S adsorbed and atomic H in vacuum respectively. Figure 4.7 shows the adsorption energy as a function of d_{S-H}. We find that as the S-H distance goes beyond

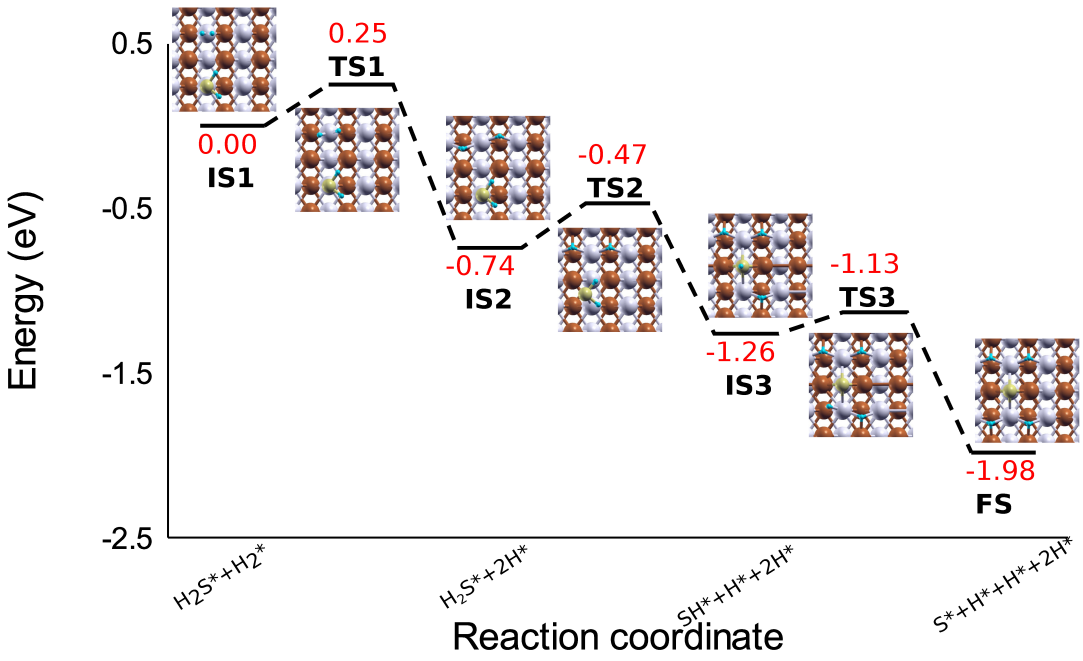


Figure 4.6: The energetics and geometries of the initial states(IS), Transition states(TS), and final state(FS) for H_2 and H_2S coadsorbed dissociation reaction. The numbers in red are the reaction energies calculated with respect to H_2 and H_2S on the surface.

3.56 Å, $E_{ads}^{H;S}$ does not change. At 3.56 Å $E_{ads}^{H;S}$ is about -0.54 eV/H atom while it reduces to -0.42 eV/H atom when the separation between the S and H atoms are reduced further. We note that the H adsorption energy of the most stable configuration of S and H coadsorption is about 0.01 eV higher than that observed for H adsorption in absence of S. [7] This suggests that the interaction between atomic S and H on this surface is weakly repulsive in nature.

4.3.3.2 Effect of S poisoning on H adsorption

In membrane reactors hydrogen partial pressure is high at the feeder side. Hence, in this study, we have focused on cases where H adsorption is high, namely, Θ_H = 1.00, 1.16, and 1.50 ML. We did not consider higher H coverages because beyond 1.50 ML both H1 and H2 sites need to be occupied. However, the H2 sites are very close to B2 site and in presence of S some of the B2 sites being occupied will make the H2 sites near the occupied B2 sites inaccessible for H adsorption. Further, for each of the above H coverage we considered S coverage of, Θ_S = 0.16, 0.33 and 0.50 ML.

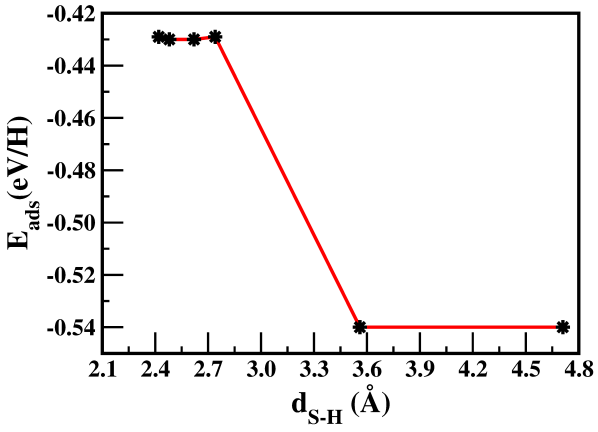


Figure 4.7: Adsorption energy of H at 0.16 ML of S as a function of distance (d_{S-H})

To find the most stable configurations of H and S coadsorption at different H and S coverages, we used two distance criteria, namely, $d_{S-H} > 3.00$ Å and $d_{S-S} > 5.24$ Å. This is chosen based on the results of coadsorptions of one H and S atom and two S atoms on the surface. The above two criteria can be easily fulfilled at lower H, S coverages and it may deviate for higher coverages. The lowest energy configurations for each combination of Θ_H and Θ_S are shown in Figure B.9 of Appendix B.

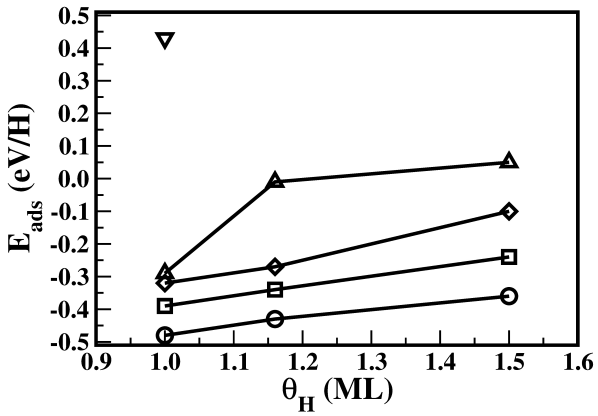


Figure 4.8: The adsorption energy of H for different H coverage as a function of S coverage. The open circle symbols are for S coverage of 0.00 ML. The open square symbols are for S coverage of 0.16 ML. The open diamond symbols are for S coverage of 0.33 ML. The triangle-up symbols are for S coverage of 0.50 ML. The triangle-down symbol is for S coverage of 1.00 ML

Figure 4.8 shows the H adsorption energy as a function of H coverage in presence of S. Similar to that observed in absence of S, we find that H adsorption becomes thermody-

namically less favourable as the H coverage is increased. However, in presence of S, for a fixed H coverage, H adsorption becomes less exothermic than that observed in absence of S. Further, when the S coverage is about 0.50 ML and the H coverage is 1.16 ML and above, H adsorption becomes completely endothermic.

4.3.3.3 Effect of Sulphur poisoning on the H_2 dissociation at higher H coverage ($1.00 \leq \Theta_H \leq 1.50$ ML)

In addition to the fact that S poisoning effect H adsorption at large coverages, it might also affect the dissociation of molecular hydrogen, particularly at larger H coverages. In this section we investigate how the presence of S affects H_2 dissociation.

To find the thermodynamically favourable adsorption configuration of H_2 (initial state for the reaction) for a given H and S coverage, the H_2 molecule was placed at each of the available top Pd sites (stable site for H_2 adsorption) and the geometry was relaxed. Amongst them the lowest energy configuration was considered as the initial state (IS). Given an initial state configuration, for the final state (FS), i.e. where the molecule dissociates, there are two possibilities: (a) the dissociated H atoms occupy hollow sites that are diagonally opposite to the top Pd site or (b) they occupy the hollow sites that are on the either sides of the top Pd site. Out of these two the lowest energy configuration was considered as the final state. All the configurations of the initial and final states considered for the NEB calculations for all coverage of H and S atoms are shown in Figure B.10 of Appendix B.

In absence of S ($\Theta_S = 0.00$ ML), we observe that as the Θ_H increases from 1.00 to 1.16 to 1.50 ML, the binding energy of a hydrogen molecule decreases from -0.24 eV to -0.21 eV and farther to -0.01 eV at 1.50 ML. For all the cases we observe that H_2 adsorbs in an activated form with the H-H bond length varying between 0.82 - 0.84 Å. While the dissociation barriers for $\Theta_H = 1.00$ and 1.16 ML are similar, 0.29 eV and 0.28 eV respectively, that for the 1.50 ML coverage is reduced to 0.16 eV. The trends in the dissociation barrier correlates with that of the reaction energies (difference between FS and IS energies).

In Table 4.2 we report the energetics and geometry of the adsorbed H_2 molecule and H_2 dissociation on the surface as a function of Θ_H and Θ_S. For $\Theta_H = 1.00$ and 1.16 ML we have considered $\Theta_S = 0.16$, 0.33 and 0.50 ML while at Θ_H =1.50 ML, we did not consider $\Theta_S = 0.50$ ML because at such large H and S coverage there is not enough site for H_2 adsorption. At 1.00 ML H coverage we find that H_2 binding to the surface is

endothermic irrespective of the S coverage. In contrast, for $\Theta_H = 1.16$ ML, H_2 binding is weakly exothermic when $\Theta_S = 0.50$ ML. When the H coverage is increased to 1.50 ML, we find the binding of H_2 to be weakly exothermic. Except for $\Theta_H, \Theta_S = 1.16$, 0.50 ML and $\Theta_H, \Theta_S = 1.50$, 0.33 ML H_2 binds in an activated form on the surface Pd atom.

At a given H coverage, depending on the concentration of S, H_2 dissociation barrier either decreases or increases compared to that observed in absence of S. For example when $\Theta_H = 1.00$ ML, at all surface coverage the dissociation barrier is reduced to almost half of that observed in absence of S. Similar reduction is also observed when $\Theta_H = 1.16$ ML and $\Theta_S = 0.16$ and 0.33 ML. When the S coverage is further increased the dissociation barrier increases to 0.94 eV. Upon further increasing the H coverage to 1.50 ML, we observe that presence of S increases the dissociation barrier. Compared to that of 0.16 eV in absence of S, when 0.16 ML of S is present the barrier is increased to 0.30 eV. Doubling the S coverage to 0.33 ML enhances the barrier to 1.07 eV. The lowering of the barrier at low S coverage can be understood from the fact that the reaction energy that provides the thermodynamic driving force for the reaction to happen is enhanced compared to that in absence of S. This is achieved by weakening of the H_2 binding energy on the surface in presence of H. However, as the S and H coverage is enhanced, the less favourable sites start getting occupied by atomic H and S thereby reducing the stability of the FS of the reaction. This results in not only reducing the magnitude of the reaction energy but also makes the reaction endothermic, thereby increasing the H_2 dissociation barrier. The dissociation pathways for each H, S coverages are shown in Figure B.11 of Appendix B.

Table 4.2: H-H bond length of H_2 (d^{IS}_{H-H}), binding energy of H_2 (E_{BE}), reaction energy of H_2 dissociation (ΔE) and dissociation barriers (E_a)at different H and S coverage (Θ_H and Θ_S).

Θ_H (in ML)	Θ_S (in ML)	d^{IS}_{H-H} (in Å)	E_{BE} (in eV)	ΔE (in eV)	E_a (in eV)
1.00	0.00	0.824	-0.24	-0.59	0.29
	0.16	0.824	0.13	-0.69	0.13
	0.33	0.824	0.09	-0.65	0.13
	0.50	0.818	0.08	-0.56	0.16
1.16	0.00	0.838	-0.21	-0.45	0.28
	0.16	0.822	0.15	-0.69	0.13
	0.33	0.828	0.11	-0.66	0.13
	0.50	0.753	-0.02	0.37	0.94
1.50	0.00	0.819	-0.01	-0.65	0.16
	0.16	0.817	-0.01	-0.19	0.30
	0.33	0.752	-0.02	0.33	1.10

4.3.3.4 Effect of Sulphur poisoning on surface to sub-surface diffusion at Θ_H = 1.16 and 1.50 ML

The penetration of the H atom from the stable surface site to the stable subsurface site is another prime step in the hydrogen permeation mechanism. For a good permeation membrane, this process should have small barrier. In this section, we have studied the effect of S poisoning on the kinetics of H penetration/diffusion from surface to the subsurface layer of the membrane as a function of S coverage when Θ_H is 1.16 and 1.50 ML. While for Θ_H = 1.16 ML we considered S coverage of 0.00, 0.16, 0.33 and 0.50 ML, for Θ_H = 1.50 ML we have considered S coverage of 0.00, 0.16 and 0.33 ML.

In this process the final state corresponds to a configuration where one of the surface H atoms move to the subsurface layer. There are three inequivalent subsurface sites: (a) two octahedral sites (Oh) and (b) one tetrahedral site (Td). One of the two octahedral site consist of four Pd atoms at the corners of a square and two Cu atoms occupying the axial position of the octahedron and vice-versa for the other one. The tetrahedral site consist of two Pd atoms and two Cu atoms at the corners of a tetrahedron. In a previous work by some of the authors we have shown that H absorption in the tetrahedral site is preferable over absorption in the octahedral site by about 0.02 eV/H atom [7]. However, presence of S might change the preferred sub-surface occupation sites. Hence, we have considered both the sites for subsurface occupation. Our calculations show that at Θ_H = 1.16 and 1.50 ML and Θ_S = 0.00, 0.16, and 0.33 ML it is the tetrahedral site that is thermodynamically favourable. The only exception is Θ_H = 1.16 ML and Θ_S = 0.50 ML where the octahedral site is the preferred one for sub-surface H absorption. The initial and final states considered at H coverage of 1.16 and 1.50 ML for penetration step are shown in Figure B.12 of Appendix B.

Table 4.3: H penetration barriers and difference between the final and initial state energy (ΔE) at different H and S coverage.

Θ_H (ML)	Θ_S (ML)	E_{act} (eV)	ΔE (eV)
1.16	0.00	0.25	0.22
	0.16	0.16	0.08
	0.33	0.28	0.04
	0.50	0.23	-0.10
1.50	0.00	0.21	0.17
	0.16	0.19	0.08
	0.33	0.10	-0.18

Table 4.3 tabulates the difference between the final and initial state energies and the activation barriers for surface to subsurface diffusion. The energy profile for the diffusion process is shown in Figure B.13 of Appendix B. In most of the cases, there involves two barriers, a first one that involves vertical diffusion of H from surface to sub-surface octahedral site. This is followed by further diffusion from sub-surface octahedral to tetrahedral site. In this later case the H atom moves within the subsurface layer. At $\Theta_H = 1.50$ ML, we observe that presence of S lowers the diffusion barrier by making the subsurface sites more stable and there by increasing the driving force for the diffusion process to occur. In contrast, for 1.16 ML H coverage, we do not observe any such trends. Compared to the S-free case, the barrier is lowered by about 0.09 eV in presence of 0.16 ML S. However, if the S coverage is increased further, the activation energy for the diffusion increases, even though S coverage tend to stabilize the subsurface absorption. Presently, we do not understand the reason for the above mentioned observation.

4.3.3.5 Temperature Dependent Kinetics

Table 4.4 below tabulates the quantum corrected barriers and the rate constants of the dissociation and penetration steps involved in the permeation mechanism of H through a modelled PdCu membrane at 300 K. Figure 4.9 below shows the effect of S impurities on the temperature dependence of the rate constants associated with above-mentioned two processes. We note that we have not considered diffusion of H inside the bulk and from sub-surface to surface on the permeate side of the membrane because: (a) S impurities on the feed side of the membrane will not affect these processes, and (b) from our earlier study we found that these are one of the fastest processes and are almost temperature independent. In absence of S impurities we saw that only at temperatures greater than 320 K, dissociation of molecular H_2 on the clean surface is faster than the two above mentioned processes. Further, in presence of dissociated H adsorbed on the surface, the dissociation rate of molecular hydrogen decreases further. In contrast, in presence of 0.16 ML S we observe that H_2 dissociation rates increase and show weak temperature dependence. In particular, in absence of any preadsorbed atomic H on the surface the H_2 dissociation rate is almost similar to that of diffusion of H from sub-surface to surface on the feeder side. Similar behaviour is observed when Θ_S is increased to 0.33 ML and H coverage is about 1.16 ML. However, further enhancement of H coverage to 1.50 ML makes this process the slowest one.

In absence of S poisoning, the penetration of surface H to subsurface at very low H

coverage is one of the second most slowest processes. The rates of this process can be increased by increasing the H coverage. However, they are still lower than H_2 dissociation rates. In presence of S the variation of this penetration rate with respect to that of the other processes remain similar. However, we observe that depending on the S coverage and the H coverage the penetration rates can be either faster or slower than that observed in absence of S. Comparing all the processes, we find that in absence of S poisoning, at temperatures less than 500 K the rate limiting step for hydrogen permeation is the reassociation of H atoms on the feeder side. At membrane operating temperatures higher than 500 K, the rate limiting step is the H penetration from the feeder side at low H coverage. In contrast, at low amount of S poisoning (Θ_S = 0.16 ML), it is the reassociation that is the rate limiting step. However, if the S content is enhanced further, i.e., $\Theta_S = 0.33$ ML, the dissociation of H_2 at high H coverage on the feeder site is the slowest process.

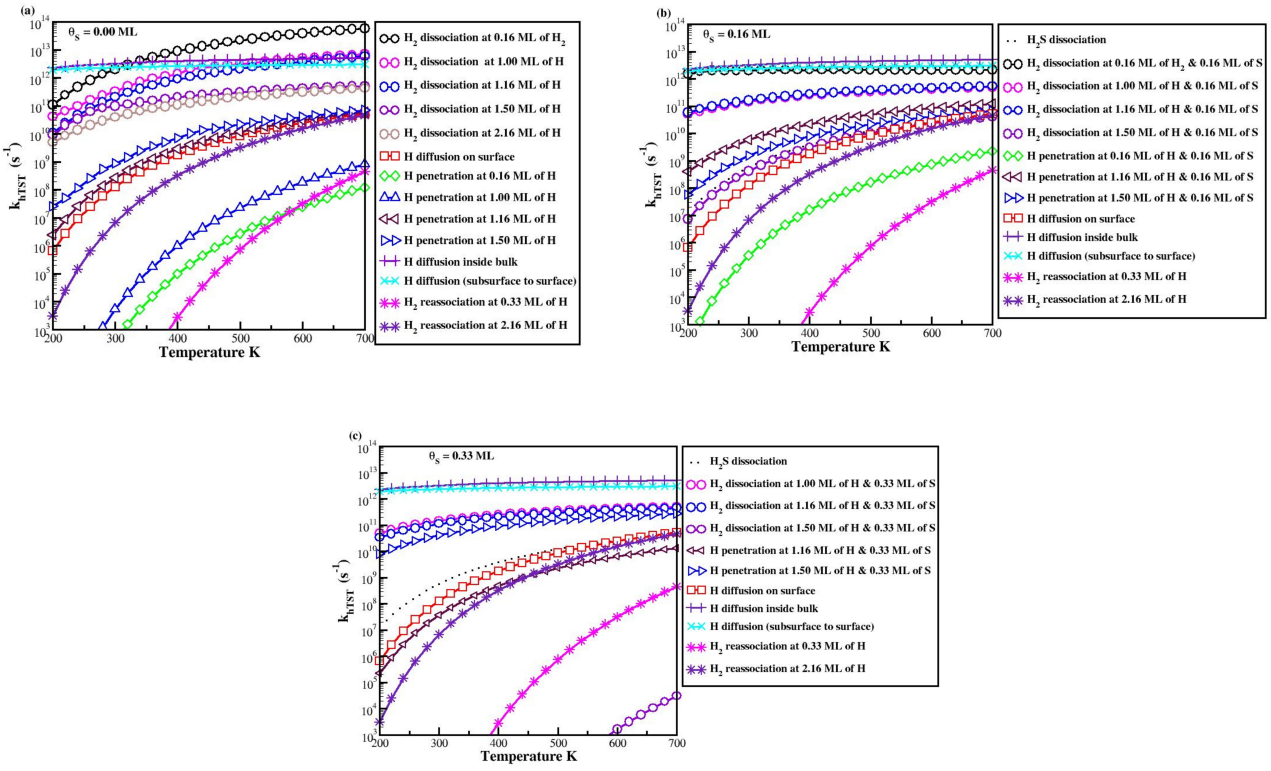


Figure 4.9: Rate constants for some important processes involved in the solution diffusion mechanism as a function of temperature

.

Table 4.4: Quantum-Corrected Barriers (ΔE^q), Classical Barriers (ΔE^c), Arhenius Prefactor, and Rate Constants (k_{hTST})

	ΔE^q (eV)	ΔE^c (eV)	prefactor (s^{-1})	k_{hTST} at 300K (s^{-1})
H_2 dissociation Θ·H·2= $0.16MLand$				
Θ·S= $0.16ML$	0.02	0.07	1.48x10^{12}	2.07x10^{12}
H_2 dissociation Θ·H= $1.00MLand$				
Θ·S= $0.16ML$	0.06	0.13	1.27x10^{12}	1.46x10^{11}
H_2 dissociation Θ·H= $1.00MLand$				
Θ·S= $0.33ML$	0.06	0.13	1.26x10^{12}	1.46x10^{11}
H_2 dissociation Θ·H= $1.00MLand$				
Θ·S= $0.50ML$	0.09	0.16	1.21x10^{12}	4.36x10^{10}
H_2 dissociation Θ·H= $1.16MLand$				
Θ·S= $0.16ML$	0.05	0.13	1.29x10^{12}	1.64x10^{11}
H_2 dissociation Θ·H= $1.16MLand$				
Θ·S= $0.33ML$	0.06	0.13	1.25x10^{12}	1.11x10^{11}
H_2 dissociation Θ·H= $1.16MLand$				
Θ·S= $0.50ML$	0.90	0.94	1.13x10^{12}	8.39x10^{-4}
H_2 dissociation Θ·H= $1.50MLand$				
Θ·S= $0.16ML$	0.21	0.30	1.33x10^{12}	4.12x10^{8}
H_2 dissociation Θ·H= $1.50MLand$				
Θ·S= $0.33ML$	1.05	1.10	1.16x10^{12}	2.38x10^{-6}
H penetration Θ·H= $0.16MLand$				
Θ·S= $0.16ML$	0.40	0.46	1.61x10^{12}	3.39x10^{5}
H penetration Θ·H= $1.16MLand$				
Θ·S= $0.16ML$	0.14	0.16	1.22x10^{12}	5.41x10^{9}
H penetration Θ·H= $1.16MLand$				
Θ·S= $0.33ML$	0.27	0.28	1.09x10^{12}	3.73x10^{7}
H penetration Θ·H= $1.16MLand$				
Θ·S= $0.50ML$	0.22	0.23	0.95x10^{12}	6.28x10^{7}
H penetration Θ·H= $1.50MLand$				
Θ·S= $0.16ML$	0.17	0.19	1.12x10^{12}	1.53x10^{9}
H penetration Θ·H= $1.50MLand$				
Θ·S= $0.33ML$	0.09	0.10	1.09x10^{12}	4.08x10^{10}

4.4 Conclusions

In summary, in an effort to understand the effect of impurity on various steps in hydrogen permeation mechanism, we have studied the dissociation process of hydrogen sulphide H_2S on the PdCu(110) surface. We find that this is an activated process with an energy barrier of 0.27 eV. Further, we found the effect of impurity to be the most dominant at its higher coverage during the hydrogen adsorption, hydrogen dissociation and hydrogen penetration steps. The barrier for hydrogen dissociation increases as the coverage of sulphur impurity increases for a particular coverage of H atoms, and decreases for hydrogen penetration step as coverage of impurity increases at higher coverage of H atoms. The presence of impurity with high partial pressure of hydrogen at the feed side on the surface of PdCu(110) membrane eases the hydrogen penetration step with increase in impurity coverage as compared to hydrogen dissociation step. Evaluating, the rate constants associated with the individual processes, we put forward the two rate-limiting steps for hydrogen permeation through this membrane (i) reassociation of atomic H atoms at θ_S = 0.16 ML (ii) dissociation of H_2 at θ_S = 0.33 ML, high H coverage. Rates governing the above rate-limiting steps can be enhanced at high temperatures.

Appendix A

Appendix A

A.1 Oxygen adsorption on Pure and alloyed Ti(0001) surfaces at higher oxygen coverage θ_O>0.06 ML

The different combinations that we have looked for the adsorption energy as a function of distance between two oxygen atoms for both Pure Ti and alloyed Ti(0001) surfaces is shown in the Figure A.1.

A.1.1 Pure Ti(0001) surface

The three inequivalent configurations for the Pure Ti(0001) in the case of O coverage of 0.13 ML are shown in Figure A.2. Figure A.3 shows the variation of E_{ads} as a function of distance between two oxygen atoms (in angstrom) below. The different configurations considered for Pure Ti(0001) surface at 0.50 ML coverage of oxygen are shown in Figure A.4.

A.1.2 Alloyed(Ti(0001)) surface

Adsorption Energy as a function of distance between two oxygen atoms (in angstrom) shown in Figure A.5 and A.7 for the d-block and p-block elements repectively. At 0.50 ML oxygen coverage, the different configurations considered for the d-block elements are shown in Figure A.6 and in Figure A.8 for p-block elements.

A.1.3 Thermodynamic analysis

Stability of different surfaces, both clean and in the presence of adsorbate at various O coverages, can be determined based on their free energies. In order to account for the

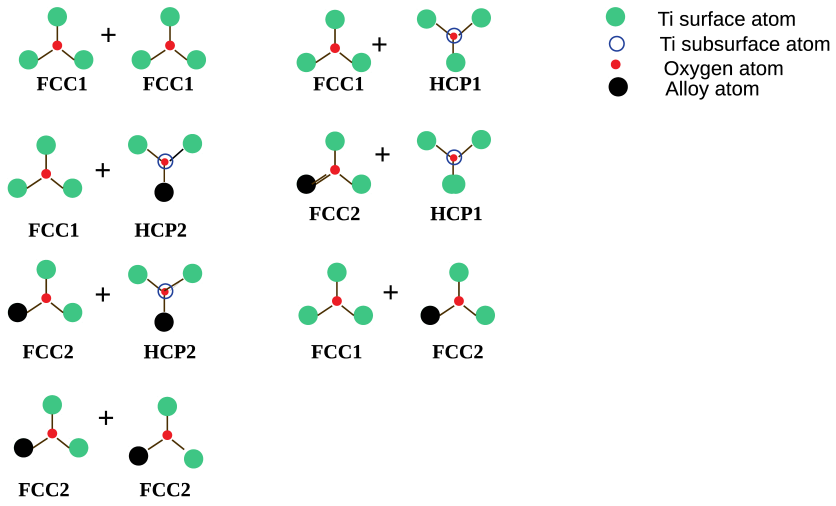


Figure A.1: The different possible combination of sites on the surface

.

effect of varying gas-phase temperature and pressure on the stability of a surface configuration, we apply concepts from classical thermodynamics. The free energy (F) of a system gives a measure of stability of the system. In the grand-canonical ensemble (GCE), assuming that the surface is in equilibrium with the adsorbates, the Gibbs free energy (F) is given by equation A.1.

$$F = E + PV - TS - \sum_i n_i \mu_i \tag{A.1}$$

where P, V, T and S are the pressure, volume, temperature and entropy, respectively. n_i and μ_i are, respectively, the number of molecules and the chemical potential of species i at the surface. E is the internal energy of the system and is obtained from the DFT calculations. In order to apply these concepts, one needs to have a clear distinction between what we consider as "system" and that which we take to be its "surroundings". In this paper the system is considered to include the surface, the adsorbed molecules on the surface and the gas above the surface; the surroundings include only the world beyond some external gas container. Taking this view, the number of particles in the system is now fixed but the entropy is considerably large, since it includes large translational and rotational contributions from the gas molecules which are not adsorbed on the surface. Hence equation A.1

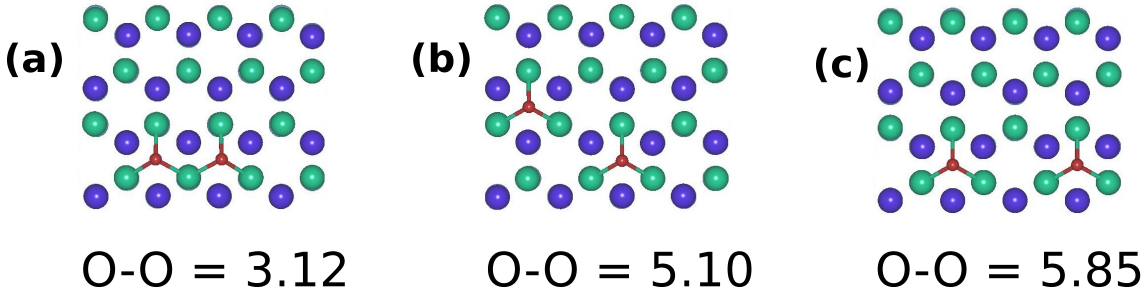


Figure A.2: The three inequivalent configurations for the case of Pure Ti(0001), where the two O atoms are 3.12 (in (a)), 5.10 (in (b)) and 5.85 Å(in (c)). In the figure, the distances are given in Å.

is modified as

$$F^s = E + PV - TS \tag{A.2}$$

Now we calculate the necessary free energy that must be minimized. This can be done by defining free energies relative to that of the surface without adsorbate. The change in free energy upon O adsorption with respect to the clean surface is given by:

$$\delta F^s = \frac{F^s_{slab+O} - F^s_{slab} - (n_O/2)F^s_O}{N_s} \tag{A.3}$$

where F^s_{slab}, F^s_{slab+O} and F^s_O are the free energies of the surface in presence of oxygen, the clean surface and the oxygen molecule in gas phase respectively. n_O and N_s denote the number of O atoms adsorbed on the surface and the number of (1×1) surface unit cells respectively. To evaluate the free energy of the solid phases, i.e. F^s_{slab+O} and F^s_{clean}, we ignore the effects of TS (because entropy of the solid phase is negligible compared to that of the gas phase) and PV. With all these approximations the free energy of the solid phases equals the internal energy obtained from the DFT calculations.

For O in the gas phase, PV is obtained by assuming that the gas phase obeys the ideal gas equations. In order to compute the contribution of TS to F^s_O for the O in gas phase at different temperatures and pressures we have taken the values of S at a pressure of 1 bar and for a temperature range of 300-1500K from the CRC handbook. We then derive the variation of S with pressure and temperature from the following formula:

$$S(T,P) = S(T,P^o) - Rln(p/p^0) \tag{A.4}$$

p^o(=1 bar) is the reference pressure and R is the universal gas constant. We plotted δF^s as a function of at different pressures (varying from 10^{-50} to 10^{-100}) for both pure and

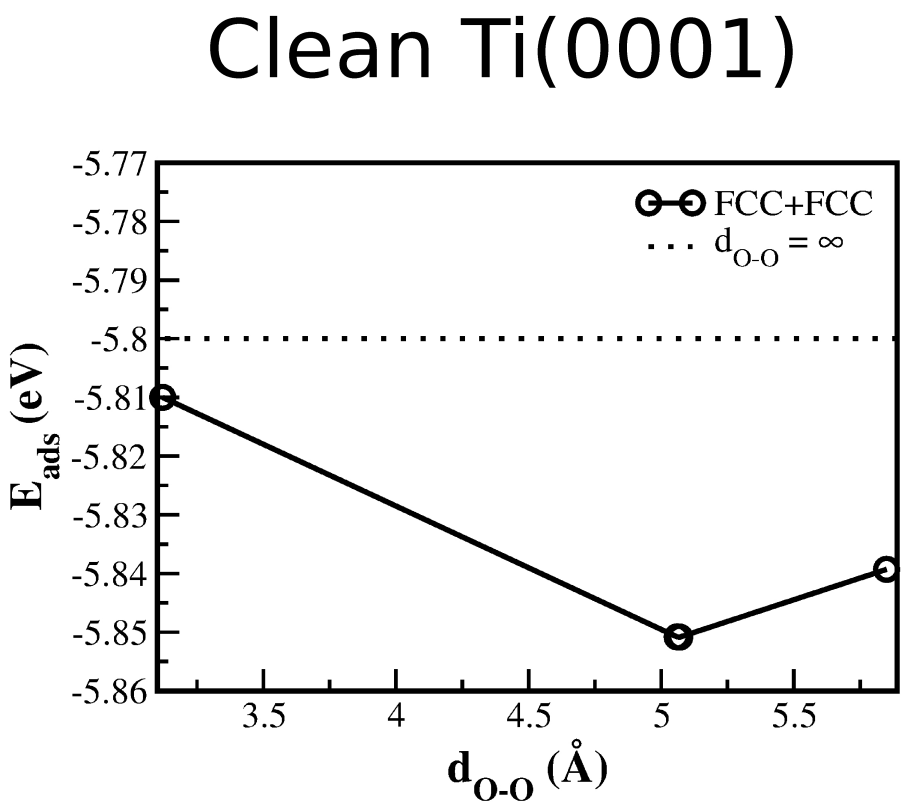


Figure A.3: E_{ads} as a function of d_{O-O} in angstrom for the case of Pure Ti(0001).

alloyed Ti(0001) surfaces. The plots are shown in Figures A.9, A.10, A.11, A.12, A.13, A.14, A.15, A.16, and A.17 for the clean and alloyed surfaces. The temperature at which the crossover in the stability occurs for different surfaces as a function of pressure is obtained and based on this we have plotted the pressure vs temperature phase diagrams for both clean and alloyed Ti(0001) surfaces.

Charges on surface atoms The charges on surface metal atoms at 0.06, 0.50 and 1.00 ML oxygen coverages for clean Ti(0001) and alloyed Ti(0001) surfaces are given below in Figures A.18, A.19, A.20, A.21, A.22, A.23, A.24, A.25, and A.26.

A.1.4 Diffusion barrier of oxygen from the surface into the subsurface layer at lower and higher oxygen coverage

Energy profile for oxygen diffusion at 0.06, 0.50 and 1.00 ML oxygen coverage shown in Figure A.27, A.28 and A.29 below.

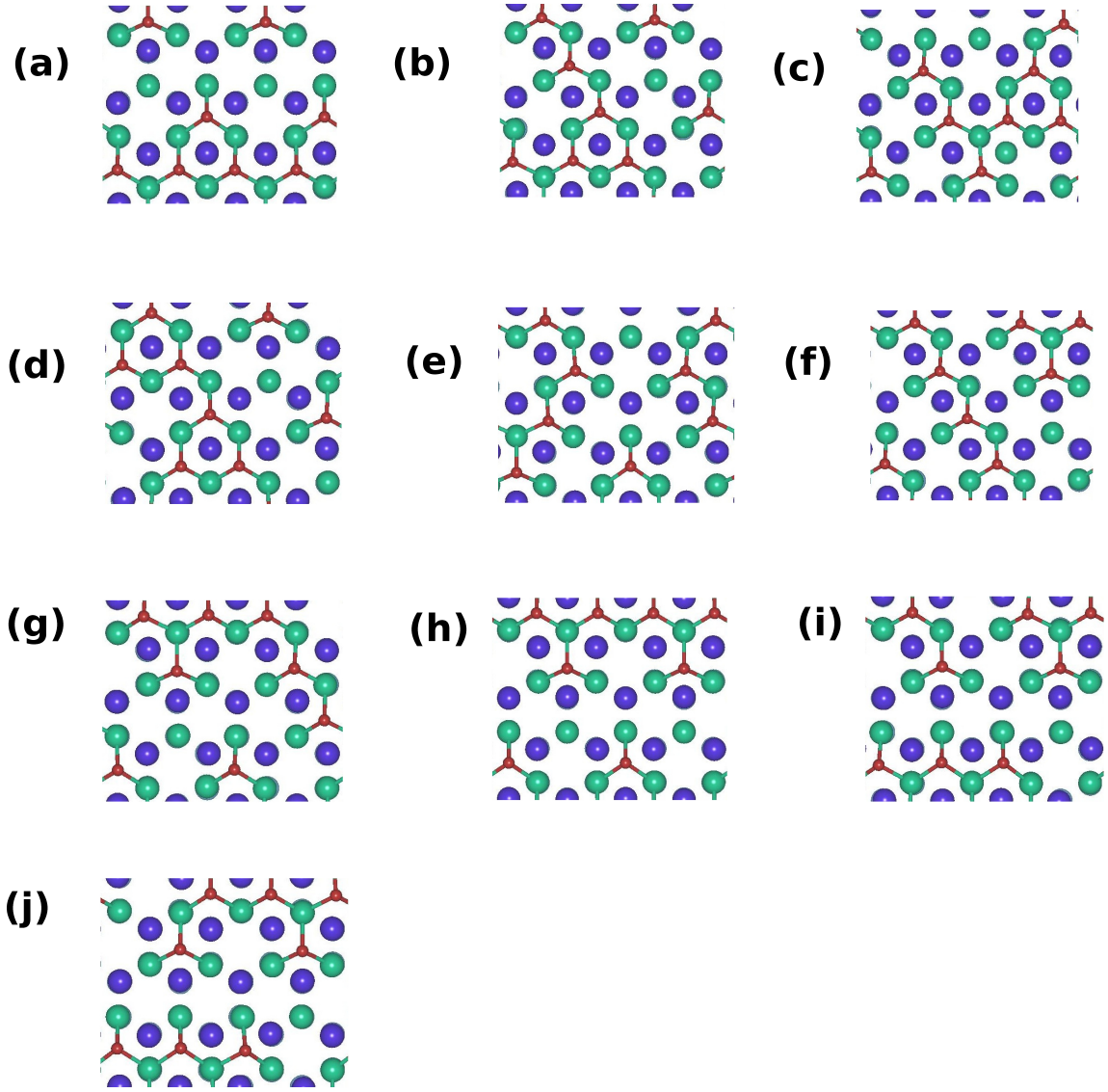


Figure A.4: (a)-(j) are the inequivalent configurations of oxygen adsorption on pure Ti(0001), at 0.50 ML O-coverage.

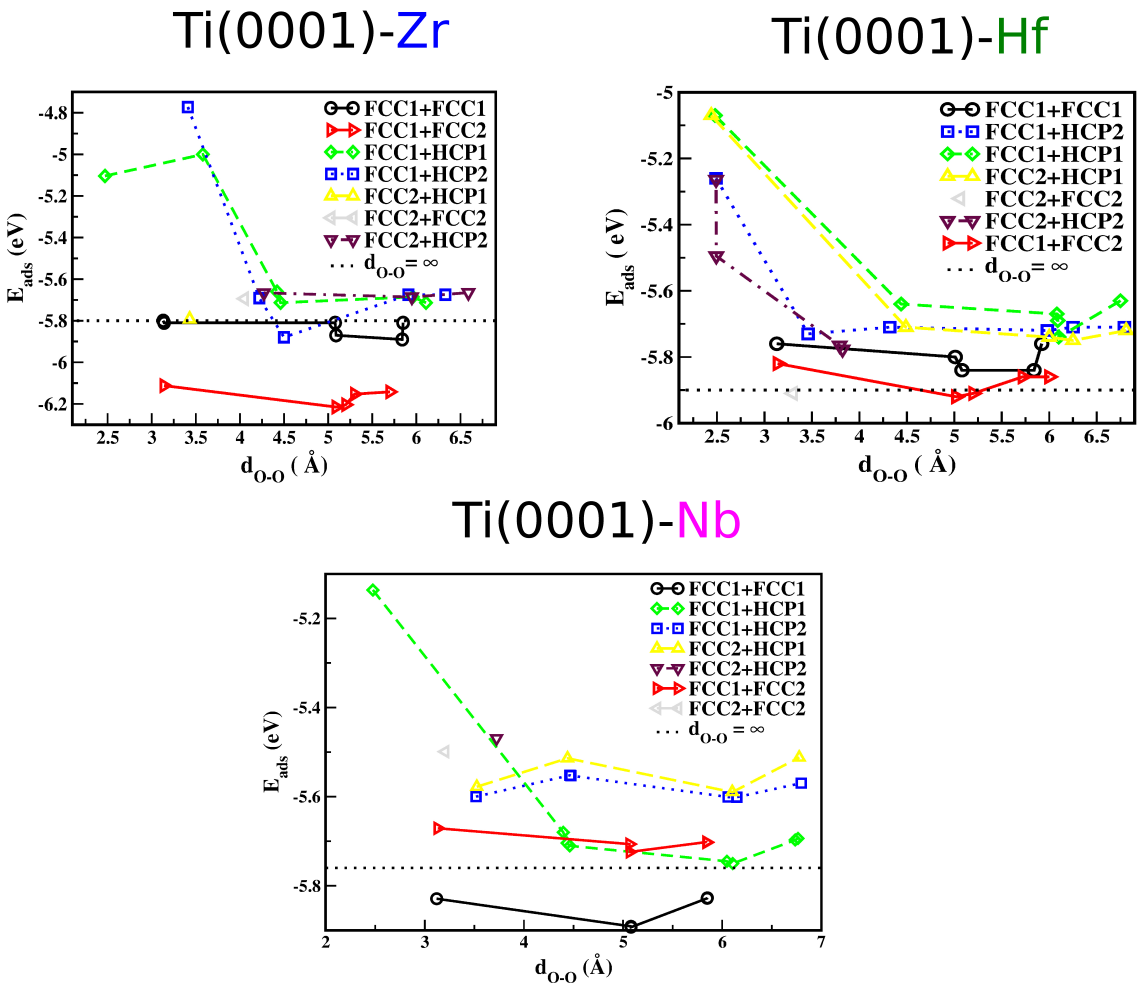


Figure A.5: E_{ads} as a function of d_{O-O} in angstrom for the case of d-block elements.

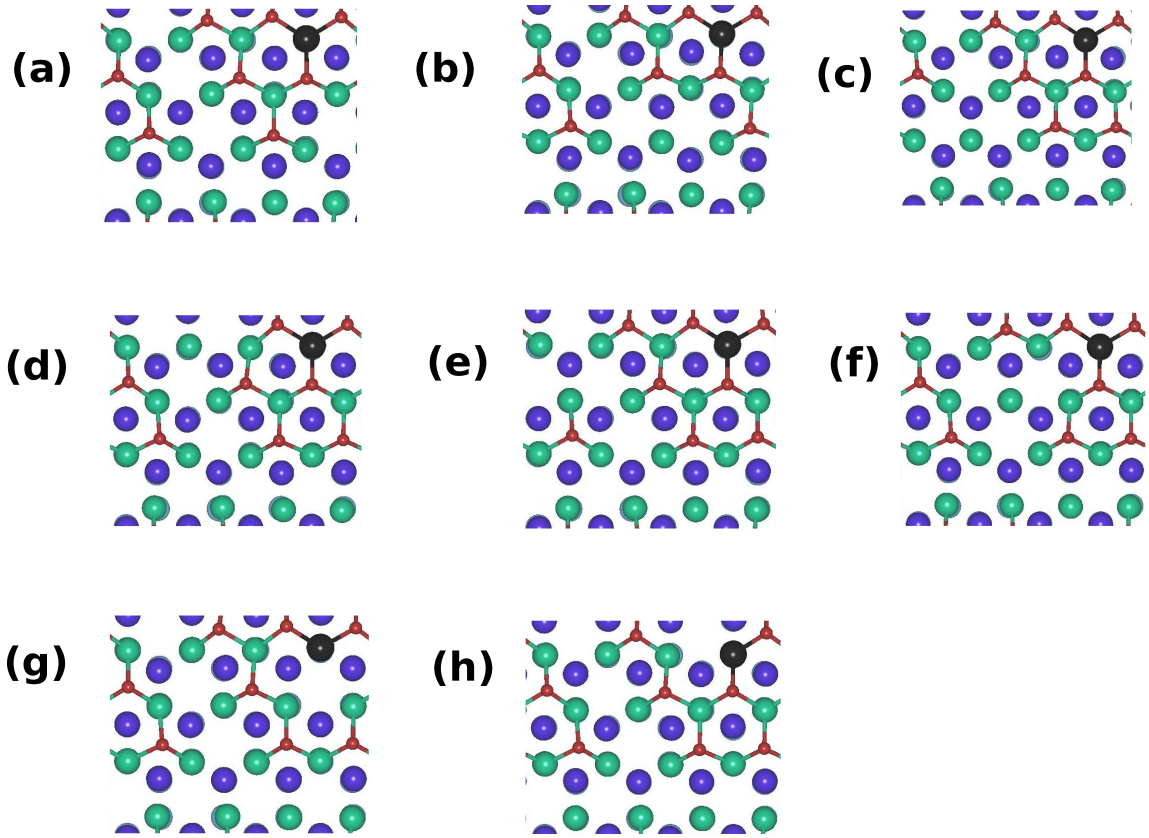


Figure A.6: (a)-(h) are the different inequivalent configurations considered for O adsorption on alloyed Ti(0001) surface at 0.50 ML O coverage. The alloying elements belong to the d-block.

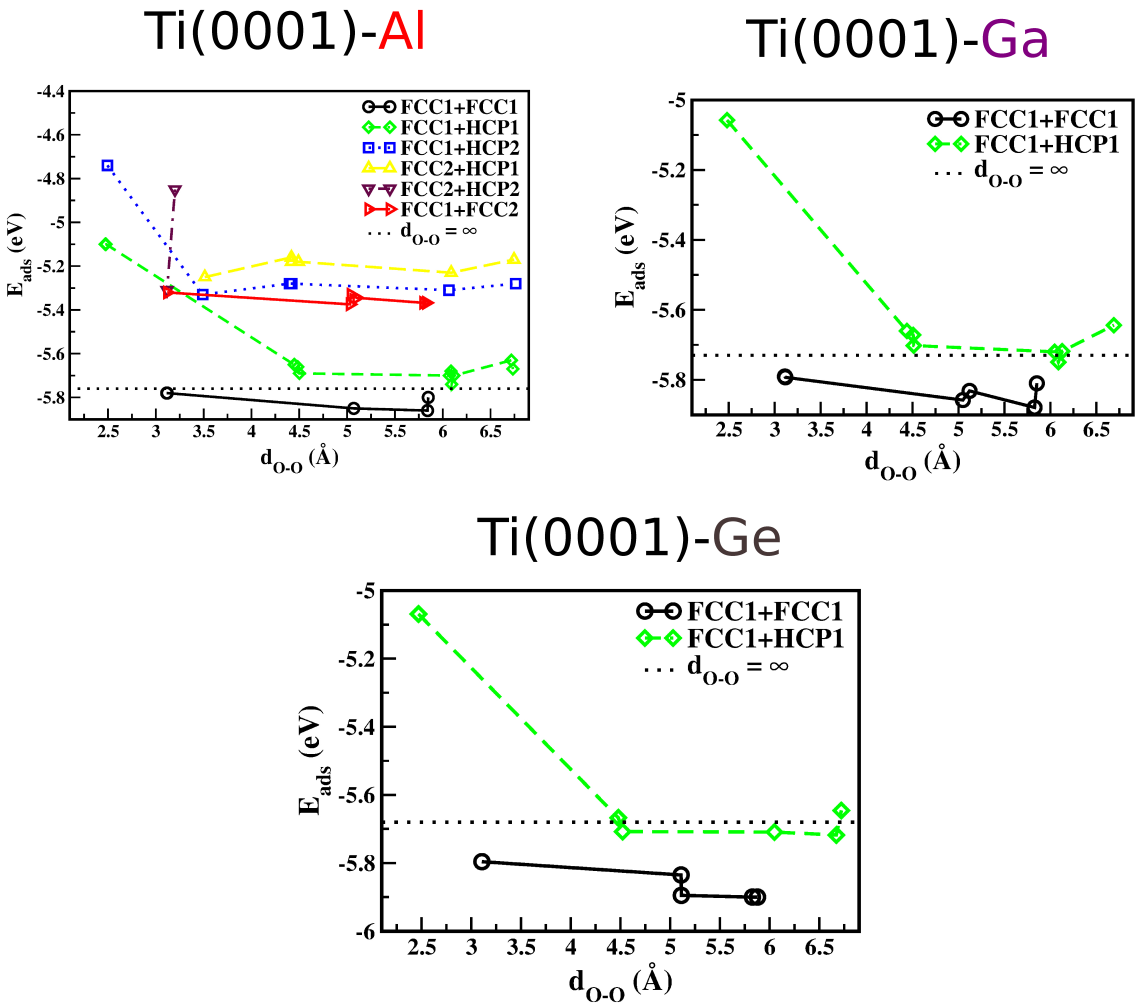


Figure A.7: E_{ads} as a function of d_{O-O} in angstrom for the case of p-block elements.

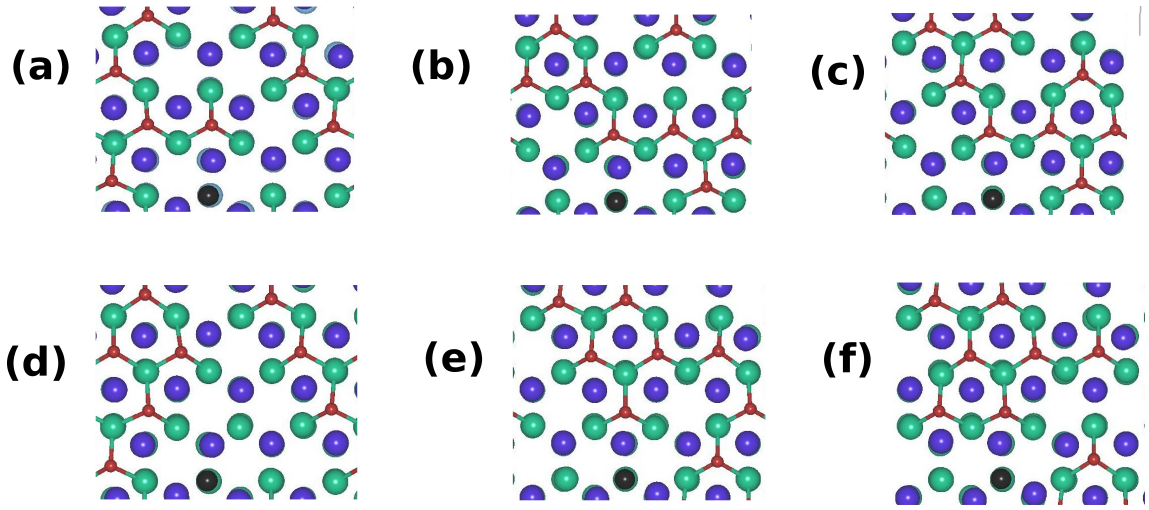


Figure A.8: (a)-(f) are the different inequivalent configurations considered for O adsorption on alloyed Ti(0001) surface at 0.50 ML O coverage. The alloying elements belong to the p-block.

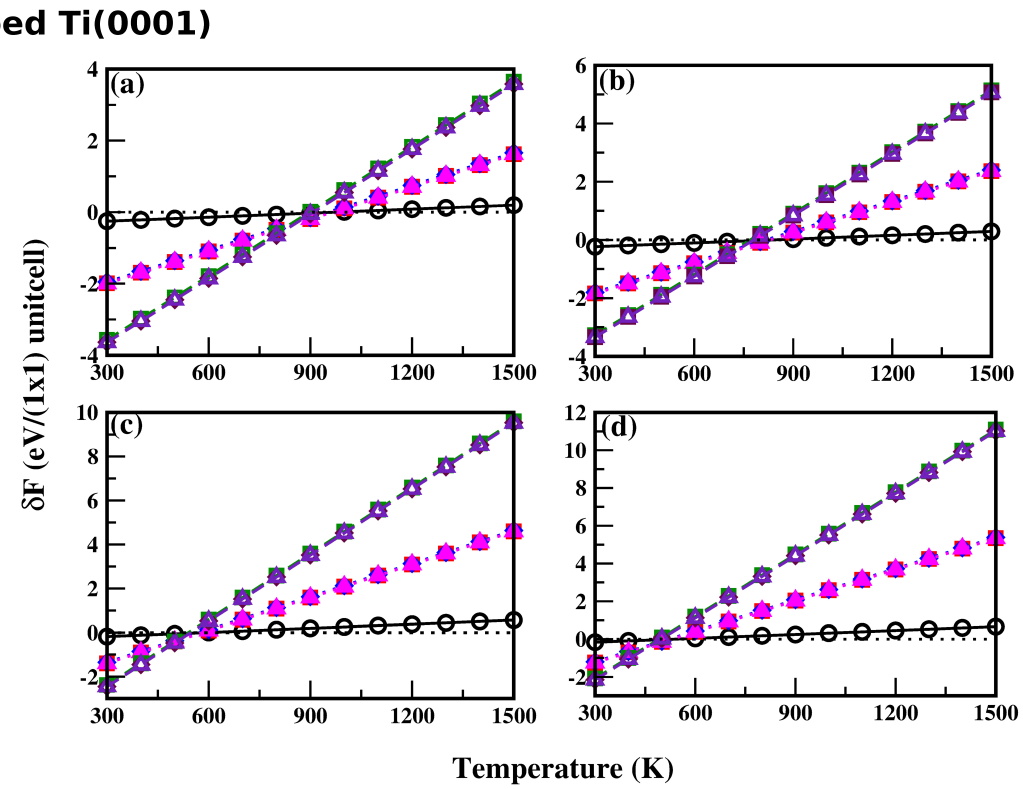


Figure A.9: Free energies relative to that of the surface without adsorbate (δF) as a function of temperature at different pressures: (a) 10^{-50}, (b) 10^{-60}, (c) 10^{-90}, and (d) 10^{-100} bar. The dotted-line without any symbol denote the surface without adsorbate. The solid-line with open circles represent surface at oxygen coverage of 0.06 ML. The dotted-line with closed squares, dashed-line with open squares represents surfaces at coverages of 0.50, 1.00 ML, respectively. The dotted-line with closed diamonds, dashed-line with open diamonds represents surfaces at coverage of 0.50 ML Octa(1,2), 1.00 ML Octa(1,2) configuration, respectively. The dotted-line with closed triangles, dashed-line with open triangles represents surfaces at coverage of 0.50 ML Octa(2,3), 1.00 ML Octa(2,3) configuration, respectively.

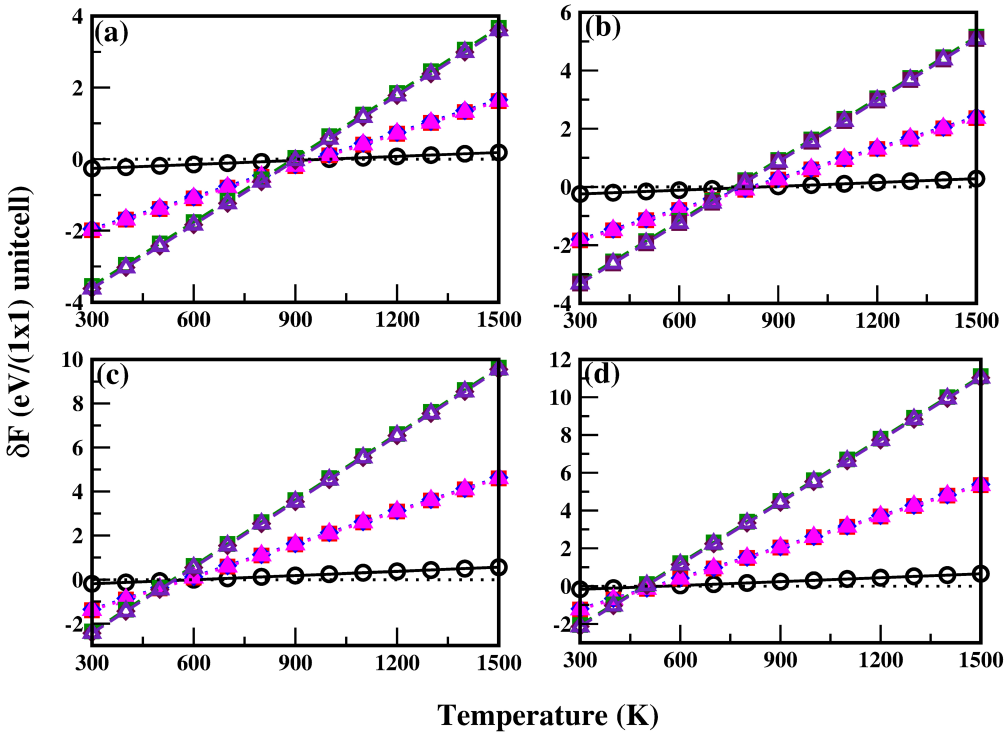


Figure A.10: Free energies relative to that of the surface without adsorbate (ΔF) as a function of temperature at different pressures: (a) 10^{-50}, (b) 10^{-60}, (c) 10^{-90}, and (d) 10^{-100} bar. The dotted-line without any symbol denote the surface without adsorbate. The solid-line with open circles represent surface at oxygen coverage of 0.06 ML. The dotted-line with closed squares, dashed-line with open squares represents surfaces at coverages of 0.50, 1.00 ML, respectively. The dotted-line with closed diamonds, dashed-line with open diamonds represents surfaces at coverage of 0.50 ML Octa(1,2), 1.00 ML Octa(1,2) configuration, respectively. The dotted-line with closed triangles, dashed-line with open triangles represents surfaces at coverage of 0.50 ML Octa(2,3), 1.00 ML Octa(2,3) configuration, respectively.

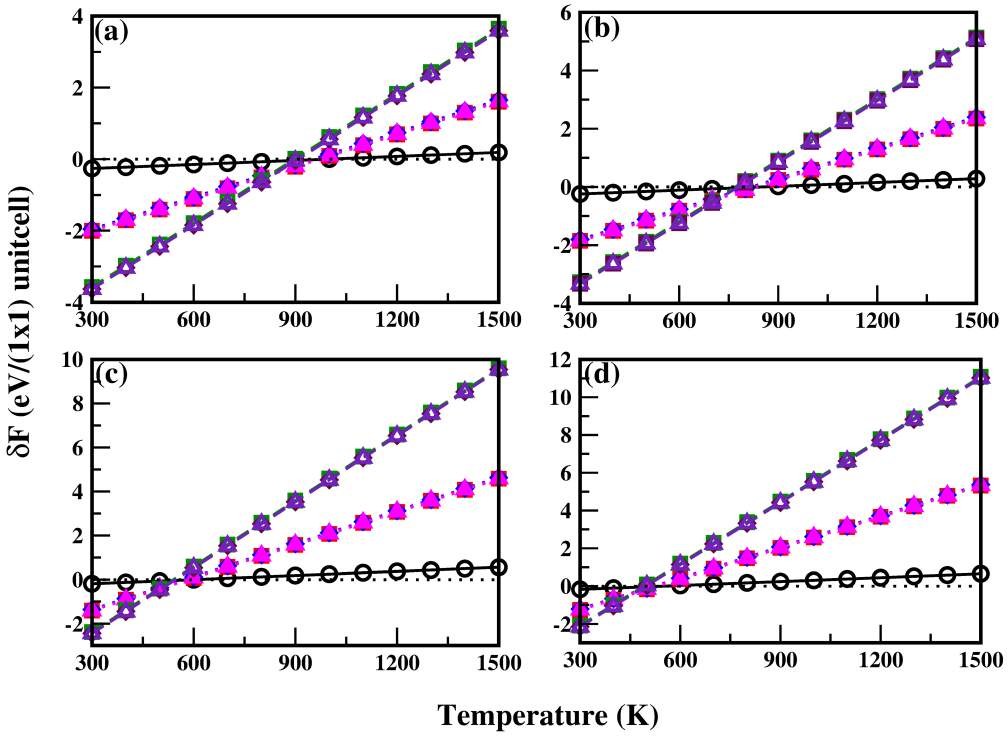


Figure A.11: Free energies relative to that of the surface without adsorbate (ΔF) as a function of temperature at different pressures: (a) 10^{-50}, (b) 10^{-60}, (c) 10^{-90}, and (d) 10^{-100} bar. The dotted-line without any symbol denote the surface without adsorbate. The solid-line with open circles represent surface at oxygen coverage of 0.06 ML. The dotted-line with closed squares, dashed-line with open squares represents surfaces at coverages of 0.50, 1.00 ML, respectively. The dotted-line with closed diamonds, dashed-line with open diamonds represents surfaces at coverage of 0.50 ML Octa(1,2), 1.00 ML Octa(1,2) configuration, respectively. The dotted-line with closed triangles, dashed-line with open triangles represents surfaces at coverage of 0.50 ML Octa(2,3), 1.00 ML Octa(2,3) configuration, respectively.

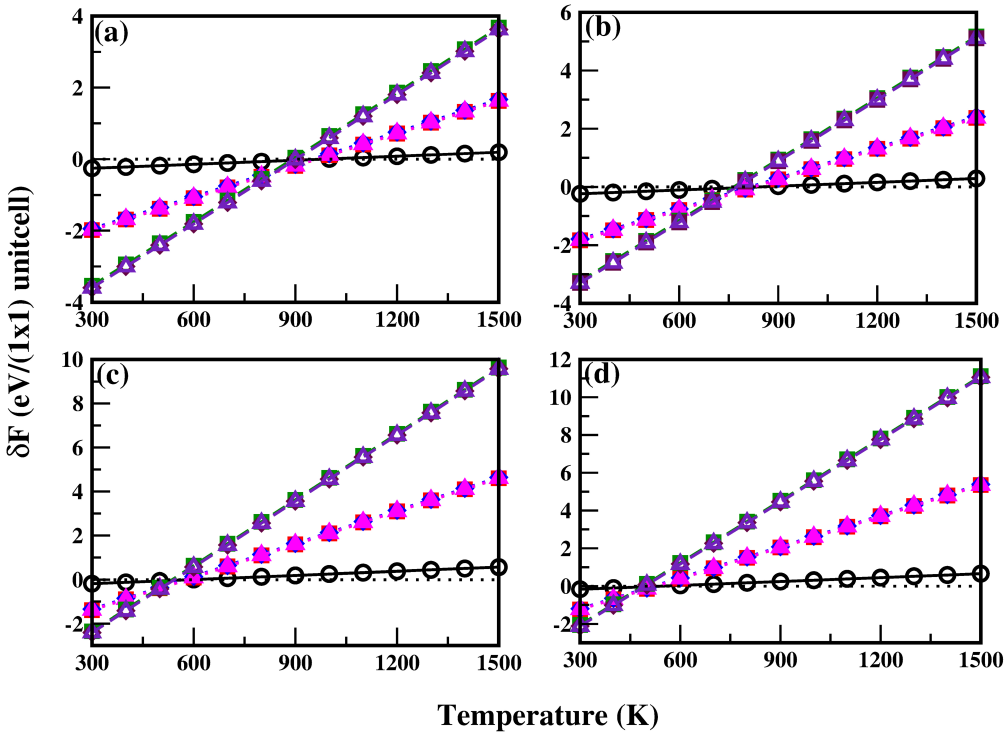


Figure A.12: Free energies relative to that of the surface without adsorbate (ΔF) as a function of temperature at different pressures: (a) 10^{-50}, (b) 10^{-60}, (c) 10^{-90}, and (d) 10^{-100} bar. The dotted-line without any symbol denote the surface without adsorbate. The solid-line with open circles represent surface at oxygen coverage of 0.06 ML. The dotted-line with closed squares, dashed-line with open squares represents surfaces at coverages of 0.50, 1.00 ML, respectively. The dotted-line with closed diamonds, dashed-line with open diamonds represents surfaces at coverage of 0.50 ML Octa(1,2), 1.00 ML Octa(1,2) configuration, respectively. The dotted-line with closed triangles, dashed-line with open triangles represents surfaces at coverage of 0.50 ML Octa(2,3), 1.00 ML Octa(2,3) configuration, respectively.

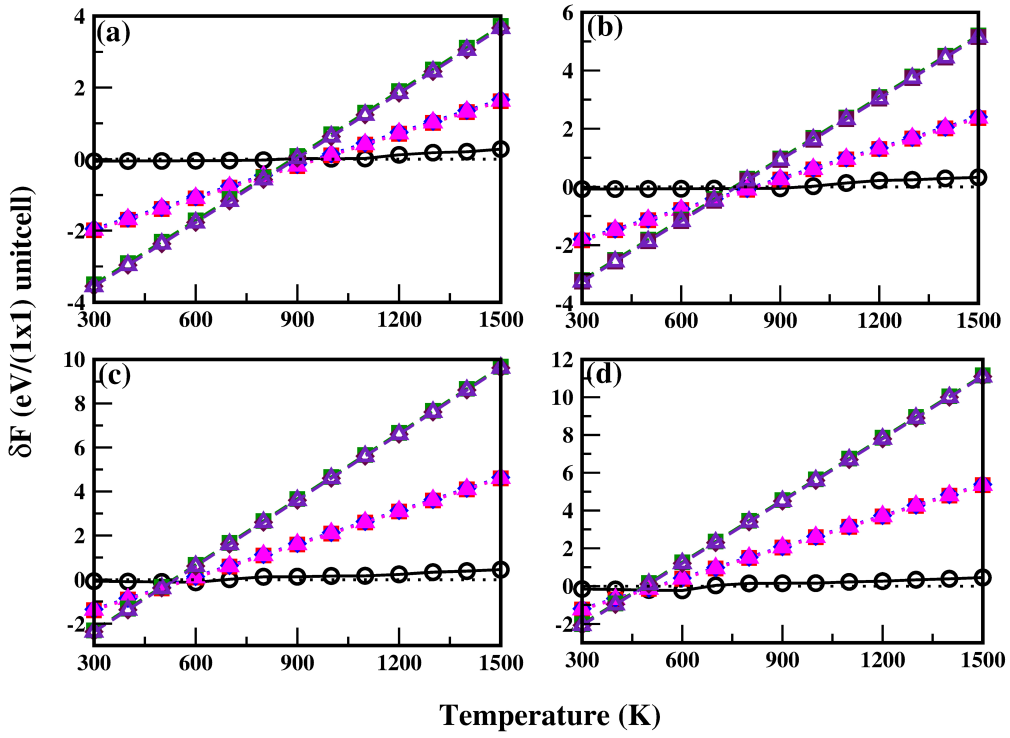


Figure A.13: Free energies relative to that of the surface without adsorbate (ΔF) as a function of temperature at different pressures: (a) 10^{-50}, (b) 10^{-60}, (c) 10^{-90}, and (d) 10^{-100} bar. The dotted-line without any symbol denote the surface without adsorbate. The solid-line with open circles represent surface at oxygen coverage of 0.06 ML. The dotted-line with closed squares, dashed-line with open squares represents surfaces at coverages of 0.50, 1.00 ML, respectively. The dotted-line with closed diamonds, dashed-line with open diamonds represents surfaces at coverage of 0.50 ML Octa(1,2), 1.00 ML Octa(1,2) configuration, respectively. The dotted-line with closed triangles, dashed-line with open triangles represents surfaces at coverage of 0.50 ML Octa(2,3), 1.00 ML Octa(2,3) configuration, respectively.

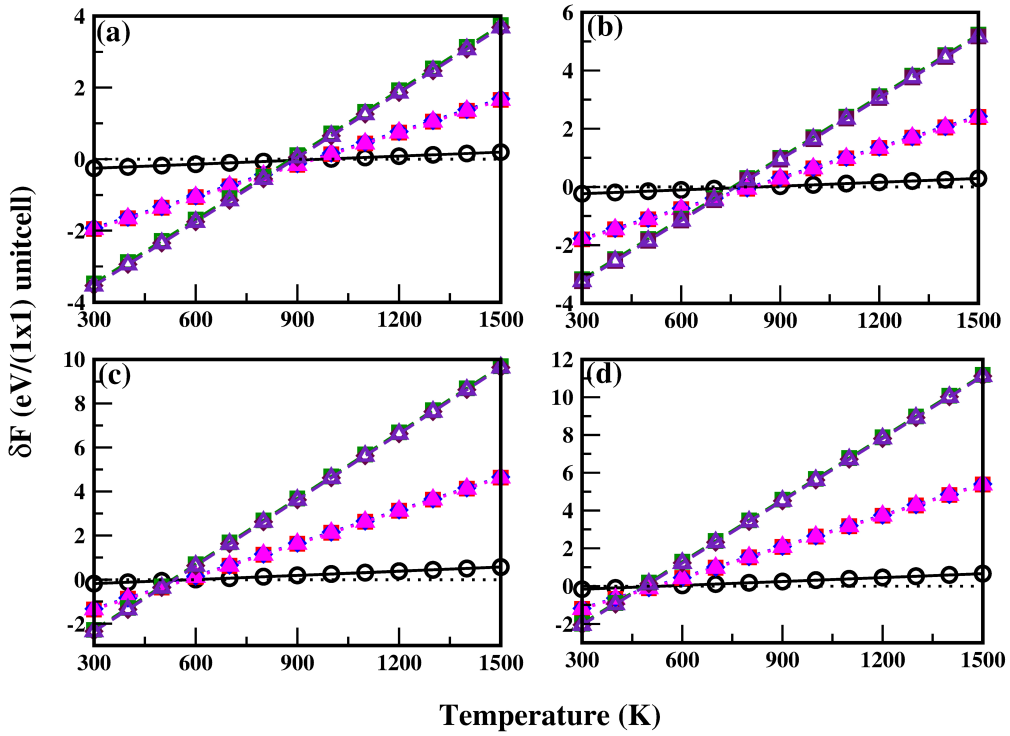


Figure A.14: Free energies relative to that of the surface without adsorbate (ΔF) as a function of temperature at different pressures: (a) 10^{-50}, (b) 10^{-60}, (c) 10^{-90}, and (d) 10^{-100} bar. The dotted-line without any symbol denote the surface without adsorbate. The solid-line with open circles represent surface at oxygen coverage of 0.06 ML. The dotted-line with closed squares, dashed-line with open squares represents surfaces at coverages of 0.50, 1.00 ML, respectively. The dotted-line with closed diamonds, dashed-line with open diamonds represents surfaces at coverage of 0.50 ML Octa(1,2), 1.00 ML Octa(1,2) configuration, respectively. The dotted-line with closed triangles, dashed-line with open triangles represents surfaces at coverage of 0.50 ML Octa(2,3), 1.00 ML Octa(2,3) configuration, respectively.

Ti-Ga(0001)

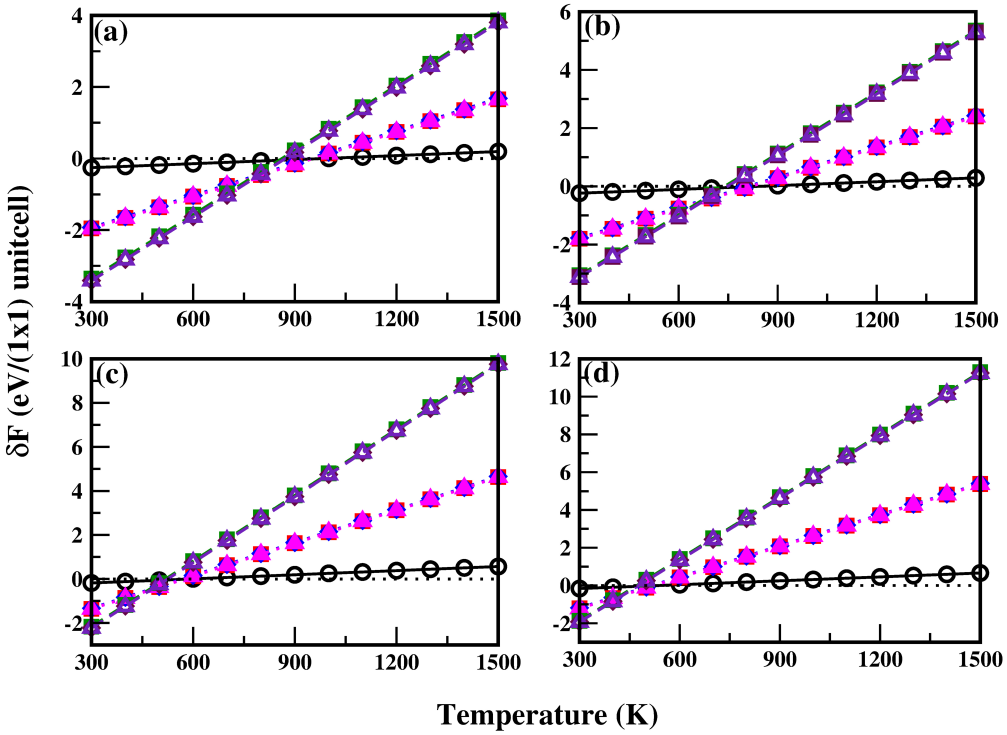


Figure A.15: Free energies relative to that of the surface without adsorbate (ΔF) as a function of temperature at different pressures: (a) 10^{-50}, (b) 10^{-60}, (c) 10^{-90}, and (d) 10^{-100} bar. The dotted-line without any symbol denote the surface without adsorbate. The solid-line with open circles represent surface at oxygen coverage of 0.06 ML. The dotted-line with closed squares, dashed-line with open squares represents surfaces at coverages of 0.50, 1.00 ML, respectively. The dotted-line with closed diamonds, dashed-line with open diamonds represents surfaces at coverage of 0.50 ML Octa(1,2), 1.00 ML Octa(1,2) configuration, respectively. The dotted-line with closed triangles, dashed-line with open triangles represents surfaces at coverage of 0.50 ML Octa(2,3), 1.00 ML Octa(2,3) configuration, respectively.

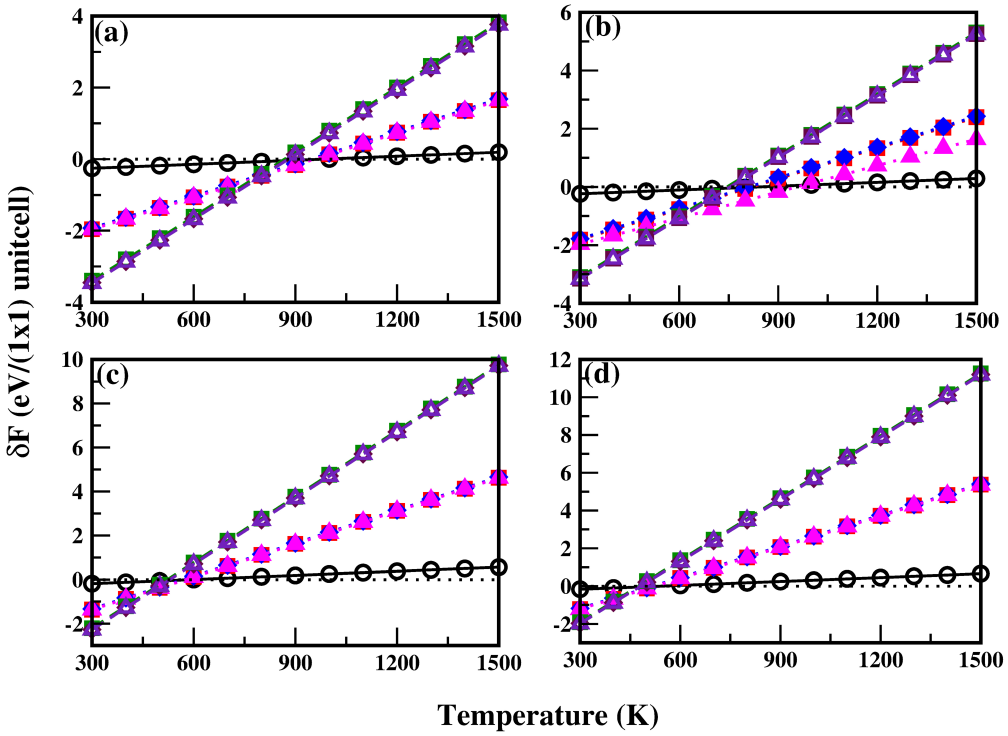


Figure A.16: Free energies relative to that of the surface without adsorbate (ΔF) as a function of temperature at different pressures: (a) 10^{-50}, (b) 10^{-60}, (c) 10^{-90}, and (d) 10^{-100} bar. The dotted-line without any symbol denote the surface without adsorbate. The solid-line with open circles represent surface at oxygen coverage of 0.06 ML. The dotted-line with closed squares, dashed-line with open squares represents surfaces at coverages of 0.50, 1.00 ML, respectively. The dotted-line with closed diamonds, dashed-line with open diamonds represents surfaces at coverage of 0.50 ML Octa(1,2), 1.00 ML Octa(1,2) configuration, respectively. The dotted-line with closed triangles, dashed-line with open triangles represents surfaces at coverage of 0.50 ML Octa(2,3), 1.00 ML Octa(2,3) configuration, respectively.

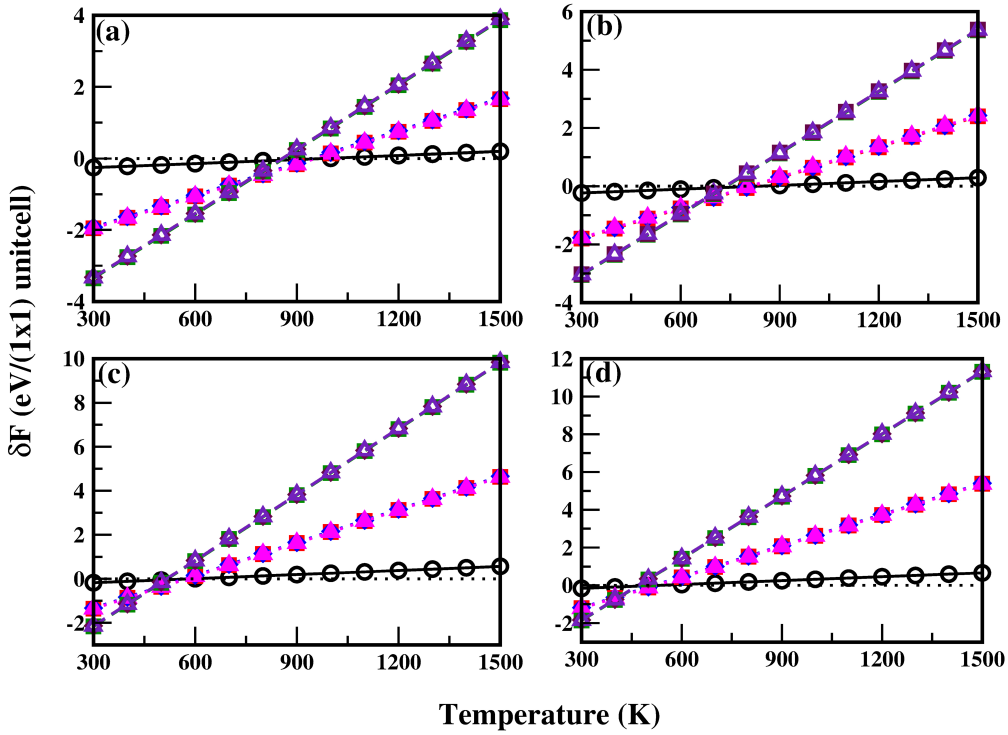
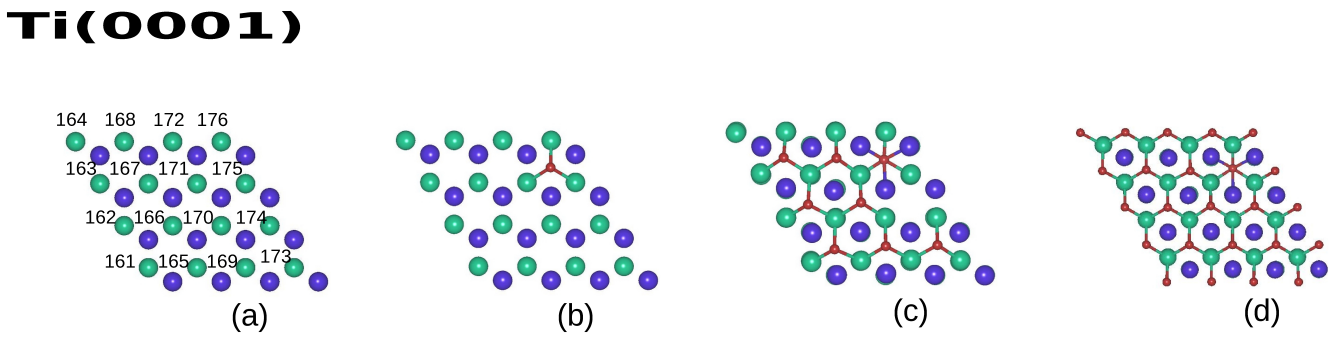
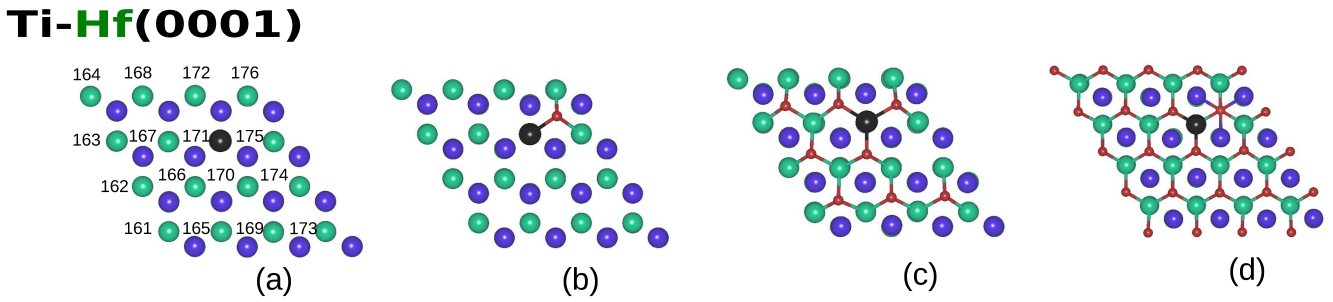


Figure A.17: Free energies relative to that of the surface without adsorbate (ΔF) as a function of temperature at different pressures: (a) 10^{-50}, (b) 10^{-60}, (c) 10^{-90}, and (d) 10^{-100} bar. The dotted-line without any symbol denote the surface without adsorbate. The solid-line with open circles represent surface at oxygen coverage of 0.06 ML. The dotted-line with closed squares, dashed-line with open squares represents surfaces at coverages of 0.50, 1.00 ML, respectively. The dotted-line with closed diamonds, dashed-line with open diamonds represents surfaces at coverage of 0.50 ML Octa(1,2), 1.00 ML Octa(1,2) configuration, respectively. The dotted-line with closed triangles, dashed-line with open triangles represents surfaces at coverage of 0.50 ML Octa(2,3), 1.00 ML Octa(2,3) configuration, respectively.



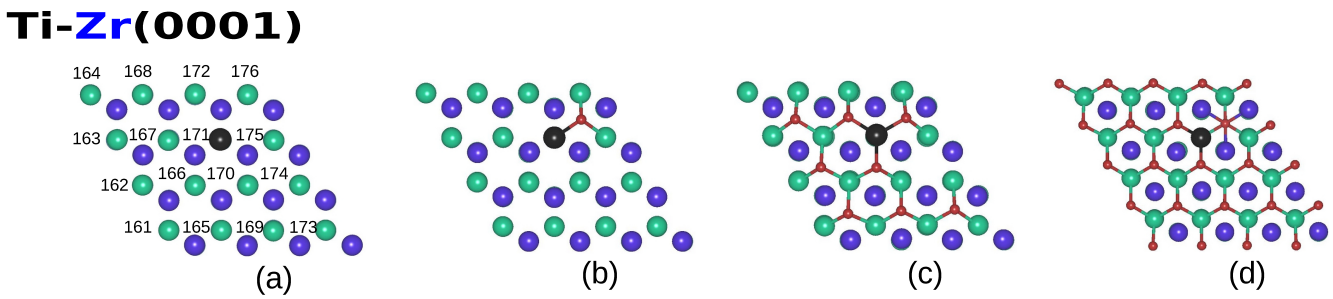
Atom No.	(a)	(b)	(c)	(d)	Atom No.	(a)	(b)	(c)	(d)
161	-0.14	-0.18	+0.40	+1.22	169	-0.14	-0.13	+0.91	+1.25
162	-0.14	-0.11	+0.28	+1.32	170	-0.14	-0.19	+0.85	+1.38
163	-0.14	-0.16	+0.43	+1.22	171	-0.14	+0.48	+0.79	+0.66
164	-0.14	-0.19	-0.26	+1.39	172	-0.14	-0.19	+0.24	+1.39
165	-0.14	-0.14	+0.88	+1.24	173	-0.14	-0.18	+0.31	+1.22
166	-0.14	-0.18	+1.36	+1.23	174	-0.14	-0.17	+0.35	+1.22
167	-0.14	-0.18	+1.37	+1.23	175	-0.14	+0.47	-0.32	+0.66
168	-0.14	-0.14	+0.19	+1.24	176	-0.14	+0.47	-0.31	+0.68

Figure A.18: Charges on the surface Ti atoms at (a) Θ_O = 0.00 ML, (b) Θ_O = 0.06 ML, (c) Θ_O = 0.50 ML Octa(2,3), and (d) Θ_O = 1.00 ML Octa(2,3).



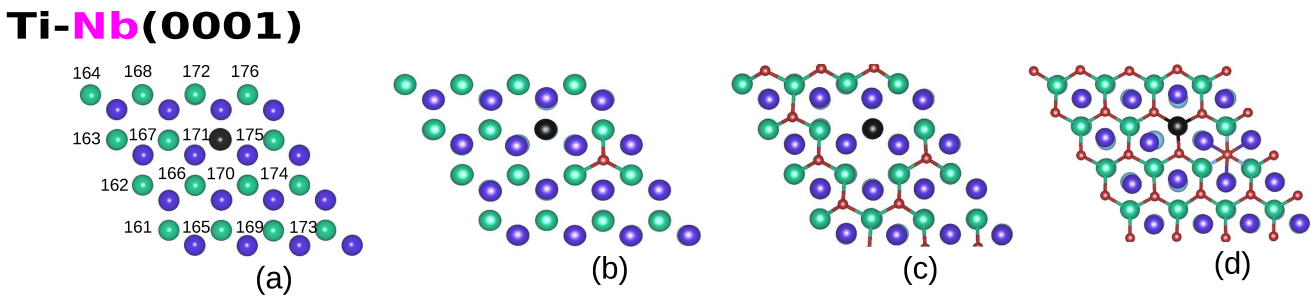
Atom No.	(a)	(b)	(c)	(d)	Atom No.	(a)	(b)	(c)	(d)
161	-0.11	-0.18	+0.39	+1.20	169	-0.11	-0.06	+0.90	+1.21
162	-0.10	-0.04	+0.29	+1.31	170	-0.09	-0.12	+0.79	+1.38
163	-0.10	-0.17	+0.24	+1.21	171[Hf]	-0.17	+0.46	+1.66	+0.67
164	-0.05	-0.16	-0.20	+1.41	172	-0.09	-0.13	+0.20	+1.38
165	-0.07	-0.002	+0.88	+1.24	173	-0.09	-0.16	+0.38	+1.21
166	-0.09	-0.26	+1.31	+1.24	174	-0.09	-0.16	+0.40	+1.21
167	-0.10	-0.27	+1.28	+1.23	175	-0.09	+0.44	+0.27	+0.67
168	-0.06	-0.004	+0.23	+1.23	176	-0.10	+0.45	+0.10	+0.68

Figure A.19: Charges on the surface Ti and Hf atoms at (a) Θ_O = 0.00 ML, (b) Θ_O = 0.06 ML, (c) Θ_O = 0.50 ML , and (d) Θ_O = 1.00 ML Octa(2,3).



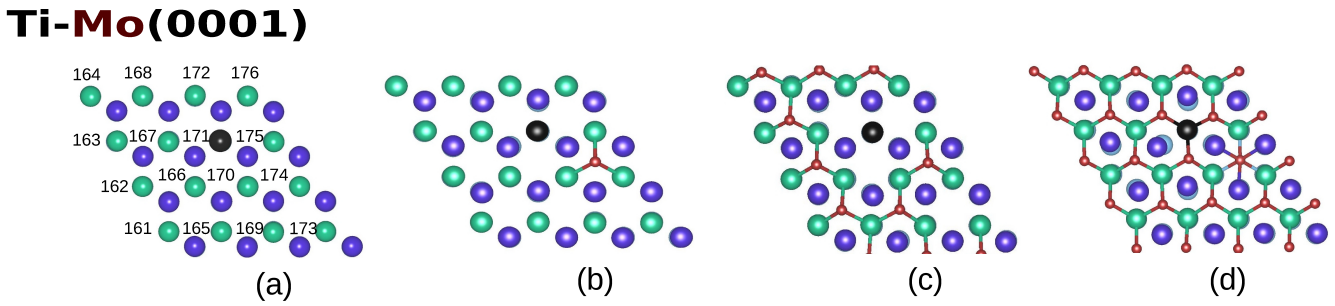
Atom No.	(a)	(b)	(c)	(d)	Atom No.	(a)	(b)	(c)	(d)
161	-0.13	-0.18	+0.38	+1.21	169	-0.13	-0.09	+0.90	+1.22
162	-0.11	-0.03	+0.30	+1.28	170	-0.14	-0.14	+0.80	+1.37
163	-0.13	-0.19	+0.22	+1.21	171[Zr]	+0.02	+0.54	+1.58	+0.60
164	+0.02	-0.17	-0.20	+1.41	172	-0.13	-0.14	+0.21	+1.37
165	+0.02	-0.03	+0.89	+1.22	173	-0.11	-0.18	+0.38	+1.21
166	-0.14	-0.33	+1.30	+1.28	174	-0.11	-0.17	+0.41	+1.21
167	-0.13	-0.33	+1.29	+1.28	175	-0.14	+0.44	+0.26	+0.71
168	-0.00	-0.013	+0.22	+1.21	176	-0.14	+0.45	+0.10	+0.71

Figure A.20: Charges on the surface Ti and Zr atoms at (a) Θ_O = 0.00 ML, (b) Θ_O = 0.06 ML, (c) Θ_O = 0.50 ML , and (d) Θ_O = 1.00 ML Octa(2,3).



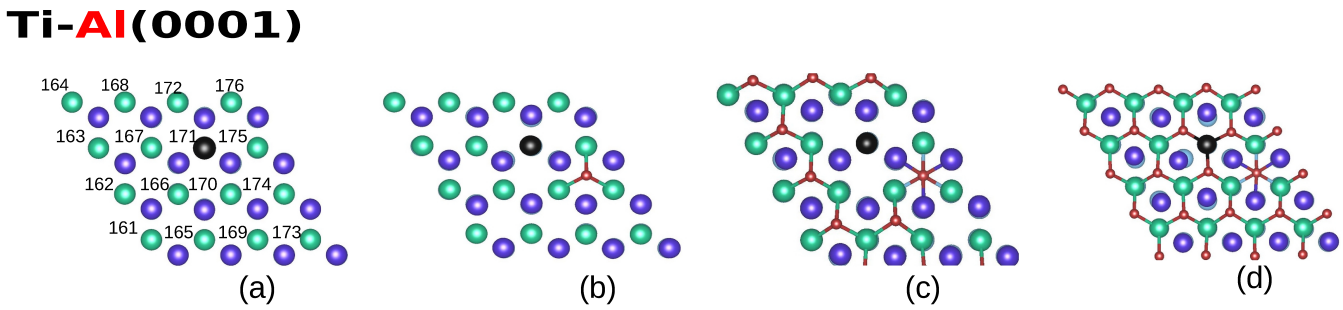
Atom No.	(a)	(b)	(c)	(d)	Atom No.	(a)	(b)	(c)	(d)
161	+0.00	-0.02	+0.31	+1.34	169	-0.00	-0.18	+0.77	+1.39
162	-0.12	-0.24	+0.33	+1.11	170	+0.14	+0.61	+0.94	+0.88
163	-0.00	-0.18	+0.31	+1.37	171[Nb]	-1.37	-1.32	-1.33	-0.10
164	-0.11	-0.16	+0.05	+1.20	172	+0.14	-0.14	+0.94	+1.32
165	-0.11	-0.16	+1.36	+1.08	173	-0.12	-0.24	+0.36	+1.17
166	+0.14	-0.02	+0.89	+1.43	174	-0.11	+0.44	+0.36	+0.64
167	+0.14	-0.14	+0.89	+1.37	175	+0.14	+0.61	+0.57	+0.87
168	-0.13	-0.17	+1.36	+1.28	176	+0.14	-0.02	+0.57	+1.43

Figure A.21: Charges on the surface Ti and Nb toms at (a) Θ_O = 0.00 ML, (b) Θ_O = 0.06 ML, (c) Θ_O = 0.50 ML , and (d) Θ_O = 1.00 ML Octa(2,3).



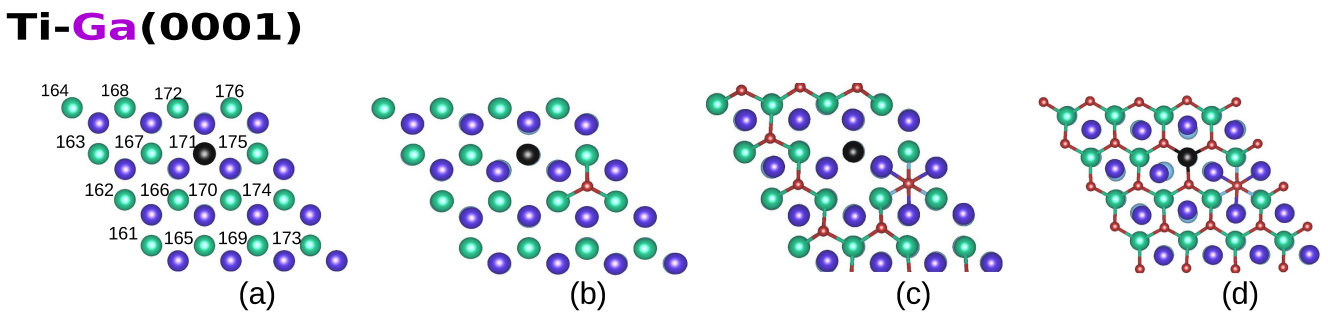
Atom No.	(a)	(a)	(b)	(c)	Atom No.	(a)	(a)	(b)	(c)
161	+0.05	-0.01	+0.34	+1.35	169	+0.04	-0.17	+0.76	+1.39
162	-0.26	-0.43	+0.35	+1.13	170	+0.21	+0.66	+0.99	+0.89
163	+0.04	-0.17	+0.33	+1.39	171[Mo]	-1.85	-1.85	-1.76	-0.62
164	-0.13	-0.15	+0.11	+1.14	172	+0.23	-0.25	+0.99	+1.39
165	-0.13	-0.15	+1.36	+1.14	173	-0.23	-0.43	+0.29	+1.14
166	+0.22	-0.08	+0.90	+1.45	174	-0.22	+0.37	+0.31	+0.65
167	+0.22	-0.25	+0.89	+1.39	175	+0.22	+0.67	+0.62	+0.87
168	-0.13	-0.19	+1.36	+1.24	176	+0.22	-0.08	+0.61	+1.45

Figure A.22: Charges on the surface Mo atoms at (a) Θ_O = 0.00 ML, (b) Θ_O = 0.06 ML, (c) Θ_O = 0.50 ML , and (d) Θ_O = 1.00 ML Octa(2,3).



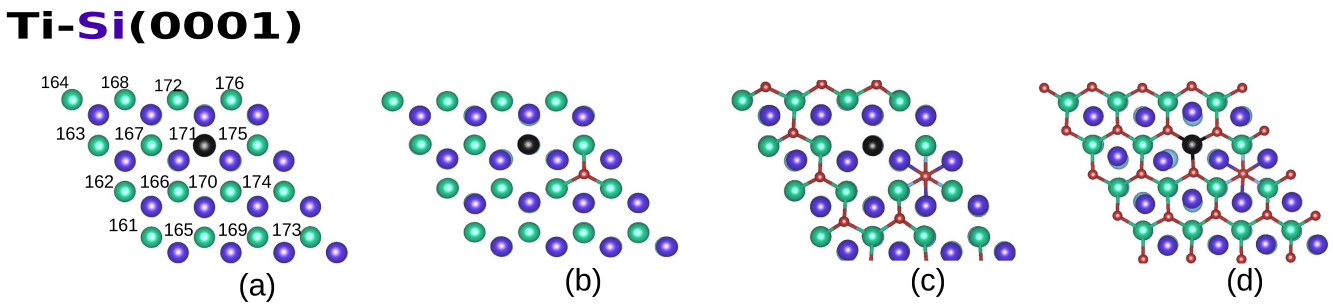
Atom No.	(a)	(b)	(c)	(d)	Atom No.	(a)	(b)	(c)	(d)
161	-0.23	-0.22	+0.25	+1.25	169	-0.22	-0.26	+0.79	+1.38
162	-0.22	-0.30	+0.43	+1.22	170	-0.14	+0.55	+0.30	+0.68
163	-0.22	-0.26	+0.33	+1.39	171[Al]	-0.89	-0.91	-1.10	+1.73
164	-0.04	-0.28	+0.31	+1.20	172	-0.13	-0.13	+0.98	+1.26
165	-0.05	-0.28	+1.38	+1.20	173	-0.22	-0.29	+0.20	+1.22
166	-0.14	-0.24	+0.95	+1.38	174	-0.23	+0.36	-0.44	+0.64
167	-0.14	-0.16	+0.91	+1.26	175	-0.14	+0.55	-0.30	+0.65
168	-0.04	-0.17	+1.30	+1.15	176	-0.15	-0.24	+0.44	+1.38

Figure A.23: Charges on the surface Ti and Al atoms at (a) Θ_O = 0.00 ML, (b) Θ_O = 0.06 ML, (c) Θ_O = 0.50 ML Octa(2,3) , and (d) Θ_O = 1.00 ML Octa(2,3).



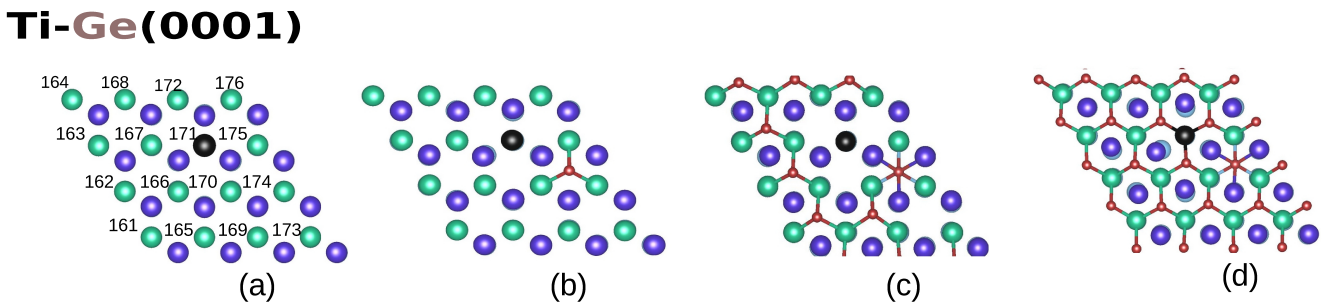
Atom No.	(a)	(b)	(c)	(d)	Atom No.	(a)	(b)	(c)	(d)
161	-0.16	-0.15	+0.27	+1.25	169	-0.15	-0.21	+0.77	+1.38
162	-0.13	-0.23	+0.42	+1.19	170	-0.05	+0.57	+0.35	+0.72
163	-0.15	-0.21	+0.33	+1.38	171[Ga]	-1.13	-1.14	-1.31	+0.73
164	-0.09	-0.19	+0.33	+1.19	172	-0.06	-0.09	+0.99	+1.31
165	-0.09	-0.19	+1.37	+1.18	173	-0.13	-0.24	+0.19	+1.19
166	-0.05	-0.18	+0.95	+1.41	174	-0.13	+0.32	-0.39	+0.70
167	-0.04	-0.10	+0.92	+1.32	175	-0.05	+0.57	-0.24	+0.71
168	-0.11	-0.13	+1.30	+1.14	176	-0.05	-0.17	+0.48	+1.41

Figure A.24: Charges on the surface Ti and Ga atoms at (a) Θ_O = 0.00 ML, (b) Θ_O = 0.06 ML, (c) Θ_O = 0.50 ML Octa(2,3) , and (d) Θ_O = 1.00 ML Octa(2,3).



Atom No.	(a)	(b)	(c)	(d)	Atom No.	(a)	(b)	(c)	(d)
161	-0.20	-0.18	+0.29	+1.21	169	-0.19	-0.25	+0.78	+1.34
162	-0.14	-0.18	+0.44	+1.28	170	-0.01	+0.60	+0.41	+0.65
163	-0.19	-0.25	+0.32	+1.34	171[Si]	-1.58	-1.57	-1.72	+1.94
164	+0.00	-0.18	+0.32	+1.20	172	+0.02	-0.02	+1.00	+1.19
165	+0.00	-0.18	+1.35	+1.21	173	-0.14	-0.18	+0.18	+1.28
166	-0.01	-0.09	+0.98	+1.31	174	-0.14	+0.39	-0.40	+0.64
167	-0.01	-0.02	+0.93	+1.17	175	-0.01	+0.59	-0.16	+0.64
168	-0.02	-0.09	+1.30	+1.21	176	+0.00	-0.08	+0.51	+1.31

Figure A.25: Charges on the surface Ti and Si atoms at (a) Θ_O = 0.00 ML, (b) Θ_O = 0.06 ML, (c) Θ_O = 0.50 ML Octa(2,3) , and (d) Θ_O = 1.00 ML Octa(2,3).



Atom No.	(a)	(b)	(c)	(d)	Atom No.	(a)	(b)	(c)	(d)
161	-0.18	-0.16	+0.30	+1.22	169	-0.18	-0.21	+0.83	+1.34
162	-0.15	-0.22	+0.32	+1.33	170	-0.02	+0.59	-0.12	+0.67
163	-0.18	-0.22	+0.38	+1.33	171[Ge]	-1.35	-1.38	-1.52	+1.97
164	-0.09	-0.17	+0.22	+1.21	172	-0.02	-0.01	+1.07	+1.38
165	-0.09	-0.16	+1.38	+1.32	173	-0.15	-0.22	+1.38	+1.28
166	-0.01	-0.09	+0.98	+1.33	174	-0.14	+0.34	+0.86	+0.67
167	-0.01	-0.01	+0.93	+1.20	175	-0.02	+0.59	+0.55	+0.67
168	-0.10	-0.12	+1.32	+1.23	176	-0.01	-0.09	+0.39	+1.38

Figure A.26: Charges on the surface Ti and Ge atoms at (a) Θ_O = 0.00 ML, (b) Θ_O = 0.06 ML, (c) Θ_O = 0.50 ML Octa(2,3) , and (d) Θ_O = 1.00 ML Octa(2,3).

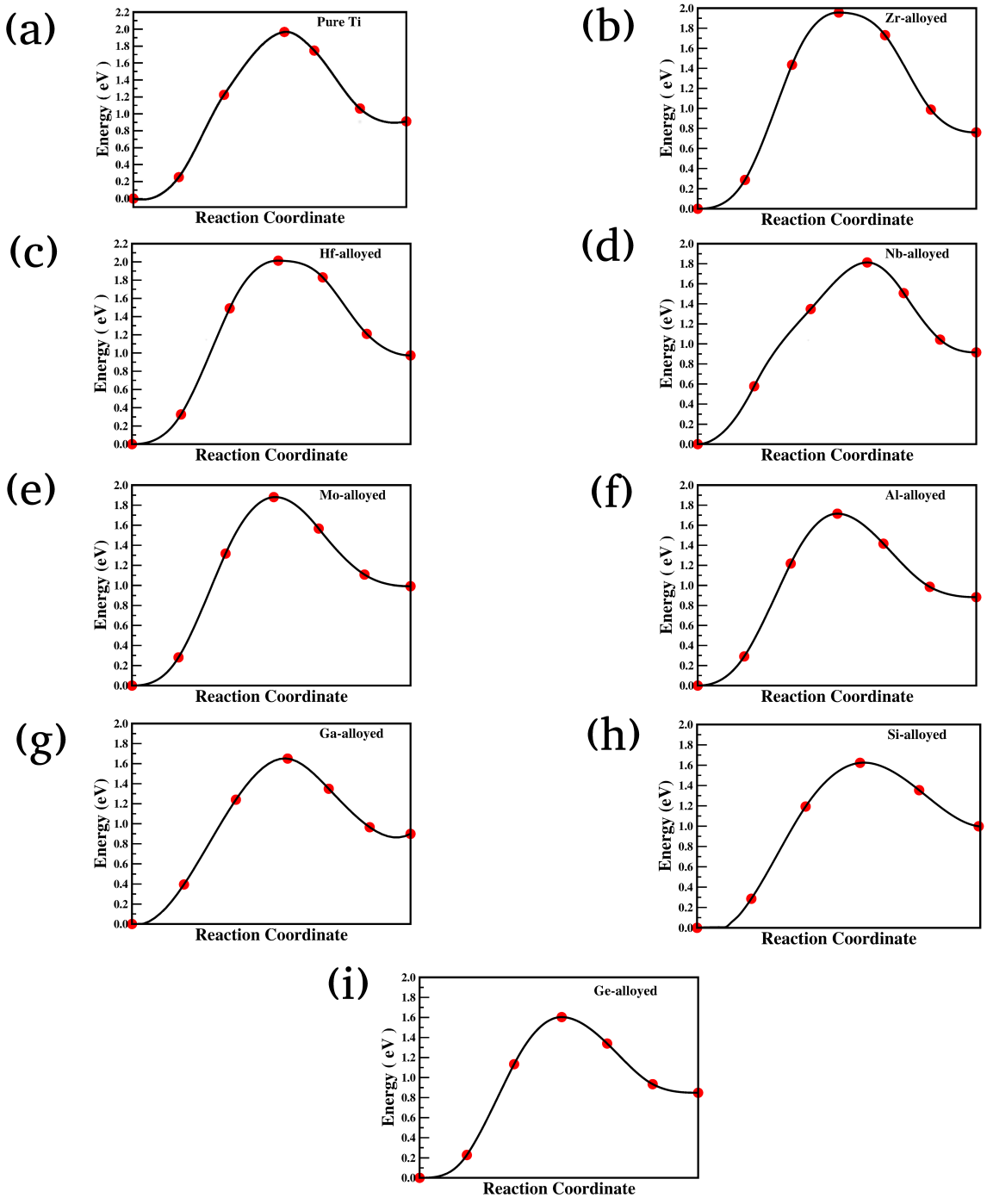


Figure A.27: The energy profile for surface to sub-surface oxygen diffusion at oxygen coverage of 0.06 ML on pure Ti (a) and alloyed Ti (b), (c), (d), (e), (f), (g), (h), (i) are when the alloying elements are Zr, Hf, Nb, Mo, Al, Ga, Si and Ge respectively.

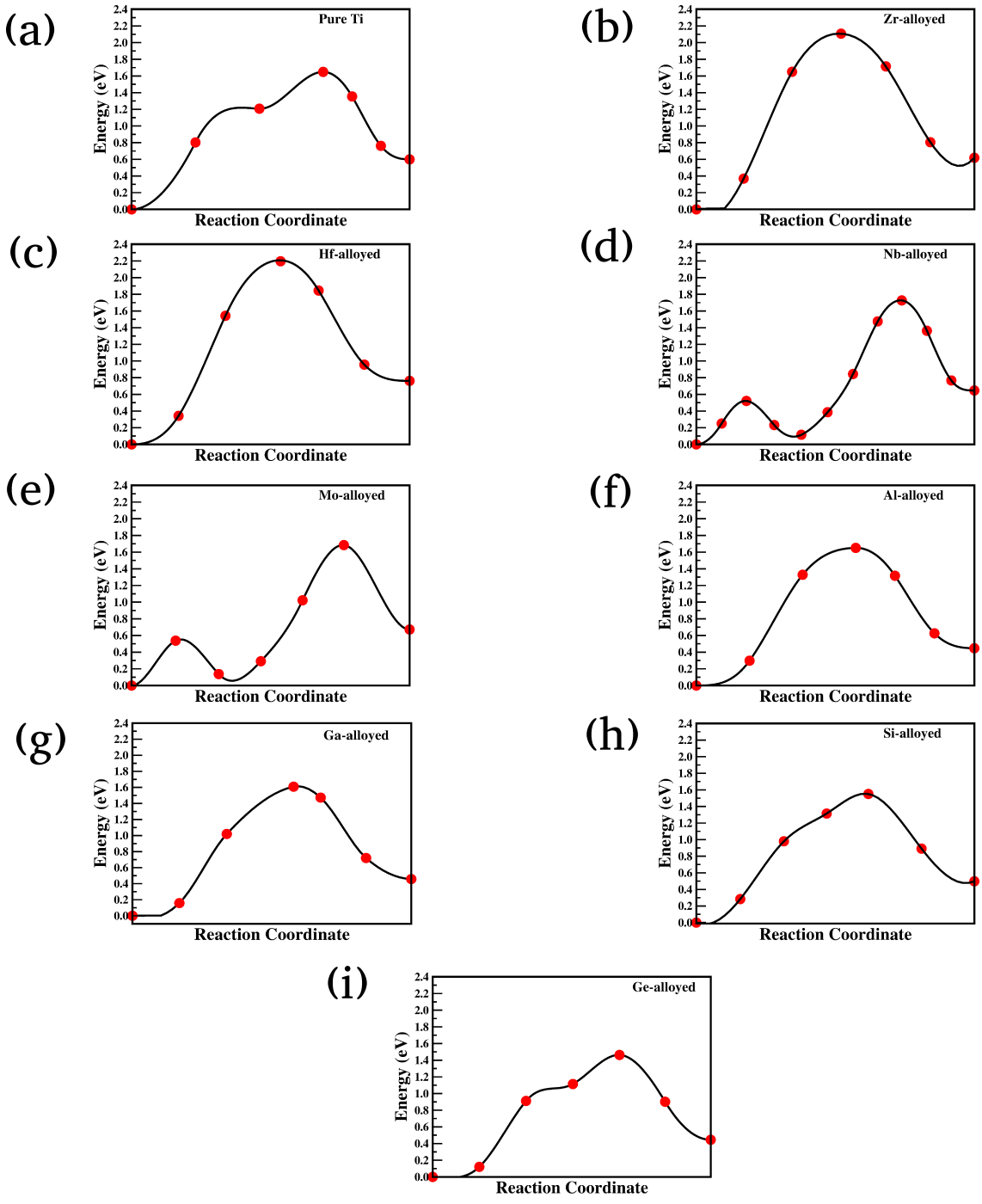


Figure A.28: The energy profile for surface to sub-surface oxygen diffusion at oxygen coverage of 0.5 ML on pure Ti (a) and alloyed Ti (b), (c), (d), (e), (f), (g), (h), (i) are when the alloying elements are Zr, Hf, Nb, Mo, Al, Ga, Si and Ge respectively.

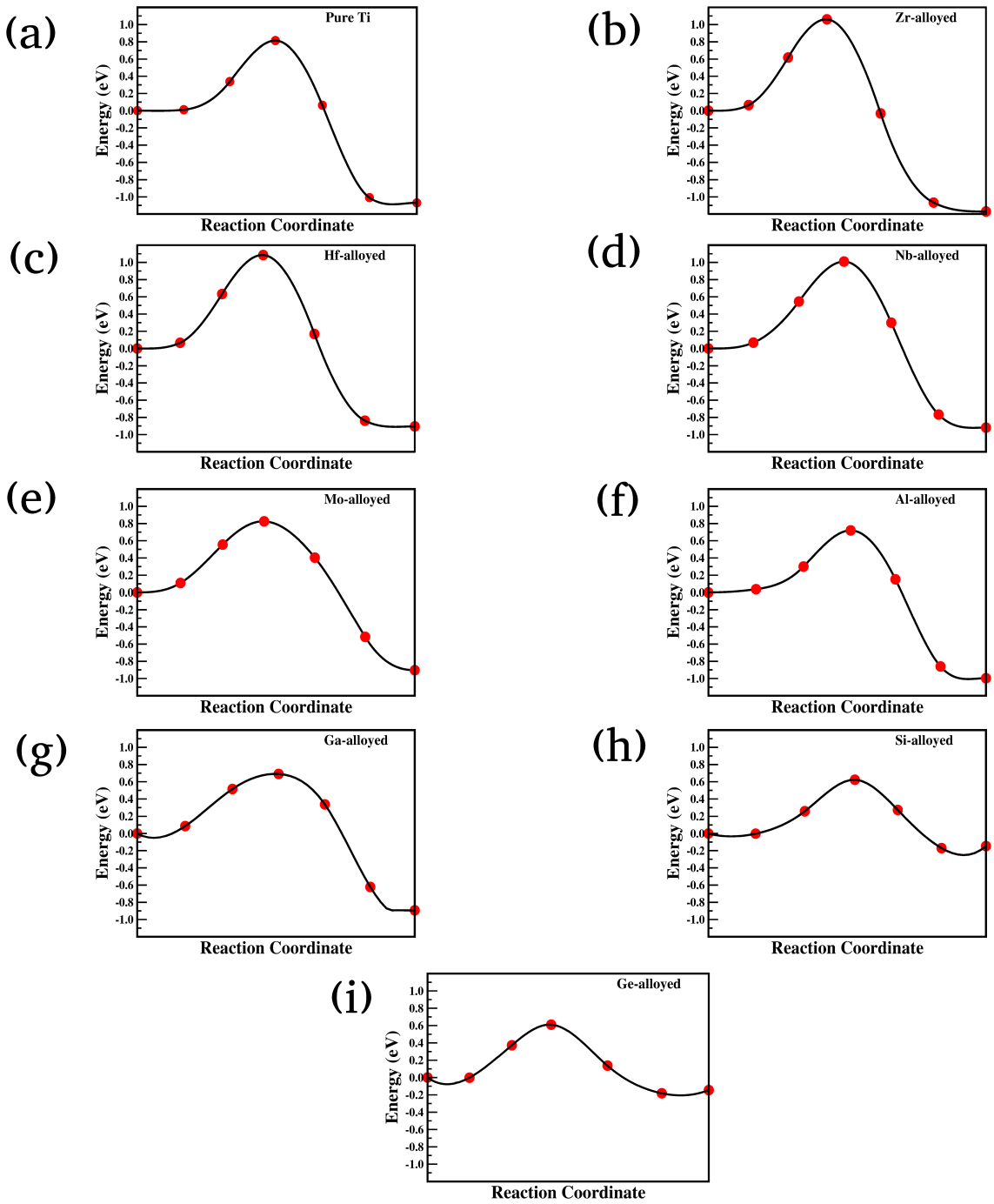


Figure A.29: The energy profile for surface to sub-surface oxygen diffusion at oxygen coverage of 1.00 ML on pure Ti (a) and alloyed Ti (b), (c), (d), (e), (f), (g), (h), (i) are when the alloying elements are Zr, Hf, Nb, Mo, Al, Ga, Si and Ge respectively.

Appendix B

Appendix B

B.1 Adsorption of sulphur-containing species

The Table B.1, B.2 and B.3 below tabulates adsorption energies and optimized structural parameters of H_2S, SH and S at sites other than the most stable ones. Figure B.1 below shows the three inequivalent configurations with 0.33 ML S coverage. Figure B.2 below shows the variation of adsorption energy of sulphur(E^{S}_{ads}) with distance between two sulphur atoms(d_{S-S}). Figure B.3 below shows the four inequivalent configurations with 0.50 ML S coverage.

Table B.1: The adsorption energies and optimized structural parameters of H_2S on PdCu(110) surface.

Adsorption Site	$\mathbf{E}_{ads}$ **(eV)**	$\mathbf{E}^{ZP}_{ads}$ **(eV)**	$\mathbf{d}_{Pd-S/Cu-S}$ **(Å)**	$\mathbf{d}_{S-H}$ **(Å)**	$\angle HSH$^o
T2	-0.43	-0.40	2.34	1.37	92.0
B1	-0.52	-0.50	2.38	1.44	91.0
B2	-0.66	-0.64	2.34	1.36	91.4
B3	-0.48	-0.44	2.37/2.35	1.41	91.3
H1	-0.66	-0.64	2.38/2.34	1.36	91.4
H2	-0.49	-0.46	2.38/2.35	1.41	92.3

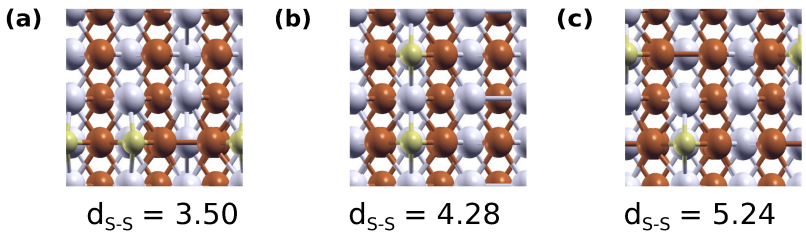


Figure B.1: The inequivalent configurations of S adsorbed on the surface at Θ_S = 0.33 ML. The numbers below are the shortest distances between two S atoms and are in Å.

Table B.2: The adsorption energies and optimized structural parameters of SH on PdCu(110) surface.

Adsorption Site	E_{ads} (eV)	E_{ads}^{ZP} (eV)	$d_{Pd-S/Cu-S}$ (Å)	d_{S-H} (Å)
B1	-2.87	-2.85	2.38/2.23	1.48
B3	-2.99	-2.96	2.35/2.26	1.37
H1	-3.07	-3.05	2.48/2.28	1.42
H2	-3.09	-3.05	2.47/2.22	1.37
T1	-2.87	-2.84	2.39	1.49
T2	-3.09	-3.05	2.23	1.37

Table B.3: The adsorption energies and optimized structural parameters of S on PdCu(110) surface.

Adsorption Site	E_{ads} (eV)	$d_{Pd-S/Cu-S}$ (Å)
B1	-2.42	2.42/2.27
B3	-2.41	2.47/2.22
H1	-2.42	2.42/2.27
H2	-2.52	2.41/2.21
T1	-0.80	2.40
T2	-1.10	2.20

B.2 H_2S dissociation

Figure B.4 below shows the energy profile for reaction steps R1 and R2 of H_2S dissociation reaction.

B.3 Coadsorbed H_2 and H_2S dissociation

B.3.1 H_2 and H_2S coadsorption

Figure B.5 below shows the different configurations of coadsorbed H_2 and H_2S as a combination of T1 and T2 sites.

B.3.2 Dissociation of H_2 and H_2S in coadsorbed form

Figure B.6 and B.7 below shows the energy profile for the three reaction steps R1, R2, and R3 for P1 and P2 in case of coadsorbed dissociation reaction.

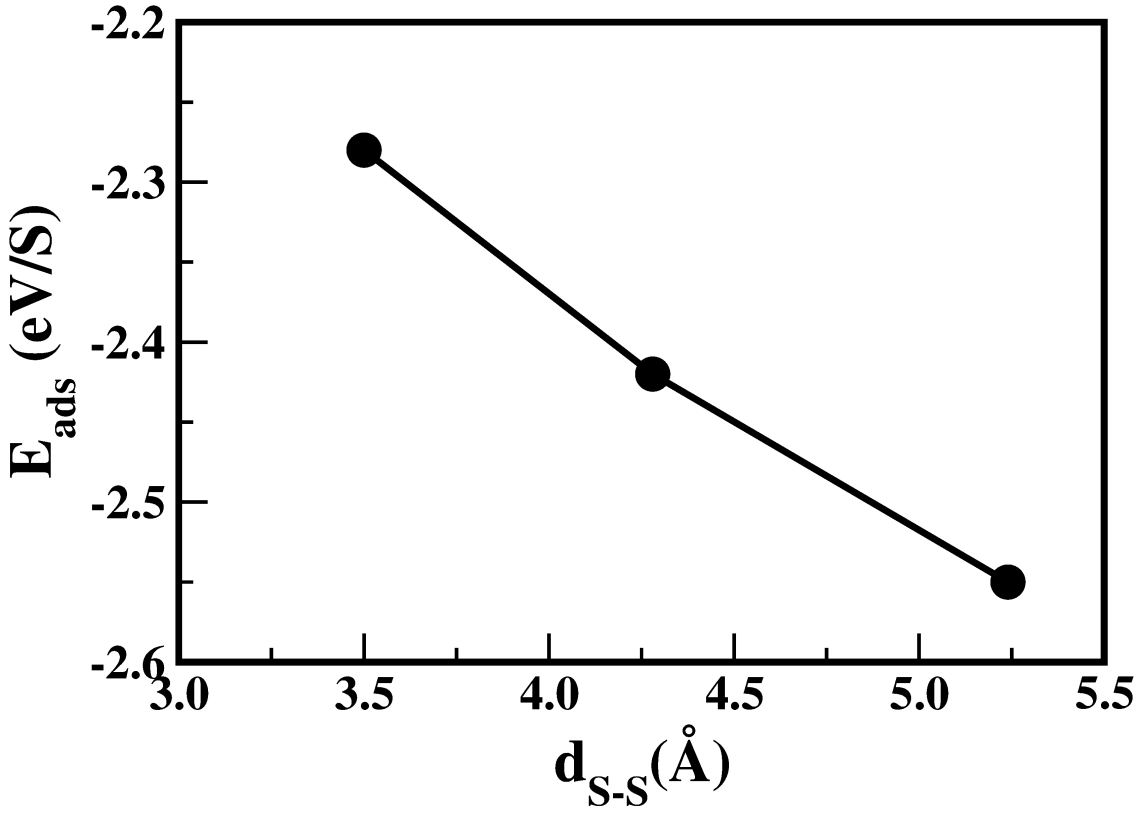


Figure B.2: Adsorption energy of sulphur(E_{ads}) versus distance between two sulphur atoms(d_{S-S}) in Å.

B.4 Effect of S poisoning

B.4.0.1 Coadsorption of atomic S and H at $\Theta_{H,S}$ = 0.16 ML

The various configurations with S and H coadsorbed, with different S-H distances are shown below in Figure B.8

B.4.0.2 Effect of S poisoning on H adsorption

Figure B.9 below shows the lowest energy configurations for different combination of Θ_S and Θ_H.

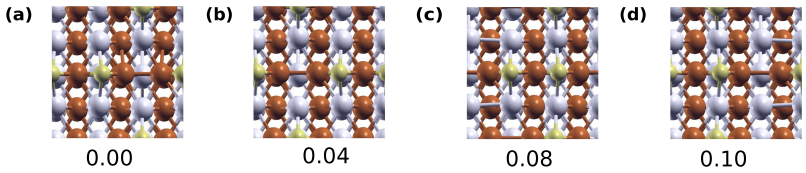


Figure B.3: The inequivalent configurations of S adsorbed on the surface at Θ_S = 0.50 ML arranged in decreasing order of stability. The numbers below are the relative energies in eV.

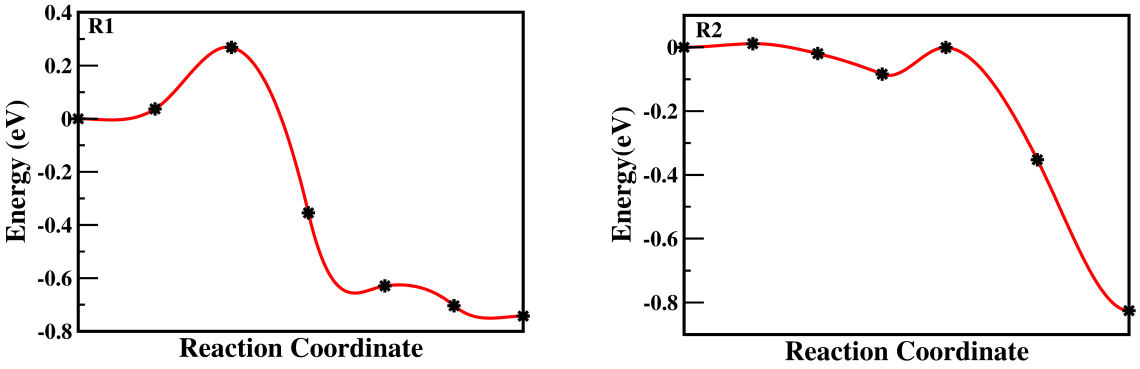


Figure B.4: The energy profile of H_2S dissociation reaction.

B.4.0.3 Effect of Sulphur poisoning on the H_2 dissociation at higher H coverage ($1.00 \leq \Theta_H \leq 1.50$ ML)

Figure B.10 below shows the initial and final for H_2 dissociation pathway at different H, S coverage. Figure B.11 below shows the dissociation pathways at different H, S coverages.

B.4.0.4 Effect of Sulphur poisoning on surface to sub-surface diffusion at Θ_H = 1.16 and 1.50 ML

Figure B.12 below shows the initial and final states considered for the penetration step at H coverages of 1.16 and 1.50 ML. Figure B.13 below shows the energy profiles for the penetration of H at different H, S coverage.



Figure B.5: The different configurations of coadsorbed H_2 and H_2S.

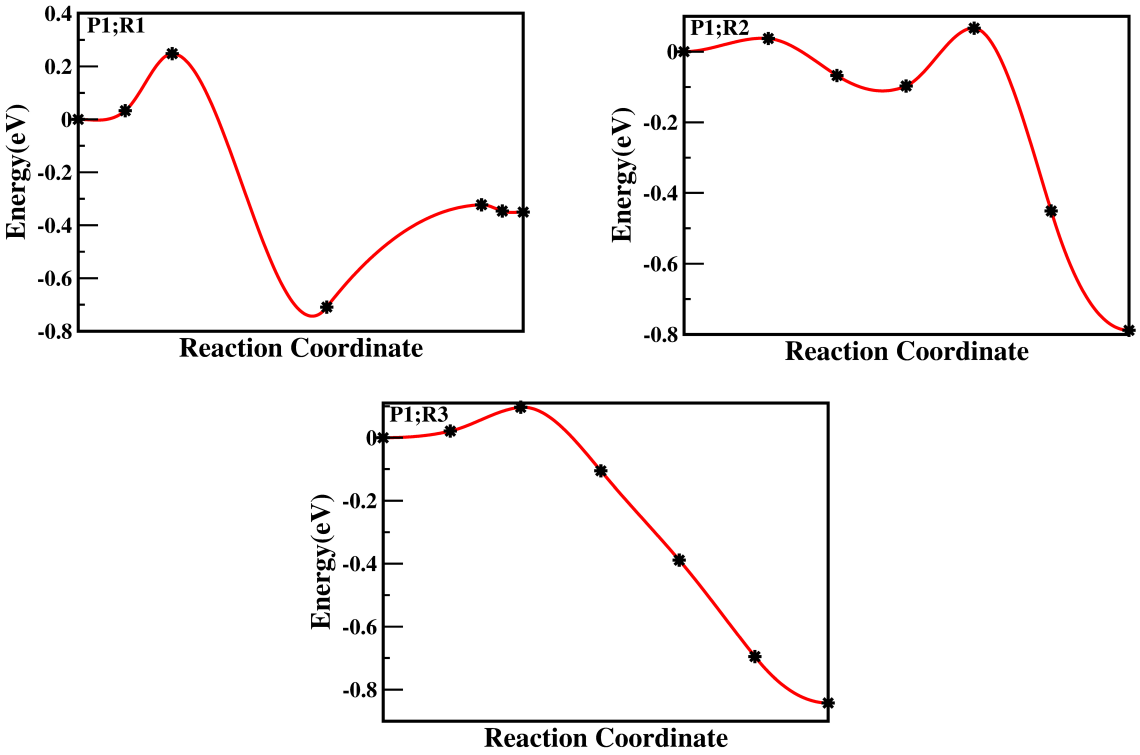


Figure B.6: The energy profile of coadsorbed dissociation reaction for P1.

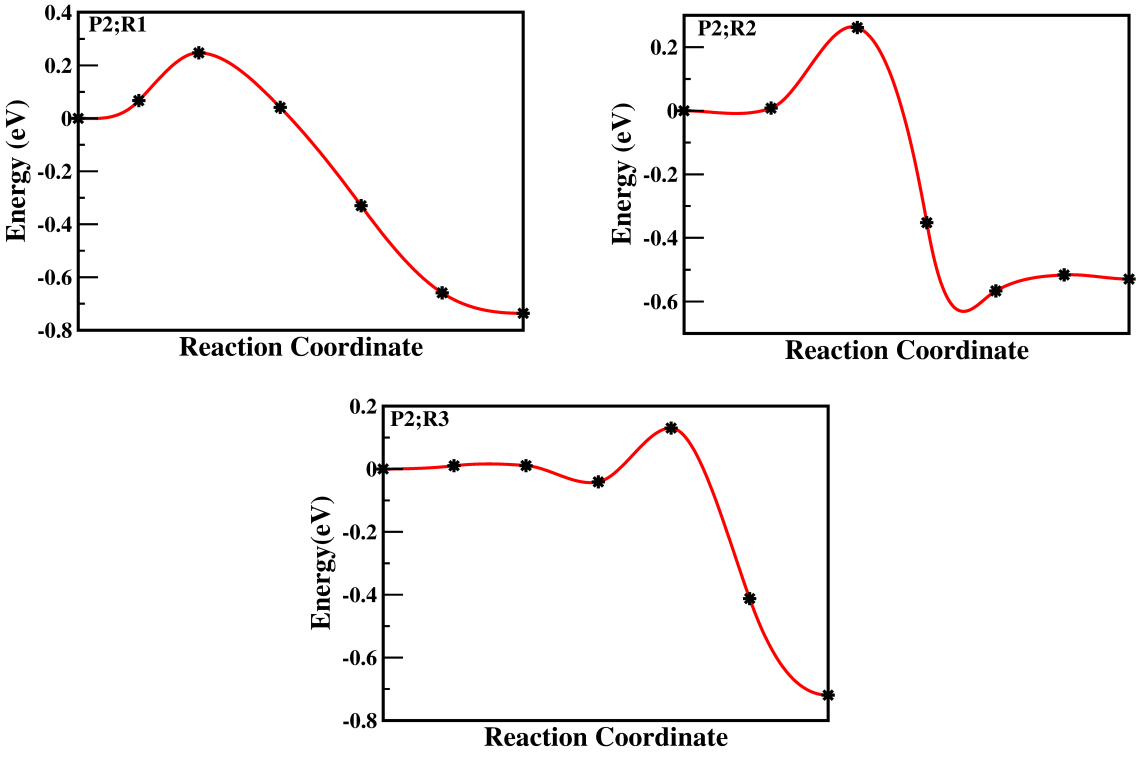


Figure B.7: The energy profile of coadsorbed dissociation reaction for P2.

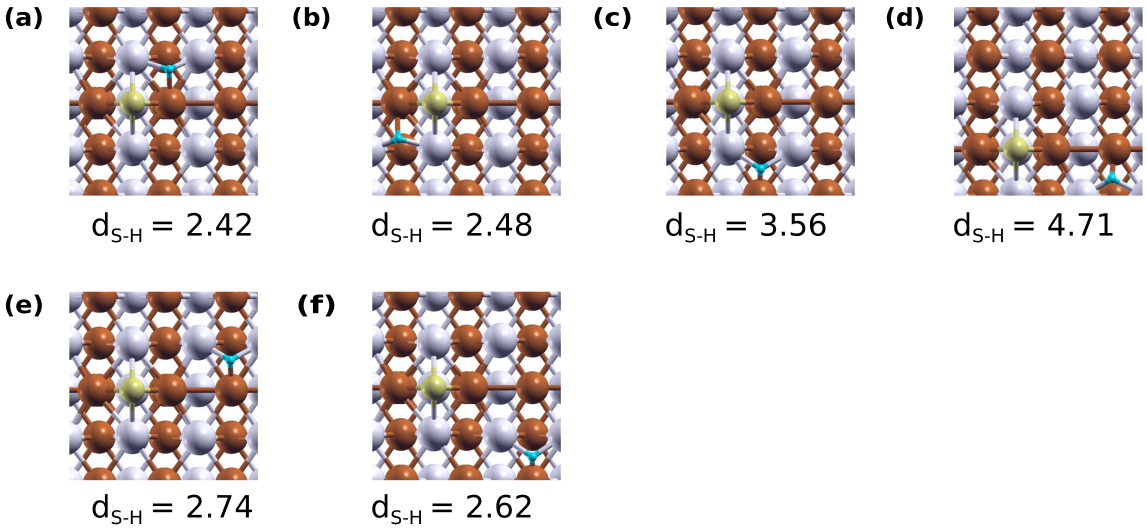


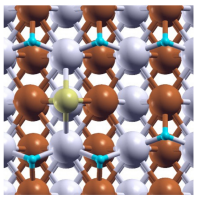
Figure B.8: The configurations with S and H coadsorbed on the surface. The numbers below are the distances between S and H atoms in Å.

Table B.4: The Zero-point energy corrections involved in different processes on PdCu(110) surface.

Process	**E**$_{ads}$ (eV)	**E**$^{ZP}_{ads}$ (eV)	**E**$_{act}$ **(eV)**	**E**$^{ZP}_{act}$ **(eV)**
Adsorption				
H_2S at T1 site	-0.66	-0.64		
SH at B2 site	-3.16	-3.11		
H_2S dissociation				
R1			0.27	0.24
R2			0.08	0.06
H_2 and H_2S co-adsorption				
H_2 and H_2S at T1 site	-0.97	-0.94		
H_2 and H_2S co-adsorbed dissociation				
P1;R1			0.29	0.27
P1;R2			0.06	0.04
P1;R3			0.13	0.10
P2;R1			0.30	0.26
P2;R2			0.04	0.01
P2;R3			0.27	0.25
S and H co-adsorption (d_{H-S} = 3.56 Å)	-0.57	-0.54		

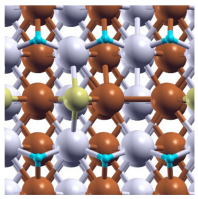
θ_H = 1.00 ML and θ_S = 0.16 ML

(a)



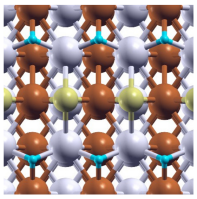
θ_H = 1.00 ML and θ_S = 0.33 ML

(a)



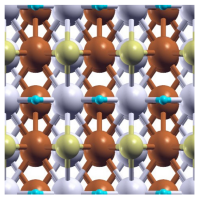
θ_H = 1.00 ML and θ_S = 0.50 ML

(a)



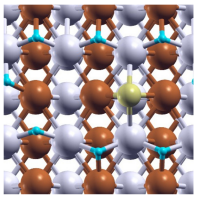
θ_H = 1.00 ML and θ_S = 1.00 ML

(a)



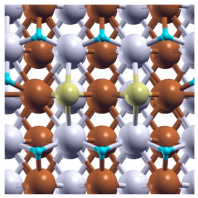
θ_H = 1.16 ML and θ_S = 0.16 ML

(a)



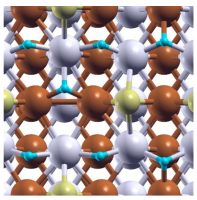
θ_H = 1.16 ML and θ_S = 0.33 ML

(a)



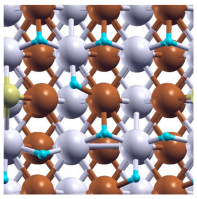
θ_H = 1.16 ML and θ_S = 0.50 ML

(a)



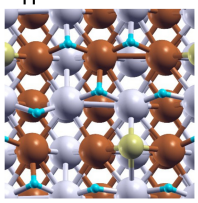
θ_H = 1.50 ML and θ_S = 0.16 ML

(a)



θ_H = 1.50 ML and θ_S = 0.33 ML

(a)



θ_H = 1.50 ML and θ_S = 0.50 ML

(a)

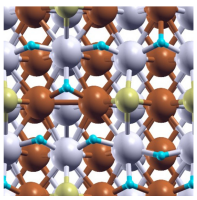


Figure B.9: Configurations for different combination of Θ_H and Θ_S .

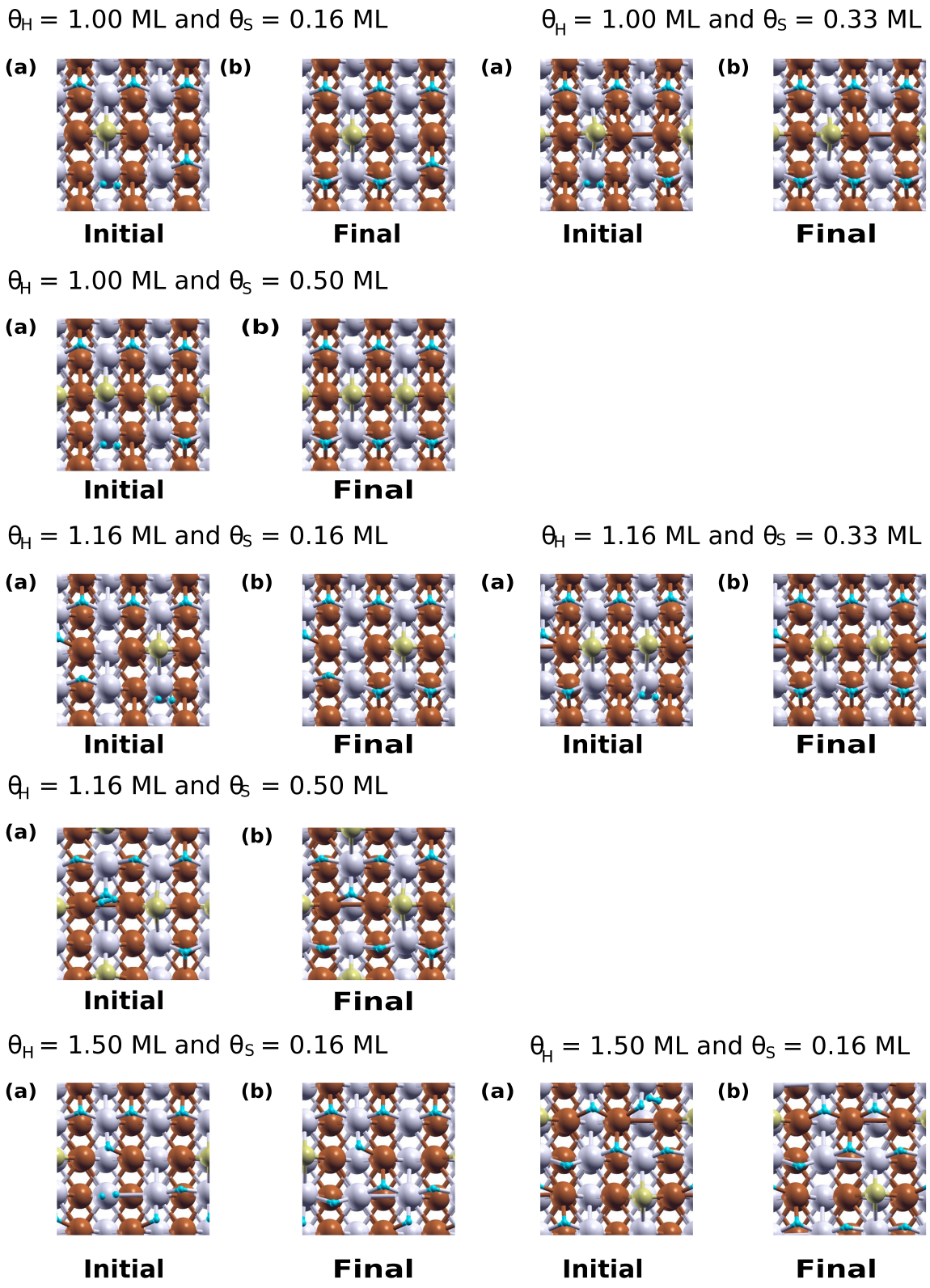


Figure B.10: The initial and final state configurations for H_2 dissociation pathway for all coverages of H and S atoms.

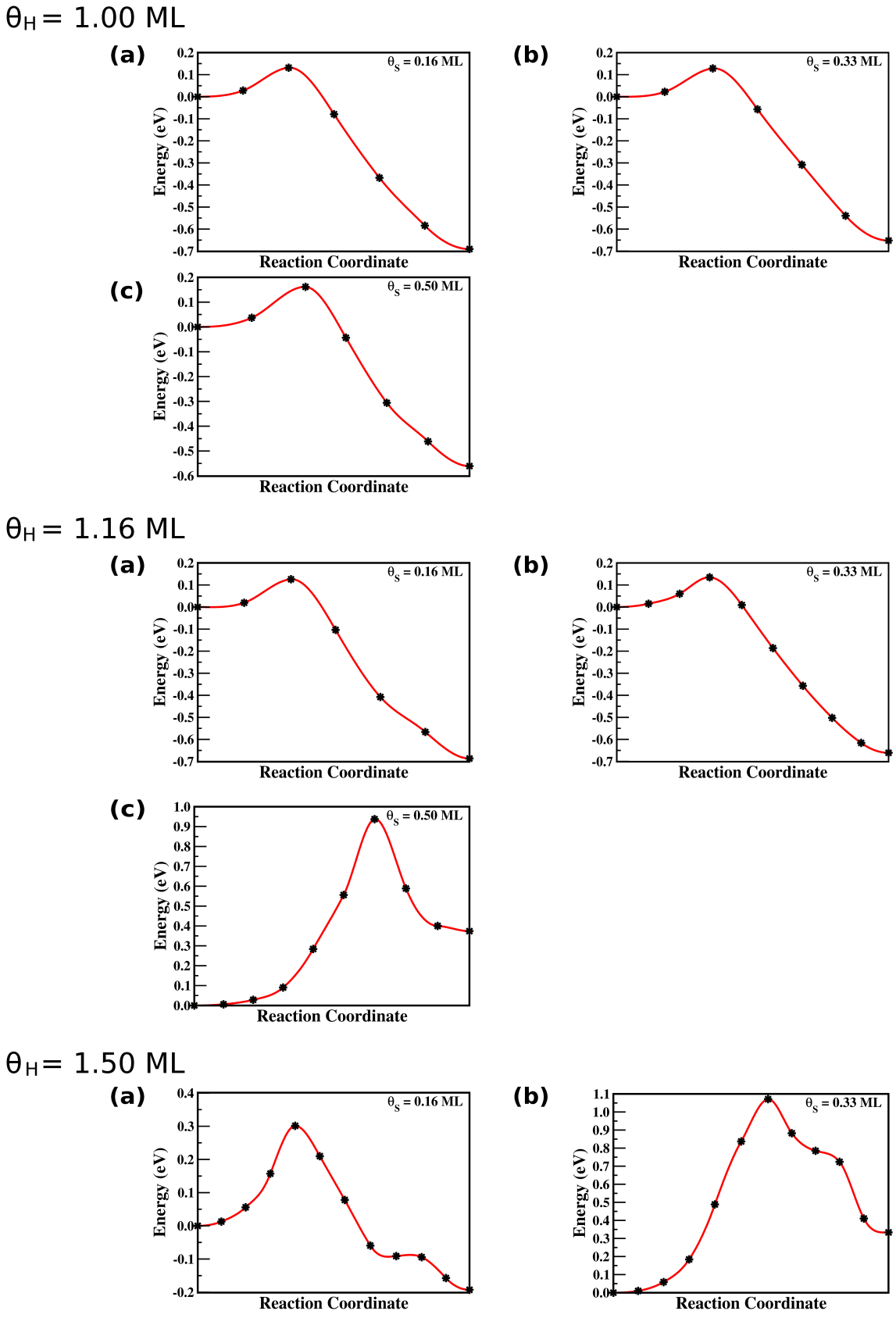


Figure B.11: The energy profile for H_2 dissociation pathway at different H, S coverage.

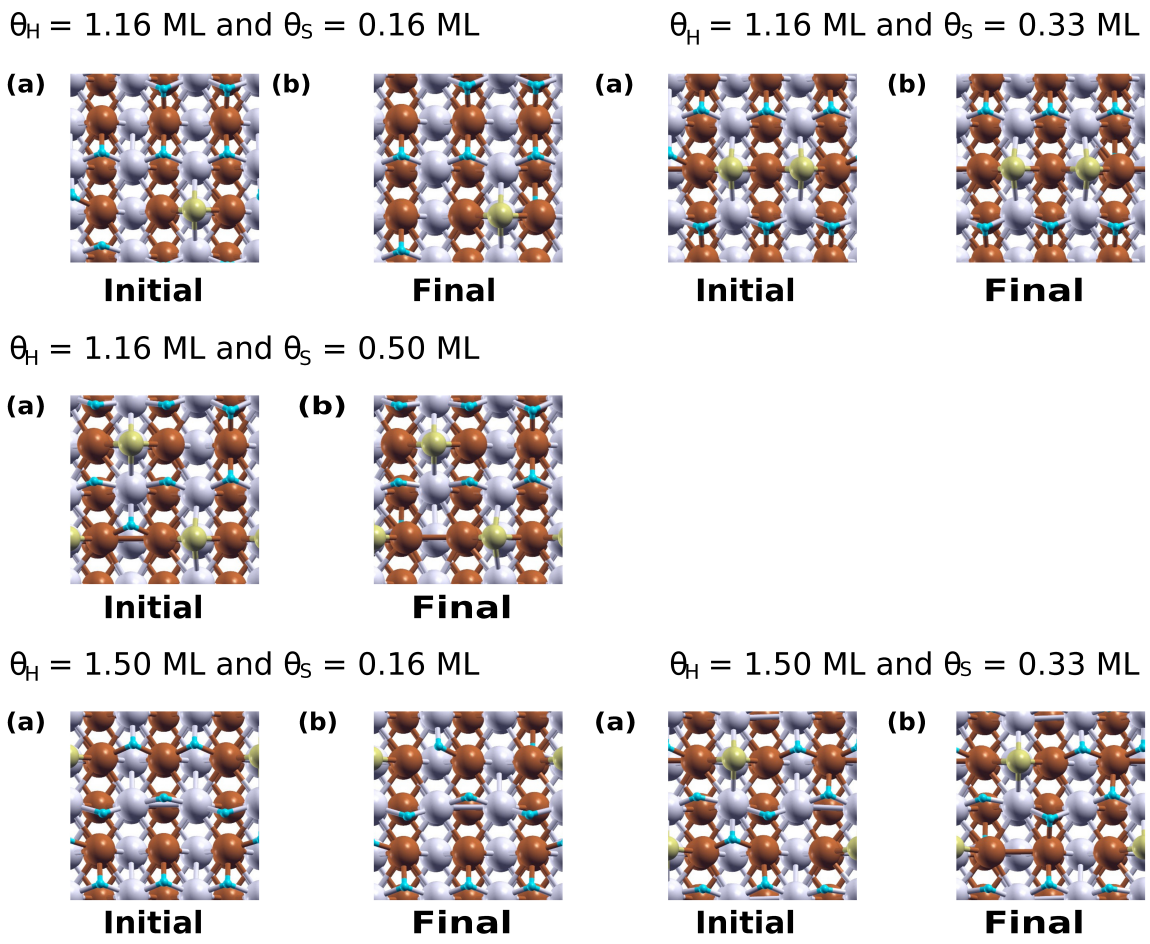


Figure B.12: The initial and final state configurations for H penetration step at different H, S coverage.

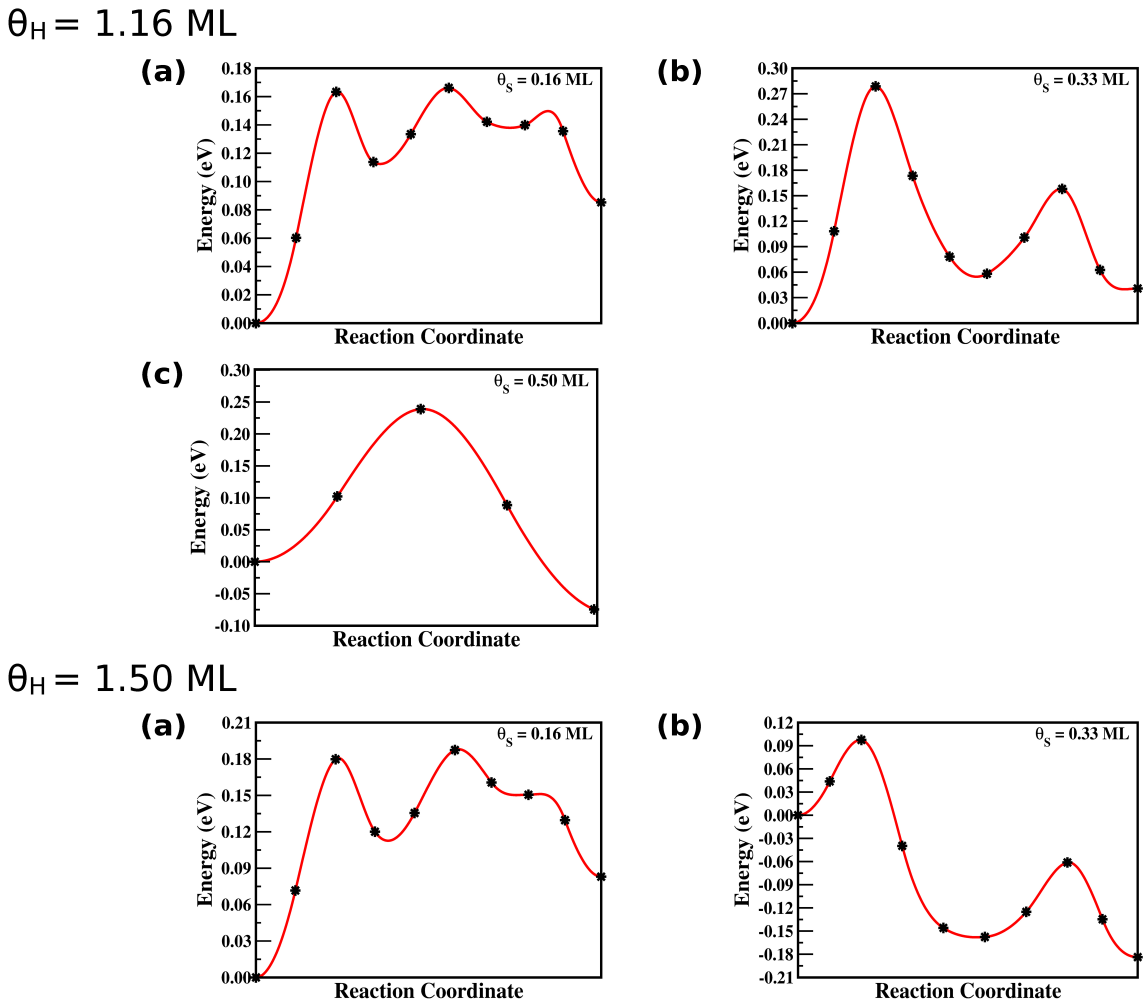


Figure B.13: The energy profile for the H penetration step at different H, S coverage.

Bibliography

[1] G Henkelman, "Atomistic simulations of activated processes in materials", *Annual Review of Materials Research* **47**, pp. 199–216 (2017). xv, 2, 3

[2] Adrian Ioan Ciucivara, *Density functional studies of magnetic semiconductors and multiferroics*, The University of Texas at Austin (2007). xv, 15

[3] Mike C Payne, Michael P Teter, Douglas C Allan, TA Arias, and ad JD Joannopoulos, "Iterative minimization techniques for ab initio total-energy calculations: molecular dynamics and conjugate gradients", *Reviews of modern physics* **64**(4), pp. 1045 (1992). xv, 6, 19, 20

[4] Daniel Sheppard, Rye Terrell, and Graeme Henkelman, "Optimization methods for finding minimum energy paths", *The Journal of chemical physics* **128**(13), pp. 134106 (2008). xv, 26, 27

[5] Graeme Henkelman, Blas P Uberuaga, and Hannes Jónsson, "A climbing image nudged elastic band method for finding saddle points and minimum energy paths", *The Journal of chemical physics* **113**(22), pp. 9901–9904 (2000). xv, 4, 25, 26, 28, 34, 54

[6] Jutta Rogal and Karsten Reuter, "Ab initio atomistic thermodynamics for surfaces: A primer", Technical report Max-planck-gesellschaft zur foerderung der wissenschaften ev berlin (germany ... (2006).

[7] Nandha Kumar, Debabrata Chattaraj, Prasenjit Ghosh, and Chiranjib Majumder, "Microscopic insights into hydrogen permeation through a model pdcu membrane from first-principles investigations", *The Journal of Physical Chemistry C* **122**(24), pp. 12920–12933 (2018). xxiv, 59, 62, 64, 68

[8] Arthur F Voter, Francesco Montalenti, and Timothy C Germann, "Extending the time scale in atomistic simulation of materials", *Annual review of materials research* **32**(1), pp. 321–346 (2002). 2

[9] Arthur F Voter, "Introduction to the kinetic monte carlo method", In *Radiation effects in solids* , pp. 1–23. Springer (2007). 2

[10] Graeme Henkelman and Hannes Jónsson, "A dimer method for finding saddle points on high dimensional potential surfaces using only first derivatives", *The Journal of chemical physics* **111**(15), pp. 7010–7022 (1999). 4, 34, 54

[11] H Jónsson and G Henkelman, "Improved tangent estimate in the nudged elastic band method for finding minimum energy paths and saddle points", *J. Chem. Phys* **113**, pp. 9978 (2000). 4, 34, 54

[12] Paolo Giannozzi, Stefano De Gironcoli, Pasquale Pavone, and Stefano Baroni, "Ab initio calculation of phonon dispersions in semiconductors", *Physical Review B* **43**(9), pp. 7231 (1991). 4, 55

[13] P Pavone, K Karch, O Schütt, D Strauch, W Windl, P Giannozzi, and S Baroni, "Ab initio lattice dynamics of diamond", *Physical Review B* **48**(5), pp. 3156 (1993). 4

[14] Stefano Baroni, Paolo Giannozzi, and Andrea Testa, "Green's-function approach to linear response in solids", *Physical review letters* **58**(18), pp. 1861 (1987). 4

[15] Antonio Gloria, Roberto Montanari, Maria Richetta, and Alessandra Varone, "Alloys for aeronautic applications: state of the art and perspectives", *Metals* **9**(6), pp. 662 (2019). 4

[16] T Nejat Veziroglu, "21st century's energy: Hydrogen energy system", In *Assessment of hydrogen energy for sustainable development* , pp. 9–31. Springer (2007). 5, 53

[17] Mustafa Balat, "Potential importance of hydrogen as a future solution to environmental and transportation problems", *International journal of hydrogen energy* **33**(15), pp. 4013–4029 (2008). 5, 53

[18] C David Sherrill, "An introduction to hartree-fock molecular orbital theory", *School of Chemistry and Biochemistry Georgia Institute of Technology* (2000). 10

[19] Rodney J Bartlett and Monika Musiał, "Coupled-cluster theory in quantum chemistry", *Reviews of Modern Physics* **79**(1), pp. 291 (2007). 10

[20] Pierre Hohenberg and Walter Kohn, "Inhomogeneous electron gas", *Physical review* **136**(3B), pp. B864 (1964). 10

[21] Walter Kohn and Lu Jeu Sham, "Self-consistent equations including exchange and correlation effects", *Physical review* **140**(4A), pp. A1133 (1965). 11

[22] R Martin Electronic Structure, "Basic theory and practical methods, chapter 20.4" (2004). 11

[23] Richard M Martin, *Electronic structure: basic theory and practical methods*, Cambridge university press (2020). 16

[24] David Vanderbilt, "Soft self-consistent pseudopotentials in a generalized eigenvalue formalism", *Physical review B* **41**(11), pp. 7892 (1990). 20

[25] Leny Alvarez-Falcon, Francesc Vines, Almudena Notario-Estevez, and Francesc Illas, "On the hydrogen adsorption and dissociation on cu surfaces and nanorows", *Surface Science* **646**, pp. 221–229 (2016). 21

[26] Stefano Baroni, Stefano De Gironcoli, Andrea Dal Corso, and Paolo Giannozzi, "Phonons and related crystal properties from density-functional perturbation theory", *Reviews of modern Physics* **73**(2), pp. 515 (2001). 22, 24

[27] Hans Hellman, "Einführung in die quantenchemie", *Franz Deuticke, Leipzig* **285** (1937). 23

[28] Eric Ganz, Silva K Theiss, Shouh Hwang, and Jene Golovchenko, "Direct measurement of diffusion by hot tunneling microscopy: activation energy, anisotropy, and long jumps", *Physical review letters* **68**(10), pp. 1567 (1992). 25

[29] Donna Cowell Senft and Gert Ehrlich, "Long jumps in surface diffusion: one-dimensional migration of isolated adatoms", *Physical review letters* **74**(2), pp. 294 (1995). 25

[30] Peter Talkner, "Finite barrier corrections for the kramers rate problem in the spatial diffusion regime", *Chemical physics* **180**(2-3), pp. 199–213 (1994). 25

[31] Peter Talkner and Peter Hänggi, *New trends in Kramers' reaction rate theory* volume 11, Springer Science & Business Media (1995). 25

[32] Robert Wyatt, *Dynamics of molecules and chemical reactions*, CRC Press (1996). 25

[33] Graeme Henkelman, Gísli Jóhannesson, and Hannes Jónsson, "Methods for finding saddle points and minimum energy paths", In *Theoretical methods in condensed phase chemistry* , pp. 269–302. Springer (2002). 25

[34] Matthias Scheffler, "Thermodynamic aspects of bulk and surface defects–first-principle calculations", In *Studies in Surface Science and Catalysis* volume 40 , pp. 115–122. Elsevier (1988).

[35] Guo-Xin Qian, Richard M Martin, and DJ Chadi, "First-principles study of the atomic reconstructions and energies of ga-and as-stabilized gaas (100) surfaces", *Physical Review B* **38**(11), pp. 7649 (1988).

[36] Christoph Leyens and Manfred Peters, editors, *Titanium and Titanium Alloys: Fundamentals and Applications*, Wiley (2003). 31

[37] M.M. Klinger, F. Rahemtulla, C.W. Prince, L.C. Lucas, and J.E. Lemons, "Proteoglycans at the bone-implant interface", *Critical Reviews in Oral Biology & Medicine* **9**(4), pp. 449–463 (1998), PMID: 9825221. 31

[38] PG Allen, "Titanium'95: Science and technology", In *Proc. of 8th World Conf.* volume 1608 (1996). 31

[39] Henry H Wu and Dallas R Trinkle, "Direct diffusion through interpenetrating networks: Oxygen in titanium", *Physical review letters* **107**(4), pp. 045504 (2011). 31

[40] J Stringer, "The oxidation of titanium in oxygen at high temperatures", *Acta Metallurgica* **8**(11), pp. 758–766 (1960). 31

[41] P Kofstad, PB Anderson, and OJ Krudtaa, "Oxidation of titanium in the temperature range 800–1200 c", *Journal of the Less Common Metals* **3**(2), pp. 89–97 (1961). 31

[42] HD Shih, F Jona, DW Jepsen, and PM Marcus, "The structure of the clean ti (0001) surface", *Journal of Physics C: Solid State Physics* **9**(8), pp. 1405 (1976). 31

[43] HD Shih and F Jona, "Low-energy electron diffraction and auger electron spectroscopy study of the oxidation of ti {0001} at room temperature", *Applied physics* **12**(4), pp. 311–315 (1977). 31

[44] H Cichy and E Fromm, "Oxidation kinetics of metal films at 300 k studied by the piezoelectric quartz crystal microbalance technique", *Thin Solid Films* **195**(1-2), pp. 147–158 (1991). 31

[45] D David, G Beranger, and EA Garcia, "A study of the diffusion of oxygen in $alpha$-titanium oxidized in the temperature range 460°–700° c", *Journal of the Electrochemical Society* **130**(6), pp. 1423–1426 (1983). 31

[46] T Kitashima, Y Yamabe-Mtarai, S Iwasaki, and S Kuroda, "Effects of alloying elements on the tensile and oxidation properties of alpha and near-alpha ti alloys", In *Proceedings of the 13th World Conference on Titanium* , pp. 479–483. Wiley Online Library (2016). 31, 32, 33, 49

[47] T Kitashima and T Kawamura, "Prediction of oxidation behavior of near-α titanium alloys", *Scripta Materialia* **124**, pp. 56–58 (2016). 31

[48] Ji Liu, Xiaofeng Fan, Changqing Sun, and Weiguang Zhu, "Oxidation of the titanium (0001) surface: diffusion processes of oxygen from dft", *RSC Advances* **6**(75), pp. 71311–71318 (2016). 31, 32, 36, 43

[49] Henry H Wu and Dallas R Trinkle, "Solute effect on oxygen diffusion in α-titanium", *Journal of Applied Physics* **113**(22), pp. 223504 (2013). 31, 32

[50] Julian Schneider and Lucio Colombi Ciacchi, "First principles and classical modeling of the oxidized titanium (0001) surface", *Surface science* **604**(13-14), pp. 1105–1115 (2010). 31

[51] Bastian Ohler, Stefano Prada, Gianfranco Pacchioni, and Walter Langel, "Dft simulations of titanium oxide films on titanium metal", *The Journal of Physical Chemistry C* **117**(1), pp. 358–367 (2013). 31, 36

[52] Somesh Kr. Bhattacharya, Ryoji Sahara, Tomonori Kitashima, Kyosuke Ueda, and Takayuki Narushima, "First principles study of oxidation of si-segregated α-Ti(0001) surfaces", *Japanese Journal of Applied Physics* **56**(12), pp. 125701 (2017). 31, 32, 37

[53] Somesh Kr. Bhattacharya, Ryoji Sahara, Satoshi Suzuki, Kyosuke Ueda, and Takayuki Narushima, "Mechanisms of oxidation of pure and Si-segregated α-Ti surfaces", *Applied Surface Science* **463**, pp. 686–692 (2019). 31

[54] Adib J. Samin, "Oxidation thermodynamics of Nb-Ti alloys studied via first-principles calculations", *Journal of Alloys and Compounds* **879**, pp. 160455 (2021). 32

[55] Paolo Giannozzi, Stefano Baroni, Nicola Bonini, Matteo Calandra, Roberto Car, Carlo Cavazzoni, Davide Ceresoli, Guido L Chiarotti, Matteo Cococcioni, Ismaila Dabo, Andrea Dal Corso, Stefano de Gironcoli, Stefano Fabris, Guido Fratesi, Ralph Gebauer, Uwe Gerstmann, Christos Gougoussis, Anton Kokalj, Michele Lazzeri, Layla Martin-Samos, Nicola Marzari, Francesco Mauri, Riccardo Mazzarello, Stefano Paolini, Alfredo Pasquarello, Lorenzo Paulatto, Carlo Sbraccia, Sandro Scandolo, Gabriele Sclauzero, Ari P Seitsonen, Alexander Smogunov, Paolo Umari, and Renata M Wentzcovitch, "Quantum espresso: a modular and open-source software project for quantum simulations of materials", *J. Phys.: Condens. Matter* **21**, pp. 395502 (2009). 32, 54

[56] David Vanderbilt, "Soft self-consistent pseudopotentials in a generalized eigenvalue formalism", *Phys. Rev. B* **41**(11), pp. 7892–7895 (1990). 32, 54

[57] John P. Perdew, Kieron Burke, and Matthias Ernzerhof, "Generalized gradient approximation made simple", *Phys. Rev. Lett.* **77**(18), pp. 3865–3868 (1996). 32, 54

[58] Hendrik J Monkhorst and James D Pack, "Special points for brillouin-zone integrations", *Physical review B* **13**(12), pp. 5188 (1976). 32

[59] Nicola Marzari, David Vanderbilt, Alessandro De Vita, and M. C. Payne, "Thermal contraction and disordering of the al(110) surface", *Phys. Rev. Lett.* **82**(16), pp. 3296–3299 (1999). 32, 54

[60] M. N. Huda and Leonard Kleinman, "Density functional calculations of the influence of hydrogen adsorption on the surface relaxation of ti (0001)", *Phys. Rev. B* **71**, pp. 241406 (2005). 32

[61] R M Wood, "The lattice constants of high purity alpha titanium", **80**(3), pp. 783–786 (1962). 32

[62] David R Lide, *CRC handbook of chemistry and physics* volume 85, CRC press (2004). 29, 35

[63] A Kiejna and Bengt I Lundqvist, "First-principles study of surface and subsurface o structures at al (111)", *Physical Review B* **63**(8), pp. 085405 (2001). 36

[64] Mira Todorova, Karsten Reuter, and Matthias Scheffler, "Oxygen overlayers on pd (111) studied by density functional theory", *The Journal of Physical Chemistry B* **108**(38), pp. 14477–14483 (2004). 36

[65] Somesh Kr Bhattacharya, Masanori Kohyama, Shingo Tanaka, and Yoshinori Shiihara, "Si segregation at fe grain boundaries analyzed by ab initio local energy and local stress", *Journal of Physics: Condensed Matter* **26**(35), pp. 355005 (2014). 36

[66] Hans Conrad, "Effect of interstitial solutes on the strength and ductility of titanium", *Progress in Materials Science* **26**(2-4), pp. 123–403 (1981). 36

[67] Jan Koj, Christina Wulf, Andrea Schreiber, and Petra Zapp, "Site-dependent environmental impacts of industrial hydrogen production by alkaline water electrolysis", *Energies* **10**(7), pp. 860 (2017). 53

[68] Christos Didaskalou, Sibel Buyuktiryaki, Rustem Kecili, Claudio P Fonte, and Gyorgy Szekely, "Valorisation of agricultural waste with an adsorption/nanofiltration hybrid process: from materials to sustainable process design", *Green Chemistry* **19**(13), pp. 3116–3125 (2017). 53

[69] Tina M Nenoff, Richard J Spontak, and Christopher M Aberg, "Membranes for hydrogen purification: an important step toward a hydrogen-based economy", *Mrs Bulletin* **31**(10), pp. 735–744 (2006). 53

[70] Brian D Adams and Aicheng Chen, "The role of palladium in a hydrogen economy", *Materials today* **14**(6), pp. 282–289 (2011). 53

[71] Nathan W Ockwig and Tina M Nenoff, "Membranes for hydrogen separation", *Chemical reviews* **107**(10), pp. 4078–4110 (2007). 53

[72] SA Steward, "Review of hydrogen isotope permeability through materials", Technical report Lawrence Livermore National Lab.(LLNL), Livermore, CA (United States) (1983). 53

[73] W Eichenauer, "Fa lewis: The palladium hydrogen system. academic press, london and new york 1967. 178 seiten, 87 abbildungen. preis: 45 s.", *Berichte der Bunsengesellschaft für physikalische Chemie* **71**(9-10), pp. 1160–1161 (1967). 53

[74] Shin-Kun Ryi, Nong Xu, Anwu Li, C Jim Lim, and John R Grace, "Electroless pd membrane deposition on alumina modified porous hastelloy substrate with edta-free bath", *international journal of hydrogen energy* **35**(6), pp. 2328–2335 (2010). 53

[75] Shigeyuki Uemiya, "State-of-the-art of supported metal membranes for gas separation", *Separation and purification Methods* **28**(1), pp. 51–85 (1999). 53

[76] Graeme W Watson, Richard PK Wells, David J Willock, and Graham J Hutchings, "A comparison of the adsorption and diffusion of hydrogen on the {111} surfaces of ni, pd, and pt from density functional theory calculations", *The Journal of Physical Chemistry B* **105**(21), pp. 4889–4894 (2001). 53

[77] Roland Dittmeyer, Volker Höllein, and Kristian Daub, "Membrane reactors for hydrogenation and dehydrogenation processes based on supported palladium", *Journal of Molecular Catalysis A: Chemical* **173**(1-2), pp. 135–184 (2001). 53

[78] AG Knapton, "Palladium alloys for hydrogen diffusion membranes", *Platinum Metals Review* **21**(2), pp. 44–50 (1977). 53

[79] Samhun Yun and S Ted Oyama, "Correlations in palladium membranes for hydrogen separation: a review", *Journal of membrane science* **375**(1-2), pp. 28–45 (2011). 53

[80] David L Mckinley, "Method for hydrogen separation and purification" (1969), US Patent 3,439,474. 53

[81] Fernando Roa, Michael J Block, and J Douglas Way, "The influence of alloy composition on the h2 flux of composite pd cu membranes", *Desalination* **147**(1-3), pp. 411–416 (2002). 54

[82] John Piper, "Diffusion of hydrogen in copper-palladium alloys", *Journal of Applied Physics* **37**(2), pp. 715–721 (1966). 54

[83] A Yu Volkov, OS Novikova, and BD Antonov, "Formation of an ordered structure in the cu-49 at% pd alloy", *Inorganic Materials* **49**(1), pp. 43–48 (2013). 54

[84] Miho Yamauchi and Tatsuya Tsukuda, "Production of an ordered (b2) cupd nanoalloy by low-temperature annealing under hydrogen atmosphere", *Dalton Transactions* **40**(18), pp. 4842–4845 (2011). 54

[85] Cai Wei, FT Kong, and HR Gong, "Phase stability and elastic property of pdh and pdcuh phases", *international journal of hydrogen energy* **38**(36), pp. 16485–16494 (2013). 54

[86] Dominic R Alfonso, Anthony V Cugini, and Dan C Sorescu, "Adsorption and decomposition of h2s on pd (1 1 1) surface: a first-principles study", *Catalysis Today* **99**(3-4), pp. 315–322 (2005). 56, 57

[87] Yi Li, Pan Huang, Dandan Tao, Juan Wu, Mei Qiu, Xin Huang, Kaining Ding, Wenkai Chen, Wenyue Su, and Yongfan Zhang, "Adsorption and dissociation of h2s on monometallic and monolayer bimetallic ni/pd (111) surfaces: A first-principles study", *Applied Surface Science* **387**, pp. 301–307 (2016). 56, 58, 59

[88] Zhao Jiang, Pei Qin, and Tao Fang, "Investigation on adsorption and decomposition of h2s on pd (1 0 0) surface: A dft study", *Surface Science* **632**, pp. 195–200 (2015). 56, 59

[89] José A Rodriguez and Jan Hrbek, "Interaction of sulfur with well-defined metal and oxide surfaces: unraveling the mysteries behind catalyst poisoning and desulfurization", *Accounts of Chemical Research* **32**(9), pp. 719–728 (1999). 57

[90] PA Gravil and H Toulhoat, "Hydrogen, sulphur and chlorine coadsorption on pd (111): a theoretical study of poisoning and promotion", *Surface Science* **430**(1-3), pp. 176–191 (1999). 57

AIP PUBLISHING LICENSE
TERMS AND CONDITIONS

Oct 24, 2022

This Agreement between Kanika Kohli ("You") and AIP Publishing ("AIP Publishing") consists of your license details and the terms and conditions provided by AIP Publishing and Copyright Clearance Center.

License Number	5402230215220
License date	Oct 04, 2022
Licensed Content Publisher	AIP Publishing
Licensed Content Publication	Journal of Chemical Physics
Licensed Content Title	Optimization methods for finding minimum energy paths
Licensed Content Author	Daniel Sheppard, Rye Terrell, Graeme Henkelman
Licensed Content Date	Apr 7, 2008
Licensed Content Volume	128
Licensed Content Issue	13
Type of Use	Thesis/Dissertation
Requestor type	Student
Format	Print and electronic

Portion	Figure/Table
Number of figures/tables	1
Will you be translating?	No
Title	First Principles study of thermally activated processes on transition metal surfaces
Institution name	Indian Institute of Science Education and Research(IISER), Pune, India
Expected presentation date	Oct 2022
Portions	Figure 1 on page 134106-2
Requestor Location	Kanika Kohli Green Field House Number 83 Ludhiana, PB 141001 India Attn: Miss Kanika Kohli
Total	0.00 USD

Terms and Conditions

AIP Publishing -- Terms and Conditions: Permissions Uses

AIP Publishing hereby grants to you the non-exclusive right and license to use and/or distribute the Material according to the use specified in your order, on a one-time basis, for the specified term, with a maximum distribution equal to the number that you have ordered. Any links or other content accompanying the Material are not the subject of this license.

1. You agree to include the following copyright and permission notice with the reproduction of the Material:"Reprinted from [FULL CITATION], with the permission of AIP Publishing." For an article, the credit line and permission notice must be printed on the first page of the article or book chapter. For photographs, covers, or tables, the notice may appear with the Material, in a footnote, or in the reference list.

2. If you have licensed reuse of a figure, photograph, cover, or table, it is your responsibility to ensure that the material is original to AIP Publishing and does not contain the copyright of another entity, and that the copyright notice of the figure, photograph, cover, or table does not indicate that it was reprinted by AIP Publishing, with permission, from another source. Under no circumstances does AIP Publishing purport or intend to grant permission to reuse material to which it does not hold appropriate rights.
   You may not alter or modify the Material in any manner. You may translate the Material into another language only if you have licensed translation rights. You may not use the Material for promotional purposes.
3. The foregoing license shall not take effect unless and until AIP Publishing or its agent, Copyright Clearance Center, receives the Payment in accordance with Copyright Clearance Center Billing and Payment Terms and Conditions, which are incorporated herein by reference.
4. AIP Publishing or Copyright Clearance Center may, within two business days of granting this license, revoke the license for any reason whatsoever, with a full refund payable to you. Should you violate the terms of this license at any time, AIP Publishing, or Copyright Clearance Center may revoke the license with no refund to you. Notice of such revocation will be made using the contact information provided by you. Failure to receive such notice will not nullify the revocation.
5. AIP Publishing makes no representations or warranties with respect to the Material. You agree to indemnify and hold harmless AIP Publishing, and their officers, directors, employees or agents from and against any and all claims arising out of your use of the Material other than as specifically authorized herein.
6. The permission granted herein is personal to you and is not transferable or assignable without the prior written permission of AIP Publishing. This license may not be amended except in a writing signed by the party to be charged.
7. If purchase orders, acknowledgments or check endorsements are issued on any forms containing terms and conditions which are inconsistent with these provisions, such inconsistent terms and conditions shall be of no force and effect. This document, including the CCC Billing and Payment Terms and Conditions, shall be the entire agreement between the parties relating to the subject matter hereof.

This Agreement shall be governed by and construed in accordance with the laws of the State of New York. Both parties hereby submit to the jurisdiction of the courts of New York County for purposes of resolving any disputes that may arise hereunder.

V1.2

Questions? customercare@copyright.com or +1-855-239-3415 (toll free in the US) or +1-978-646-2777.

Marketplace™

This is a License Agreement between Kanika Kohli ("User") and Copyright Clearance Center, Inc. ("CCC") on behalf of the Rightsholder identified in the order details below. The license consists of the order details, the CCC Terms and Conditions below, and any Rightsholder Terms and Conditions which are included below.

All payments must be made in full to CCC in accordance with the CCC Terms and Conditions below.

Order Date	17-May-2022	**Type of Use**	Republish in a thesis/dissertation
Order License ID	1222475-1		
ISSN	1545-4118	**Publisher**	ANNUAL REVIEWS
		Portion	Chart/graph/table/figure

LICENSED CONTENT

Publication Title	Annual review of materials research	**Rightsholder**	Annual Reviews, Inc.
		Publication Type	e-Journal
Date	12/31/2000	**URL**	http://arjournals.annualreviews.org/loi/matsci
Language	English		
Country	United States of America		

REQUEST DETAILS

Portion Type	Chart/graph/table/figure	**Distribution**	Worldwide
Number of charts / graphs / tables / figures requested	1	**Translation**	Original language of publication
		Copies for the disabled?	No
Format (select all that apply)	Print, Electronic	**Minor editing privileges?**	No
Who will republish the content?	Academic institution	**Incidental promotional use?**	No
Duration of Use	Life of current edition	**Currency**	USD
Lifetime Unit Quantity	Up to 499		
Rights Requested	Main product		

NEW WORK DETAILS

Title	First Principles Study of thermally activated processes on transition metal surfaces	**Institution name**	Indian Institute of Science Education and Research, Pune
		Expected presentation date	2022-05-18
Instructor name	Dr. Prasenjit Ghosh		

ADDITIONAL DETAILS

Order reference number	N/A	**The requesting person / organization to appear on the license**	Kanika Kohli

REUSE CONTENT DETAILS

Title, description or numeric reference of the portion(s)	Figure 2	**Title of the article/chapter the portion is from**	Atomistic Simulations of Activated Processes in Materials
Editor of portion(s)	N/A	**Author of portion(s)**	G. Henkelman
Volume of serial or monograph	47	**Issue, if republishing an article from a serial**	N/A
Page or page range of portion	3.3	**Publication date of portion**	2017-02-16

CCC Terms and Conditions

1. Description of Service; Defined Terms. This Republication License enables the User to obtain licenses for republication of one or more copyrighted works as described in detail on the relevant Order Confirmation (the "Work(s)"). Copyright Clearance Center, Inc. ("CCC") grants licenses through the Service on behalf of the rightsholder identified on the Order Confirmation (the "Rightsholder"). "Republication", as used herein, generally means the inclusion of a Work, in whole or in part, in a new work or works, also as described on the Order Confirmation. "User", as used herein, means the person or entity making such republication.

2. The terms set forth in the relevant Order Confirmation, and any terms set by the Rightsholder with respect to a particular Work, govern the terms of use of Works in connection with the Service. By using the Service, the person transacting for a republication license on behalf of the User represents and warrants that he/she/it (a) has been duly authorized by the User to accept, and hereby does accept, all such terms and conditions on behalf of User, and (b) shall inform User of all such terms and conditions. In the event such person is a "freelancer" or other third party independent of User and CCC, such party shall be deemed jointly a "User" for purposes of these terms and conditions. In any event, User shall be deemed to have accepted and agreed to all such terms and conditions if User republishes the Work in any fashion.

3. Scope of License; Limitations and Obligations.

    3.1. All Works and all rights therein, including copyright rights, remain the sole and exclusive property of the Rightsholder. The license created by the exchange of an Order Confirmation (and/or any invoice) and payment by User of the full amount set forth on that document includes only those rights expressly set forth in the Order Confirmation and in these terms and conditions, and conveys no other rights in the Work(s) to User. All rights not expressly granted are hereby reserved.

    3.2. General Payment Terms: You may pay by credit card or through an account with us payable at the end of the month. If you and we agree that you may establish a standing account with CCC, then the following terms apply: Remit Payment to: Copyright Clearance Center, 29118 Network Place, Chicago, IL 60673-1291. Payments Due: Invoices are payable upon their delivery to you (or upon our notice to you that they are available to you for downloading). After 30 days, outstanding amounts will be subject to a service charge of 1-1/2% per month or, if less, the maximum rate allowed by applicable law. Unless otherwise specifically set forth in the Order Confirmation or in a separate written agreement signed by CCC, invoices are due and payable on "net 30" terms. While User may exercise the rights licensed immediately upon issuance of the Order Confirmation, the license is automatically revoked and is null and void, as if it had never been issued, if complete payment for the license is not received on a timely basis either from User directly or through a payment agent, such as a credit card company.

    3.3. Unless otherwise provided in the Order Confirmation, any grant of rights to User (i) is "one-time" (including the editions and product family specified in the license), (ii) is non-exclusive and non-transferable and (iii) is subject to any and all limitations and restrictions (such as, but not limited to, limitations on duration of use or circulation) included in the Order Confirmation or invoice and/or in these terms and conditions. Upon completion of the licensed use, User shall either secure a new permission for further use of the Work(s) or immediately cease any new use of the Work(s) and shall render inaccessible (such as by deleting or by removing or severing links or other locators) any further copies of the Work (except for copies printed on paper in accordance with this license and still in User's stock at the end of such period).

3.4. In the event that the material for which a republication license is sought includes third party materials (such as photographs, illustrations, graphs, inserts and similar materials) which are identified in such material as having been used by permission, User is responsible for identifying, and seeking separate licenses (under this Service or otherwise) for, any of such third party materials; without a separate license, such third party materials may not be used.

3.5. Use of proper copyright notice for a Work is required as a condition of any license granted under the Service. Unless otherwise provided in the Order Confirmation, a proper copyright notice will read substantially as follows: "Republished with permission of [Rightsholder's name], from [Work's title, author, volume, edition number and year of copyright]; permission conveyed through Copyright Clearance Center, Inc. " Such notice must be provided in a reasonably legible font size and must be placed either immediately adjacent to the Work as used (for example, as part of a by-line or footnote but not as a separate electronic link) or in the place where substantially all other credits or notices for the new work containing the republished Work are located. Failure to include the required notice results in loss to the Rightsholder and CCC, and the User shall be liable to pay liquidated damages for each such failure equal to twice the use fee specified in the Order Confirmation, in addition to the use fee itself and any other fees and charges specified.

3.6. User may only make alterations to the Work if and as expressly set forth in the Order Confirmation. No Work may be used in any way that is defamatory, violates the rights of third parties (including such third parties' rights of copyright, privacy, publicity, or other tangible or intangible property), or is otherwise illegal, sexually explicit or obscene. In addition, User may not conjoin a Work with any other material that may result in damage to the reputation of the Rightsholder. User agrees to inform CCC if it becomes aware of any infringement of any rights in a Work and to cooperate with any reasonable request of CCC or the Rightsholder in connection therewith.

4. Indemnity. User hereby indemnifies and agrees to defend the Rightsholder and CCC, and their respective employees and directors, against all claims, liability, damages, costs and expenses, including legal fees and expenses, arising out of any use of a Work beyond the scope of the rights granted herein, or any use of a Work which has been altered in any unauthorized way by User, including claims of defamation or infringement of rights of copyright, publicity, privacy or other tangible or intangible property.

5. Limitation of Liability. UNDER NO CIRCUMSTANCES WILL CCC OR THE RIGHTSHOLDER BE LIABLE FOR ANY DIRECT, INDIRECT, CONSEQUENTIAL OR INCIDENTAL DAMAGES (INCLUDING WITHOUT LIMITATION DAMAGES FOR LOSS OF BUSINESS PROFITS OR INFORMATION, OR FOR BUSINESS INTERRUPTION) ARISING OUT OF THE USE OR INABILITY TO USE A WORK, EVEN IF ONE OF THEM HAS BEEN ADVISED OF THE POSSIBILITY OF SUCH DAMAGES. In any event, the total liability of the Rightsholder and CCC (including their respective employees and directors) shall not exceed the total amount actually paid by User for this license. User assumes full liability for the actions and omissions of its principals, employees, agents, affiliates, successors and assigns.

6. Limited Warranties. THE WORK(S) AND RIGHT(S) ARE PROVIDED "AS IS". CCC HAS THE RIGHT TO GRANT TO USER THE RIGHTS GRANTED IN THE ORDER CONFIRMATION DOCUMENT. CCC AND THE RIGHTSHOLDER DISCLAIM ALL OTHER WARRANTIES RELATING TO THE WORK(S) AND RIGHT(S), EITHER EXPRESS OR IMPLIED, INCLUDING WITHOUT LIMITATION IMPLIED WARRANTIES OF MERCHANTABILITY OR FITNESS FOR A PARTICULAR PURPOSE. ADDITIONAL RIGHTS MAY BE REQUIRED TO USE ILLUSTRATIONS, GRAPHS, PHOTOGRAPHS, ABSTRACTS, INSERTS OR OTHER PORTIONS OF THE WORK (AS OPPOSED TO THE ENTIRE WORK) IN A MANNER CONTEMPLATED BY USER; USER UNDERSTANDS AND AGREES THAT NEITHER CCC NOR THE RIGHTSHOLDER MAY HAVE SUCH ADDITIONAL RIGHTS TO GRANT.

7. Effect of Breach. Any failure by User to pay any amount when due, or any use by User of a Work beyond the scope of the license set forth in the Order Confirmation and/or these terms and conditions, shall be a material breach of the license created by the Order Confirmation and these terms and conditions. Any breach not cured within 30 days of written notice thereof shall result in immediate termination of such license without further notice. Any unauthorized (but licensable) use of a Work that is terminated immediately upon notice thereof may be liquidated by payment of the Rightsholder's ordinary license price therefor; any unauthorized (and unlicensable) use that is not terminated immediately for any reason (including, for example, because materials containing the Work cannot

reasonably be recalled) will be subject to all remedies available at law or in equity, but in no event to a payment of less than three times the Rightsholder's ordinary license price for the most closely analogous licensable use plus Rightsholder's and/or CCC's costs and expenses incurred in collecting such payment.

8. Miscellaneous.

8.1. User acknowledges that CCC may, from time to time, make changes or additions to the Service or to these terms and conditions, and CCC reserves the right to send notice to the User by electronic mail or otherwise for the purposes of notifying User of such changes or additions; provided that any such changes or additions shall not apply to permissions already secured and paid for.

8.2. Use of User-related information collected through the Service is governed by CCC's privacy policy, available online here:https://marketplace.copyright.com/rs-ui-web/mp/privacy-policy

8.3. The licensing transaction described in the Order Confirmation is personal to User. Therefore, User may not assign or transfer to any other person (whether a natural person or an organization of any kind) the license created by the Order Confirmation and these terms and conditions or any rights granted hereunder; provided, however, that User may assign such license in its entirety on written notice to CCC in the event of a transfer of all or substantially all of User's rights in the new material which includes the Work(s) licensed under this Service.

8.4. No amendment or waiver of any terms is binding unless set forth in writing and signed by the parties. The Rightsholder and CCC hereby object to any terms contained in any writing prepared by the User or its principals, employees, agents or affiliates and purporting to govern or otherwise relate to the licensing transaction described in the Order Confirmation, which terms are in any way inconsistent with any terms set forth in the Order Confirmation and/or in these terms and conditions or CCC's standard operating procedures, whether such writing is prepared prior to, simultaneously with or subsequent to the Order Confirmation, and whether such writing appears on a copy of the Order Confirmation or in a separate instrument.

8.5. The licensing transaction described in the Order Confirmation document shall be governed by and construed under the law of the State of New York, USA, without regard to the principles thereof of conflicts of law. Any case, controversy, suit, action, or proceeding arising out of, in connection with, or related to such licensing transaction shall be brought, at CCC's sole discretion, in any federal or state court located in the County of New York, State of New York, USA, or in any federal or state court whose geographical jurisdiction covers the location of the Rightsholder set forth in the Order Confirmation. The parties expressly submit to the personal jurisdiction and venue of each such federal or state court.If you have any comments or questions about the Service or Copyright Clearance Center, please contact us at 978-750-8400 or send an e-mail to support@copyright.com.

v 1.1

AIP PUBLISHING LICENSE
TERMS AND CONDITIONS

May 18, 2022

This Agreement between Kanika Kohli ("You") and AIP Publishing ("AIP Publishing") consists of your license details and the terms and conditions provided by AIP Publishing and Copyright Clearance Center.

License Number	5311780790915
License date	May 18, 2022
Licensed Content Publisher	AIP Publishing
Licensed Content Publication	Journal of Chemical Physics
Licensed Content Title	A climbing image nudged elastic band method for finding saddle points and minimum energy paths
Licensed Content Author	Graeme Henkelman, Blas P. Uberuaga, Hannes Jónsson
Licensed Content Date	Dec 8, 2000
Licensed Content Volume	113
Licensed Content Issue	22
Type of Use	Thesis/Dissertation
Requestor type	Student

Format	Print and electronic
Portion	Figure/Table
Number of figures/tables	1
Will you be translating?	No
Title	First Principles study of thermally activated processes on transition metal surfaces
Institution name	Indian Institute of Science Education and Research(IISER), Pune, India
Expected presentation date	May 2022
Portions	FIG.1
Requestor Location	Kanika Kohli Green Field House Number 83 Ludhiana, PB 141001 India Attn: Miss Kanika Kohli
Total	0.00 USD

Terms and Conditions

AIP Publishing -- Terms and Conditions: Permissions Uses

AIP Publishing hereby grants to you the non-exclusive right and license to use and/or distribute the Material according to the use specified in your order, on a one-time basis, for the specified term, with a maximum distribution equal to the number that you have ordered. Any links or other content accompanying the Material are not the subject of this license.

1. You agree to include the following copyright and permission notice with the reproduction of the Material:"Reprinted from [FULL CITATION], with the permission

of AIP Publishing." For an article, the credit line and permission notice must be printed on the first page of the article or book chapter. For photographs, covers, or tables, the notice may appear with the Material, in a footnote, or in the reference list.

2. If you have licensed reuse of a figure, photograph, cover, or table, it is your responsibility to ensure that the material is original to AIP Publishing and does not contain the copyright of another entity, and that the copyright notice of the figure, photograph, cover, or table does not indicate that it was reprinted by AIP Publishing, with permission, from another source. Under no circumstances does AIP Publishing purport or intend to grant permission to reuse material to which it does not hold appropriate rights.
   You may not alter or modify the Material in any manner. You may translate the Material into another language only if you have licensed translation rights. You may not use the Material for promotional purposes.
3. The foregoing license shall not take effect unless and until AIP Publishing or its agent, Copyright Clearance Center, receives the Payment in accordance with Copyright Clearance Center Billing and Payment Terms and Conditions, which are incorporated herein by reference.
4. AIP Publishing or Copyright Clearance Center may, within two business days of granting this license, revoke the license for any reason whatsoever, with a full refund payable to you. Should you violate the terms of this license at any time, AIP Publishing, or Copyright Clearance Center may revoke the license with no refund to you. Notice of such revocation will be made using the contact information provided by you. Failure to receive such notice will not nullify the revocation.
5. AIP Publishing makes no representations or warranties with respect to the Material. You agree to indemnify and hold harmless AIP Publishing, and their officers, directors, employees or agents from and against any and all claims arising out of your use of the Material other than as specifically authorized herein.
6. The permission granted herein is personal to you and is not transferable or assignable without the prior written permission of AIP Publishing. This license may not be amended except in a writing signed by the party to be charged.
7. If purchase orders, acknowledgments or check endorsements are issued on any forms containing terms and conditions which are inconsistent with these provisions, such inconsistent terms and conditions shall be of no force and effect. This document, including the CCC Billing and Payment Terms and Conditions, shall be the entire agreement between the parties relating to the subject matter hereof.

This Agreement shall be governed by and construed in accordance with the laws of the State of New York. Both parties hereby submit to the jurisdiction of the courts of New York County for purposes of resolving any disputes that may arise hereunder.

V1.2

Questions? customercare@copyright.com or +1-855-239-3415 (toll free in the US) or +1-978-646-2777.

American Physical Society
Reuse and Permissions License

04-Oct-2022

This license agreement between the American Physical Society ("APS") and Kanika Kohli ("You") consists of your license details and the terms and conditions provided by the American Physical Society and SciPris.

Licensed Content Information

License Number:	**RNP/22/OCT/058583**
License date:	04-Oct-2022
DOI:	10.1103/RevModPhys.64.1045
Title:	Iterative minimization techniques for ab initio total-energy calculations: molecular dynamics and conjugate gradients
Author:	M. C. Payne et al.
Publication:	Reviews of Modern Physics
Publisher:	American Physical Society
Cost:	USD $ 0.00

Request Details

Does your reuse require significant modifications: No

Specify intended distribution locations:	Worldwide
Reuse Category:	Reuse in a thesis/dissertation
Requestor Type:	Student
Items for Reuse:	Figures/Tables
Number of Figure/Tables:	1
Figure/Tables Details:	Fig 5
Format for Reuse:	Print and Electronic
Total number of print copies:	Up to 1000

Information about New Publication:

University/Publisher:	Indian Institute of Science Education and Research(IISER), Pune, India
Title of dissertation/thesis:	First principles study of thermally activated processes on transition metal surfaces
Author(s):	Kanika Kohli
Expected completion date:	Oct. 2022

License Requestor Information

Name:	Kanika Kohli
Affiliation:	Individual
Email Id:	kanika.kohli@students.iiserpune.ac.in
Country:	India

American Physical Society
Reuse and Permissions License

TERMS AND CONDITIONS

The American Physical Society (APS) is pleased to grant the Requestor of this license a non-exclusive, non-transferable permission, limited to Print and Electronic format, provided all criteria outlined below are followed.

1. You must also obtain permission from at least one of the lead authors for each separate work, if you haven't done so already. The author's name and affiliation can be found on the first page of the published Article.

2. For electronic format permissions, Requestor agrees to provide a hyperlink from the reprinted APS material using the source material's DOI on the web page where the work appears. The hyperlink should use the standard DOI resolution URL, http://dx.doi.org/{DOI}. The hyperlink may be embedded in the copyright credit line.

3. For print format permissions, Requestor agrees to print the required copyright credit line on the first page where the material appears: "Reprinted (abstract/excerpt/figure) with permission from [(FULL REFERENCE CITATION) as follows: Author's Names, APS Journal Title, Volume Number, Page Number and Year of Publication.] Copyright (YEAR) by the American Physical Society."

4. Permission granted in this license is for a one-time use and does not include permission for any future editions, updates, databases, formats or other matters. Permission must be sought for any additional use.

5. Use of the material does not and must not imply any endorsement by APS.

6. APS does not imply, purport or intend to grant permission to reuse materials to which it does not hold copyright. It is the requestor's sole responsibility to ensure the licensed material is original to APS and does not contain the copyright of another entity, and that the copyright notice of the figure, photograph, cover or table does not indicate it was reprinted by APS with permission from another source.

7. The permission granted herein is personal to the Requestor for the use specified and is not transferable or assignable without express written permission of APS. This license may not be amended except in writing by APS.

8. You may not alter, edit or modify the material in any manner.

9. You may translate the materials only when translation rights have been granted.

10. APS is not responsible for any errors or omissions due to translation.

11. You may not use the material for promotional, sales, advertising or marketing purposes.

12. The foregoing license shall not take effect unless and until APS or its agent, Aptara, receives payment in full in accordance with Aptara Billing and Payment Terms and Conditions, which are incorporated herein by reference.

13. Should the terms of this license be violated at any time, APS or Aptara may revoke the license with no refund to you and seek relief to the fullest extent of the laws of the USA. Official written notice will be made using the contact information provided with the permission request. Failure to receive such notice will not nullify revocation of the permission.

14. APS reserves all rights not specifically granted herein.

15. This document, including the Aptara Billing and Payment Terms and Conditions, shall be the entire agreement between the parties relating to the subject matter hereof.

American Physical Society
Reuse and Permissions License

18-May-2022

This license agreement between the American Physical Society ("APS") and Kanika Kohli ("You") consists of your license details and the terms and conditions provided by the American Physical Society and SciPris.

Licensed Content Information

License Number:	**RNP/22/MAY/053780**
License date:	18-May-2022
DOI:	10.1103/RevModPhys.64.1045
Title:	Iterative minimization techniques for ab initio total-energy calculations: molecular dynamics and conjugate gradients
Author:	M. C. Payne et al.
Publication:	Reviews of Modern Physics
Publisher:	American Physical Society
Cost:	USD $ 0.00

Request Details

Does your reuse require significant modifications: No

Specify intended distribution locations:	Worldwide
Reuse Category:	Reuse in a thesis/dissertation
Requestor Type:	Student
Items for Reuse:	Figures/Tables
Number of Figure/Tables:	1
Figure/Tables Details:	FiG.3
Format for Reuse:	Print and Electronic
Total number of print copies:	Up to 1000

Information about New Publication:

University/Publisher:	Indian Institute of Science Education and Research(IISER), Pune, India
Title of dissertation/thesis:	First Principles study of thermally activated processes on transition metal surfaces
Author(s):	Kanika Kohli
Expected completion date:	May. 2022

License Requestor Information

Name:	Kanika Kohli
Affiliation:	Individual
Email Id:	kanika.kohli@students.iiserpune.ac.in
Country:	India

American Physical Society
Reuse and Permissions License

TERMS AND CONDITIONS

The American Physical Society (APS) is pleased to grant the Requestor of this license a non-exclusive, non-transferable permission, limited to Print and Electronic format, provided all criteria outlined below are followed.

1. You must also obtain permission from at least one of the lead authors for each separate work, if you haven't done so already. The author's name and affiliation can be found on the first page of the published Article.

2. For electronic format permissions, Requestor agrees to provide a hyperlink from the reprinted APS material using the source material's DOI on the web page where the work appears. The hyperlink should use the standard DOI resolution URL, http://dx.doi.org/{DOI}. The hyperlink may be embedded in the copyright credit line.

3. For print format permissions, Requestor agrees to print the required copyright credit line on the first page where the material appears: "Reprinted (abstract/excerpt/figure) with permission from [(FULL REFERENCE CITATION) as follows: Author's Names, APS Journal Title, Volume Number, Page Number and Year of Publication.] Copyright (YEAR) by the American Physical Society."

4. Permission granted in this license is for a one-time use and does not include permission for any future editions, updates, databases, formats or other matters. Permission must be sought for any additional use.

5. Use of the material does not and must not imply any endorsement by APS.

6. APS does not imply, purport or intend to grant permission to reuse materials to which it does not hold copyright. It is the requestor's sole responsibility to ensure the licensed material is original to APS and does not contain the copyright of another entity, and that the copyright notice of the figure, photograph, cover or table does not indicate it was reprinted by APS with permission from another source.

7. The permission granted herein is personal to the Requestor for the use specified and is not transferable or assignable without express written permission of APS. This license may not be amended except in writing by APS.

8. You may not alter, edit or modify the material in any manner.

9. You may translate the materials only when translation rights have been granted.

10. APS is not responsible for any errors or omissions due to translation.

11. You may not use the material for promotional, sales, advertising or marketing purposes.

12. The foregoing license shall not take effect unless and until APS or its agent, Aptara, receives payment in full in accordance with Aptara Billing and Payment Terms and Conditions, which are incorporated herein by reference.

13. Should the terms of this license be violated at any time, APS or Aptara may revoke the license with no refund to you and seek relief to the fullest extent of the laws of the USA. Official written notice will be made using the contact information provided with the permission request. Failure to receive such notice will not nullify revocation of the permission.

14. APS reserves all rights not specifically granted herein.

15. This document, including the Aptara Billing and Payment Terms and Conditions, shall be the entire agreement between the parties relating to the subject matter hereof.